SCIENCE OF MULTIPHYSICS BEHAVIOR OF SI/C COMPOSITE ACTIVE PARTICLES IN ANODES

by

Xiang Gao

A dissertation submitted to the faculty of
The University of North Carolina at Charlotte
in partial fulfillment of the requirements
for the degree of Doctor of Philosophy in
Mechanical Engineering

Charlotte

2021

Approved by:

Dr. Jun Xu

Dr. Harish Cherukuri

Dr. Mesbah Uddin

Dr. Howie Fang

Dr. Wei Fan

ABSTRACT

XIANG GAO. Science of Multiphysics Behavior of Si/C Composite Active Particles in Anodes
(Under the direction of DR. JUN XU)

The rapidly growing demands on energy storage technologies over the last decade have imposed further requirements for the high energy/power density, safety, and durability of lithium-ion batteries (LIBs). Si/C composite materials have attracted enormous research interest as the most promising candidates for the anodes of next-generation lithium-ion batteries, owing to their high energy density and mechanical buffering property. However, the major disadvantage of materials with ultra-high capacities, such as Si-based materials, is the significant volume change during cycling, which further leads to mechanical and electrochemical degradation. A comprehensive computational model is indispensable in the developing process of the excellent performance of anode material due to the low-realizability, inconvenience, and high-cost of experiments, which also provides powerful tools for fabrication guidance of novel Si/C composites designs. Further, the fundamental mechanism of Li diffusion and complex failure behaviors in various Si/C composite materials remains unclear, with our understanding limited by experimental techniques and continuum modeling methodologies. Thus, DFT simulation is firstly used to investigate the Li diffusion behavior in Si/C composite materials, which indicates the underlying mechanism and provides a quantitative description of the diffusivity. A multiphysics modeling framework is then established. The relationship between mechanical failure and electrochemical performance in Si/C core-shell particles is revealed using this model.

Further, based on this multiphysics model, the contact behavior of two Si/C core-shell particles is studied, and five representative nanostructures are compared, providing design guidance on Si/C core-shell and related structures. Finally, the model is extended into a multi-scale one, which can describe the multiphysics behavior both at the particle level and cell level.

This study explores the multiphysics behavior of Si/C anodes material from the atomic level to cell level using DFT modeling and FEA methodology, systematically revealing the coupling mechanism among various physical fields, as well as providing efficient and powerful tools in the design, development, and evaluation of high energy density lithium-ion batteries.

ACKNOWLEDGMENTS

I would like to express my sincere gratitude to my advisor, Dr. Jun Xu, for his guidance not only in my research works but also in the courses of my Ph.D. degree. He devotes all his attention to teaching me how to do research step by step at the beginning. With his great patience, I grow up from a young and careless student to a skillful, mature, and qualified researcher. Also, he always let me think about the research topics by myself to keep me innovative and creative. Moreover, he is always there whenever I have difficulties either in research work or in daily life.

I am so grateful to Dr. Wenquan Lu, who is like my second advisor. He had no hesitation to help me understand the fundamental knowledge in a new area that I was trying to enter when I first turned to him. Then, we keep a very good connection during my whole Ph.D. program, and I learned a lot from him.

I am so honored to have Dr. Harish Cherukuri, Dr. Mesbah Uddin, Dr. Howie Fang, and Dr. Wei Fan serve as my committee members. I appreciate their insightful and valuable comments and suggestions, which help me enhance my knowledge and improve my topic. I am grateful to every member of our research group. I'd like to thank Yikai Jia and Chunhao Yuan for their great help with simulation issues and experiments during my research work, as well as working together on many projects. Thanks to Wen Zhang, she helps me a lot in building the lab facilities and teaches me how to use the equipment.

I want to show my thanks to all my co-authors, especially Prof. Binghe Liu and Prof.

Lubing Wang, who provide me great help and guidance in my initial stage of research.

Finally and most importantly, I want to thank my parents for their supports and understanding.

TABLE OF CONTENTS

LIST OF TABLES

LIST OF FIGURES

NOMENCLATURE

Nomenclature

i	Intercalation reaction current density	ε_e	The volume fraction of electrolyte
β	Cathodic symmetric factor	$\mathbf{J_e}$	Li-ion flux in the electrolyte
η	Over potential	κ_s^{eff}	The effective electrical conductivity of solid phase
i_0	Exchange current density	κ_e^{eff}	The effective electrical conductivity of the electrolyte
R	Gas constant	$f_\pm$	Electrolyte activity coefficient
T	Temperature	HK	Dimensionless expansion factor function
F	Faraday constant	i_p	Exchange current density for parasitic reaction
k_a	The reaction rate constant for anode	q_{SEI}	Accumulated charge of Li lost
k_c	The reaction rate constant for cathode	η_{SEI}	Potential of SEI
c_s	Li^+ concentration in solid phase	A_v	Area of particles
c_e	Li^+ concentration in electrolyte	J_s	Li-ion flux
ϕ_s	Potential in solid phase	σ_h	Hydrostatic stress
ϕ_e	Potential in electrolyte	G_{I}	The tensile energy release rate
E_{ref}	Equilibrium potential of the active materials	G_{II}	The shear energy release rate
ϕ_{SEI}	Potential in Solid electrolyte interface (SEI)	ζ	Separation gap
R_{int}	Si/C interfacial resistance	t_{dch}^n	Discharging time in the n^{th} cycle
$\mathbf{i_e}$	Current density in electrolyte	$\mathbf{i_s}$	Current density in solid phase
a_s	Effective surface area per unit electrode volume	t_{dch}^1	Discharging time in the first cycle
R (a)	Radius of Si core	t	Thickness of C shell

b $(a+t)$	Radius of core-shell particle	D	Li-ion diffusivity
ε_{ij}	Total strain of Si core	ε_{ij}^{l}	Lithiation induced strain
ε_{ij}^{e}	Elastic strain	ε_{ij}^{p}	Plastic strain
V	Volume at current time	V_0	Initial volume of Si core
$\bar{c}_s$	Normalized Li-ion concentration in solid phase	$c_{\mathrm{s,max}}$	Maximum Li-ion concentration
Ω	Partial molar volume	α	Coefficient related to diffusion expansion
δ_{ij}	Kronecker delta	υ	Poison’s ratio
σ_{ij}	Stress component	E	Young’s modulus
λ	Coefficient related to boundary problem	S_{ij}	Deviatoric stress
σ_y	Yield stress	λ_p	Plastic stretch
$\dot{\varepsilon}_p$	Plastic strain rate	A	Fitting coefficient
m	Stress exponent	$\bar{J}_0$	Magnitude of applied flux
S	Surface area of Si core	C	Charging rate
σ_{rr}	Radial stress	$\sigma_{\theta\theta}$	Hoop stress
ε_{rr}	Radial strain	$\varepsilon_{\theta\theta}$	Hoop strain
u	Displacement along particle radius	σ_{rr}^{cs}	Radial stress at Si-C interface
P	Contact force	p_0	Maximum contact stress
δ	Contact placement	w	Radius of contact area
R^*	Effective radius	E^*	Effective Young’s modulus
σ_n	Normal stress at Si/C interface	d	Displacement in the RVE
G_f	Shell fracture energy release rate	G_d	Debonding energy release rate
Γ_f	Shell fracture energy	Γ_d	Interfacial energy

K	Rate constant	SOC	State of charge
V_{RVE}	Volume of RVE	c_{theo}	Theoretical Li$^+$ concentration at certain SOC in RVE
E_{ref}	Open circuit potential of the active materials	c_{act}	Actual Li$^+$ concentration at certain SOC in RVE
V_{Si}	The volume of Si in RVE (Representative Volume Element)	C_{nom}	Normalized capacity
V_C	The volume of C in RVE	C_{nom}^{d}	Normalized capacity considering core-shell debonding
λ	Si proportion related ratio	χ	Debonding ratio
μ	Chemical potential	t_{charging}	Charging time
ξ	Lame constant	$\mathbf{F}$	Deformation gradient
Σ_{ij}	Stress component in macroscale	M	Mobility
C_{ijkl}	Stiffness tensor in macroscale	α_a	Anode transfer coefficient
Ψ_{kl}	Strain component in macroscale	α_c	Cathode transfer coefficient
c_{surf}	Li-ion concentration in particle surface	c_{aver}	Average Li-ion concentration in particle

CHAPTER 1 INTRODUCTION

The high-capacity anode material is the most promising candidate for the next-generation high energy LIBs, among which Si related material is one of the most popular ones [1-3]. However, the major problem of Si-based high capacity materials is the tremendous volume change during charge/discharge cycling, which can cause a series of mechanical issues, e.g., particle fragment, debonding between particles and binders [1, 4], and among others. These mechanical failures further lead to the broken of the electrical network and capacity loss, which eventually causes a shortage of battery life and even safety issues [5]. Researchers have conducted large amounts of studies regarding the above issues trying to explain the mechanism and provide guidance on material selection and design. In this proposal, we will first briefly introduce several types of Si-related anode materials, and then the diffusion behaviors and the corresponding volume change in particle level will be discussed. Next, the mechanical failure of Si-based materials will be presented, following which the coupled effects of mechanical failure and electrochemical degradation will be introduced.

1.1 Si related anode materials

Si possesses ultra-high capacity (gravimetric capacity 4200 mAh/g and volumetric capacity 2400 mAh/cm^3) compared to the conventional graphite material (gravimetric capacity 372 mAh/g and volumetric capacity 890 mAh/cm^3) [2, 6-9]. However, the tremendous volume change during electrochemical cycling makes it impossible to use pure Si materials directly, especially in commercial LIBs. Thus, various strategies have been proposed to solve this problem, and the most successful one is nanoengineering [10]. In the past few years, various advanced nano Si-based material fabrication methodologies, such as Si nanoparticle [11-14], Si nanotube [15-17], Si nanowire [18-20], and Si thin film [21-22], have been proposed to mitigate the stress caused by the volume change. However, the volumetric capacity of electrode fabricated by the nanomaterials is low due to the inherent nano-property accompanying low tap density, which induces excessive use of binder and conductive agent [10]. Thus, another Si-based material, known as the Si/C composite material, is widely adopted because it has the advantage of nanomaterials as well as compensates for the weakness of nano-properties [10, 23-27]. There are several ways to form the Si/C composite material, as shown in Fig. 1. Si/C core-shell particle is one type of structural material [28-30], and based on which the yolk-shell particle [31-34], dual shell particle [35-37], multicore-shell particle [37-38], and hollow core-shell particle [39-41] have also been proposed (Fig. 1 (a)). Here, C material serves as the shell in these structural materials to limit the volume change of the Si core. A simpler way to form the Si/C composite material is directly mixing Si particles with C (or graphite) particles [10, 42-44] (Fig.1 (b)). Sometimes, the core-shell particles or other structural materials are also used to mix with C particles to form the hierarchical Si/C composite material [45], as shown in Fig. 1 (c).

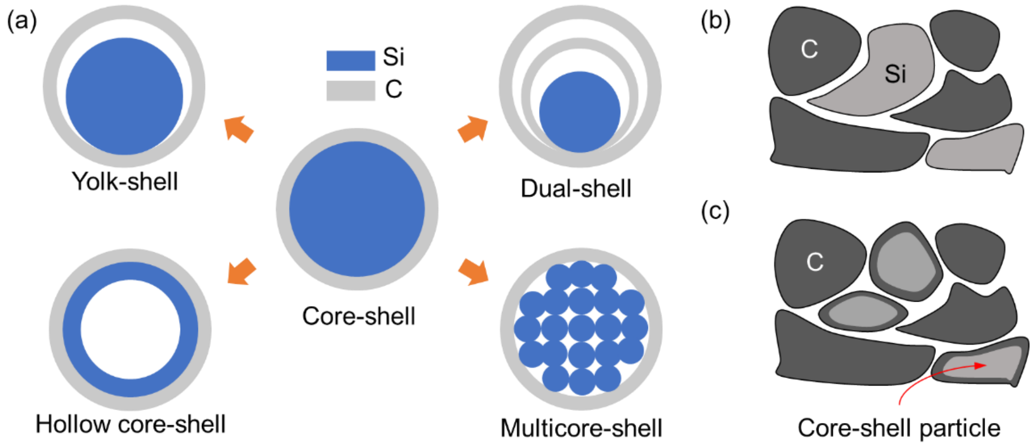

Figure 1 Various Si/C composite materials. (a) five representative structure-design particles based on core-shell particle; (b) mixture of Si particles and C particles as a kind of Si/C composite; (c) mixture of Si/C core-shell particles and C particles as a kind of hierarchical Si/C composite.

1.2 Diffusion behavior and the corresponding volume change

For active materials of LIBs, Li^+ diffusion is the major process at particle level when the battery is in charging/discharging, which finally produces the special and temporal distribution of Li^+ in active particles. The Li^+ concentration within active particles is highly related to the electrochemical performance (e.g., voltage, current) at the cell level. Thus, the diffusion behavior at the particle level is usually used to discuss the electrochemical property [46-48]. Also, the tremendous volume change of high-capacity material is dominated by the diffusion of Li^+, which in return affects the diffusion behavior as well [49-50]. It is essential to study the mechanism of the coupling behavior of Li^+ diffusion and volume change in such materials.

The diffusion behavior of pure Si particles can be *in-situ* observed by scanning electron microscope (SEM) or transmission electron microscope (TEM) [51-55]. This methodology was first proposed for SnO nanowire LIBs, which provides very clear images about the whole process of lithiation in SnO nanowire [51]. Then this technique was applied for Si-based materials, and the corresponding experiments indicate the diffusion process in such materials [52, 56-57], as shown in Fig.2. During the charging process, the volume expansion of Si particle can also be captured, which is caused by the alloying of Si and Li^+ and can be up to ~400% [57-59] (Fig. 2), leading to the particle fracture. This is the main barrier for Si to be widely used for high energy LIBs. As mentioned above, Si/C composite material is proposed to solve the volume expansion problem by using C as the exterior shell to limit the deformation of the Si core. However, the lithiation process in Si/C composite material is much more complicated and needs to be further investigated. Some recent researches have demonstrated that the diffusion process in composite materials is highly related to the potential equilibrium of each component material [60].

The *in-situ* characterization serves as an efficient way for deformation observation during electrochemical cycling, but the stress measurement in nanoscale is extremely difficult. The multibeam optical stress sensor (MOSS) was proposed to measure the stress in the thin-film structure [61-64]. However, measuring the stress in nanoparticles is hard, not to mention the composited particles. Hence, the theoretical modeling and numerical simulation are considered to be used to support the experimental data for further investigation of the whole diffusion process.

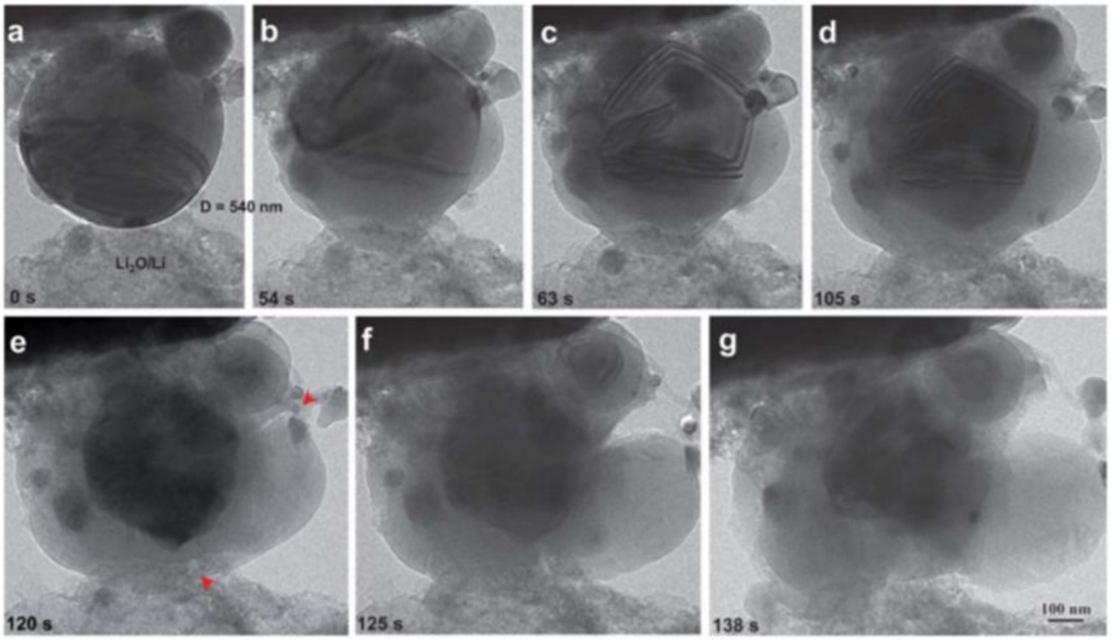

Figure 2 *In-situ* observation of the diffusion process in Si particle [52].

Two key models were adopted in almost all the studies of the relevant topics, that are the Fick's law for diffusion and classical mechanics theory for stress/strain evolution [65-70]. Fick's second law is also one basic sub-model used in the widely recognized battery model known as the Newman Model. It serves as the diffusion model for Li^+ insertion into active particles, which can calculate the Li^+ concentration within the active particle both for spatial distribution and temporal evolution. The basic model can be written as:

$$\frac{\partial c}{\partial t} + \nabla \cdot \mathbf{J} = 0 \tag{1}$$

where c is the Li^+ concentration and $\mathbf{J}$ is the Li^+ flux. Based on the specific case, this model can be further developed into the desired one. For the mechanical model, the equilibrium equation is adopted as

$$\nabla \cdot \mathbf{T} + \mathbf{B} = 0 \tag{2}$$

where **T** is the nominal stress calculated by $\mathbf{T} = \mathbf{C} : \mathbf{E}$, with stiffness matrix **C** and elastic strain matrix **E**, and **B** is the body force. According to the multiplicative decomposition law, the total deformation can be expressed as

$$\mathbf{F} = \mathbf{F_e} \cdot \mathbf{F_p} \cdot \mathbf{F_l} \tag{3}$$

where **F** represents the deformation gradient, and the subscripts "**e**", "**p**", and "**l**" represent elastic distortion, plastic deformation, and diffusion-induced volumetric deformation, respectively. The diffusion-induced volumetric deformation is related to the Li^+ concentration, *c*, which can be written out as

$$\mathbf{F}_l = \frac{\Omega}{3} \Delta c \tag{4}$$

where the Ω is the partial molar volume of Si. Through this equation, the electrochemical model and mechanical model are coupled. For core-shell particles, the diffusion model and mechanical model just need to be considered separately for core and shell with specific boundary conditions at the surface and core-shell interface.

Based on the above basic models, a few improvements have been developed to broaden the application range, such as the plasticity [71-72] and rate-dependency [73-74] in the mechanical model. The theoretical model has some limitations that the analytic solution can only be solved for the regular shape (e.g., sphere, cylinder) and single or two simply contact objects. For example, if we want to study a representative volume element (RVE) that contains many irregular active particles, binders, and electrolytes, the theoretical method is not efficient anymore. Then, the numerical simulation is a powerful tool to achieve the study of those complex cases based on the fundamental theories.

Numerical simulation methodology is originally used for the parametric study of single particles, which guides geometry and property design. Then, numerical simulation was applied to study the more complex cases, e.g., composite electrode [75-76] and multiscale[45, 77-79]. A multicomponent system based on imaging technique was established to study the effects of particle shape, particle size, particle distribution, binder stiffness, and porosity, as well as the coupling effects of mechanical expansion and electrochemical performance [70, 80-81]. Also, numerical simulation serves as a powerful tool to help to explain mechanisms based on simplifications [10].

In our previous study, the contact behavior between two Si/C core-shell particles was studied by numerical simulation considering plasticity and strain-rate effects(Fig. 3), which provides guidance on the design of Si/C core-shell particles with consideration of the shell thickness and shell modulus [73]. Based on this model, a multiscale-multiphysics model was established to study the multiphysics behavior of hierarchical Si/C composite anode (Fig. 4) [45]. The effects of Si proportion, mechanical constraint, and the charging rates were analyzed by the model, providing guidance on the corresponding design of the Si/C composite anode.

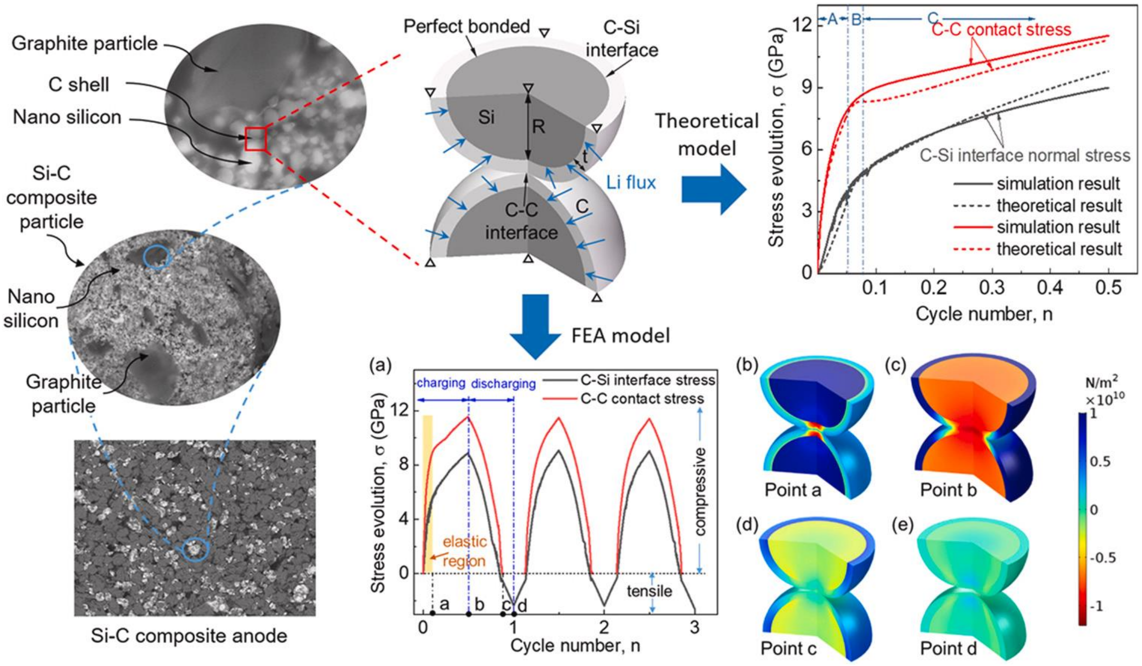

Figure 3 A numerical study about the contact behavior between two Si/C core-shell particels [73].

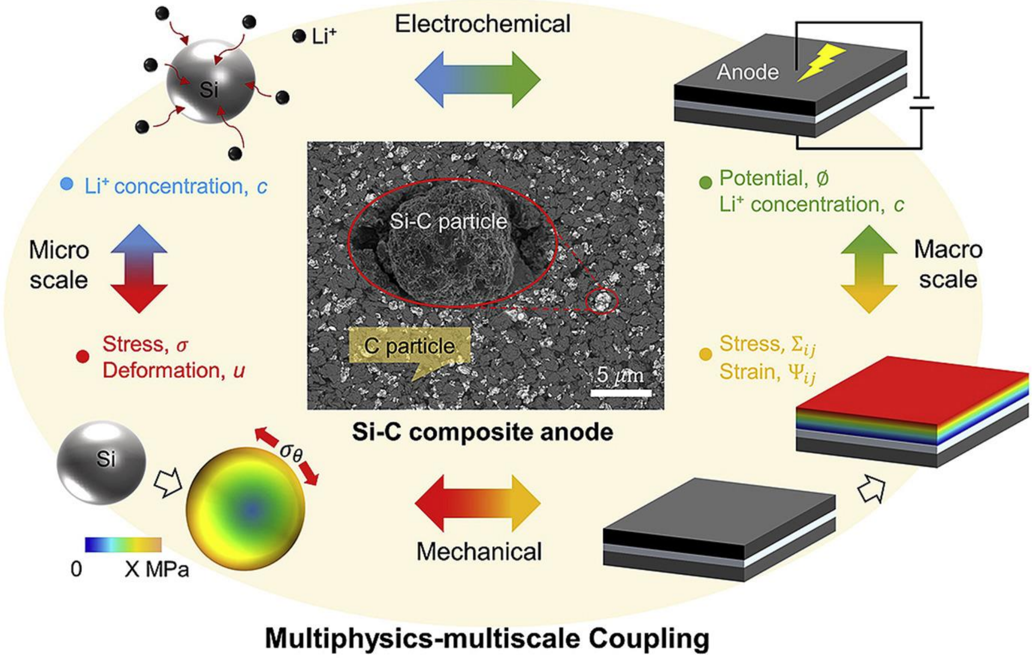

Figure 4 The concept of the Multiphysics-multiscale modeling of Si/C composite anode [45].

1.3 Mechanical failure behaviors

During the charging/discharging cycling of the battery, the Si-based active particles produce a large volume change, which further leads to the failure behavior after accumulation [82]. We mainly consider the mechanical failure caused by cracks which can be further classified as pure particle fracture, shell fracture, and core-shell debonding [83]. The last two failure modes mainly refer to the core-shell-based structural particles. The cracks generated during the electrochemical cycling grow and propagate through the whole active particle, which further leads to the fracture of the particle. The fragments produce new surfaces of the particles and cause the formation of new solid electrolyte interfaces (SEIs), which may cause capacity losses in terms of electrochemical performance [84-86]. Besides, mechanical debonding occurs in the interface of active particles and binders, which destroy the electric networks.

It has been demonstrated that the fracture of Si particle has strong size dependence through the *in-situ* test where crack only appears in the particle with a diameter greater than 150 nm [87-89]. This is the motivation for nanoengineering and other small-size techniques to be applied in Si-based materials. However, the contact force among particles in the electrode level still causes particle failure; even the particle size is below the critical value. Thus, materials based on the structural re-design, e.g., core-shell particle, yolk-shell particles, have attracted more interest in recent years [90]. The results of the *in-situ* observation of the cycling behavior of core-shell related particles show that shell fracture and core-shell debonding are the two main failure modes, which should be the key factors that need to be considered during the structure design [5].

Based on the experimental results, the energy release rate theory of fracture mechanics was adopted to analyze the failure behavior of the core-shell related particles [91-93]. For shell fracture of the spherical particle, the energy release rate, G_f can be written out as:

$$G_f = Z \frac{(\bar{\sigma}_{\theta\theta})^2}{E_2}(b-a) \qquad (5)$$

where the E_2 is Young's modulus of the shell, $\bar{\sigma}_{\theta\theta}$ is the mean value of hoop stress in the shell, Z is a dimensionless factor which is 2 for the spherical shell, and b-a is the shell thickness. Similarly, for the core-shell debonding, the energy release rate, G_d is

$$G_d = \pi \frac{(\sigma_{rr}^{cs})}{E_e}(b-a) \qquad (6)$$

where the σ_{rr}^{cs} is the normal stress at the core-shell interface, and E_e is the equivalent modulus. Once the energy release rate exceeds the corresponding critical value (also called the fracture toughness) of the material, failure occurs. This theory is very convenient for the analysis of single particles that are symmetric and provides guidance on the geometry and material property design towards excellent mechanical robustness. In our current study, this theory was applied to investigate the electro-chemo-mechanical performance of five representative nanostructures (see Fig. 1 (a)) based on the multiphysics modeling trying to figure out the optimal Si/C nanostructural configuration (Fig. 5).

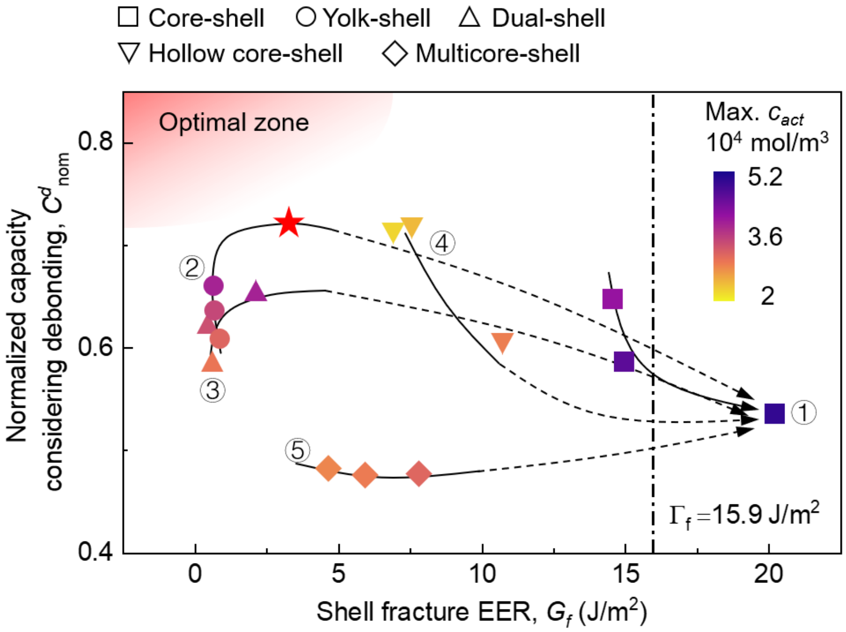

Figure 5 A design map of five representative nanostructures towards optimal electrochemical performance and mechanical robustness. (in submission)

However, when considering the behaviors in the electrode or higher level, which contains lots of particles and contact pairs, numerical simulation is a better way than theoretical analysis. The cohesive element and phase-field model are the most common methods in crack modeling [5, 94-96]. They can be either used in single particle analysis with consideration of various effective factors or applied for electrode (multicomponent) level study.

1.4 Mechanical failure and electrochemical performance coupling

As mentioned above, mechanical failure has a strong relationship with electrochemical performance. The relationship between mechanical failure and electrochemical degradation can be qualitatively investigated by *in-situ* observation and electrochemical tests [2, 87, 97-100]. The capacity fade is demonstrated by the cycling test of the cell, and when taking out the cycled electrode and putting it under the microscope, various fractures can be seen, e.g., crack, debonding, and SEI formation [98, 101-103]. However, it still lacks to figure out the quantitative relationship between mechanical failure and electrochemical performance, especially during cycling. Recently, researchers proposed a model to describe the relationship between the interfacial resistance and the interfacial gaps based on imaging technique and electrochemical tests [5, 104], as shown in Fig. 6. It is still unknown how the active particle behaves after the crack happens either in the particle or in the shell. Many fundamental issues remain to be solved, such as the diffusion behavior after the crack occurs and the diffusion behavior through the crack. Also, the multiscale coupling needs to be considered because the electrochemical performance we care about is usually at the cell level and above, while the crack and failure behavior usually happens at the particle level.

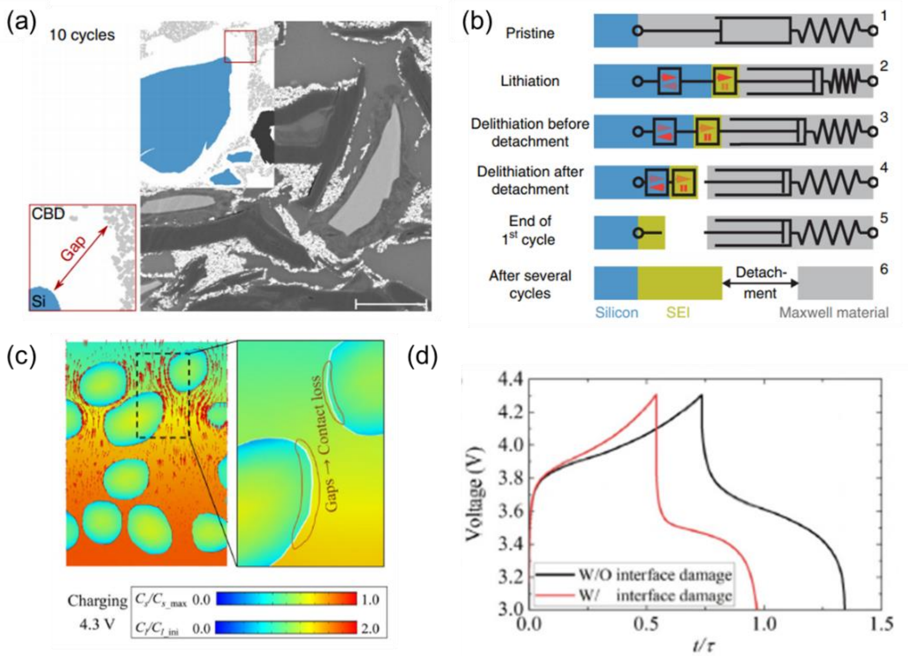

Figure 6 (a) Cross-sectional backscatter electron microscopy image with the corresponding multi-phase segmentation for a Si/C electrode after 10 cycles, and (b) the sketch of the fundamental components of the Maxwell model for gap effects [104]; An application of the model in (b) for coupling analysis of an electrode RVE and the (d) corresponding results of voltage profile with/without gap effects [5].

1.5 Challenges and motivation

As mentioned above, in the past few decades, experimental methods, and theoretical and numerical studies have been reported, providing us preliminary understanding of the multiphysics behaviors of LIBs. The multiphysics behaviors at particle level have been widely discussed by modeling method regarding to Si particle or Si/C core-shell structure. However, these studies mainly focus on single particles while little efforts have been spared on multi-particle systems. Also, the multiscale problems about the electrochemical-mechanical failure coupling effects in the Si/C composite anode materials remain unclear, which limits the broad application of this kind of material. In addition, the current models cannot consider the multiscale problems with consideration of failure behavior in an efficient way. Thus, in my thesis work, I will develop the multiphysics model of Si/C composite particle behaviors based on the fundamental understanding of Li diffusion in Si/C system from the DFT simulation, as well as the establishment of the relationship between the mechanical failure and electrochemical performance. Then, the multiphysics model at the particle level will be scaled up into the electrode level to form the multiscale model, which can be used to study the multiphysics behavior from cell level to particle level, providing design guidance and powerful tools of the LIBs with Si/C composite anodes.

CHAPTER 2 DIFFUSION BEHAVIOR AND MECHANISM

In this chapter, the Li diffusion properties in the Si/C composite is studied by the first principle calculations. Two representative modes (mixture mode and core-shell mode) of the Si/C composite anode are considered. The structural evolution of the lithiated Si/C composite during the lithiation process is firstly investigated. Then, the volume change and Li diffusivity under lithiation are studied. The effects of various C layer thicknesses on Li diffusion in Si/C composite are also presented, and the enhancement mechanism of the C materials on Li diffusion in Si is revealed. This study provides a fundamental understanding of the Li diffusion in Si/C composite considering both the mixture mode and core-shell mode and contributes to the guidance on next-generation anode material design and development.

2.1 Computational method

The diffusion behavior of Li in the Si/C composite system is investigated by density functional theory (DFT) calculations implemented in the Vienna *ab initio* package (VASP). [105] The projector augmented wave (PAW) method [106] is used to describe the interaction between core and valence electrons, and the generalized gradient approximation (GGA) [107] based on the Perdew-Burke-Ernzerhof (PBE) [108] function is applied for the electron exchange-correlation. An energy cut-off of 300 eV is used for the expansion of plane waves. Before the diffusion process modeling, all the structures used in the following Ab initio molecular dynamics (AIMD) simulations are optimized using the conjugate gradient method until the residual force is less than 0.01 eV/Å, and the convergence of energy change per atom is less than 10^{-4} eV. A sufficient k-point mesh of 3×3×1 in scheme of Monkorst-Pack for integration of Brillouin zone is used. Then, to simulate the Li diffusion and chemical lithiation processes, the AIMD simulations with Ganonical ensemble (NVT) within the framework of DFT are performed at the temperature of 1200 K. A time step of 1 fs is used, and the Nose–Hover thermostat is used to control the temperature.

All the unit cells share the same length and width of 10.86 Å×10.86 Å, while the height of the unit cells range from 23.78 Å to 28.68 Å to make sure the vacuum spaces are the same as 14 Å (Figs. 7 (a)-(e)). All the unit cells consist of 64 Si atoms that are relaxed from the 2×2×2 crystalline Si (c-Si) supercell. There are 36, 56, and 76 C atoms for the Si/C composite structures with a-C layer thicknesses of 2 Å, 3 Å, and 4 Å, respectively. Here, we define the structures with 2 Å, 3 Å, and 4 Å of C layer thicknesses as Si/C (2), Si/C (3), and Si/C (4), respectively. The C layer initial structures are cut from the amorphous C material from the Materials Studio (MS) library and fully relaxed before being placed on the surface of Si atoms. The initial Si/C interfacial gap is set as 1.5 Å, which is optimized as the slab model with 14 Å vacuum space to ensure minimal interfacial energy after the relaxation process. 62 amorphous Li atoms are then filled in the vacuum space above the C layer, and periodic boundary conditions were applied in all three directions. This periodic boundary condition enables the Li atoms diffusion from both the top of C layer and the bottom of Si lattice if the bottom atoms are free.

Two typical configurations of Si/C composite anodes are considered in this study (Fig. 7 (f) and (g)). One is defined as mixture mode (Fig. 7 (f)) where the Si and C materials are simply mixed, and the Li atoms can diffuse into either Si or C randomly and freely. For this mode, the bottom Si atoms were set to be free during the AIMD calculations. The other one is called core-shell mode (Fig. 7 (g)) where the Si is wrapped by the C material such that the Li atoms can only pass through the C shell to diffuse into the Si core. For this mode, the bottom Si atoms were fixed in all directions during the AIMD calculations. 25 ps and 60 ps were applied as the running time for the mixture mode and core-shell mode, respectively, which are proven sufficient for the mixing of Li, Si, and C atoms. Then, the Mean square displacement (MSD) of the Li atoms as a function of time was calculated to analyze the diffusivity of Li atoms in various Si/C composite structures.

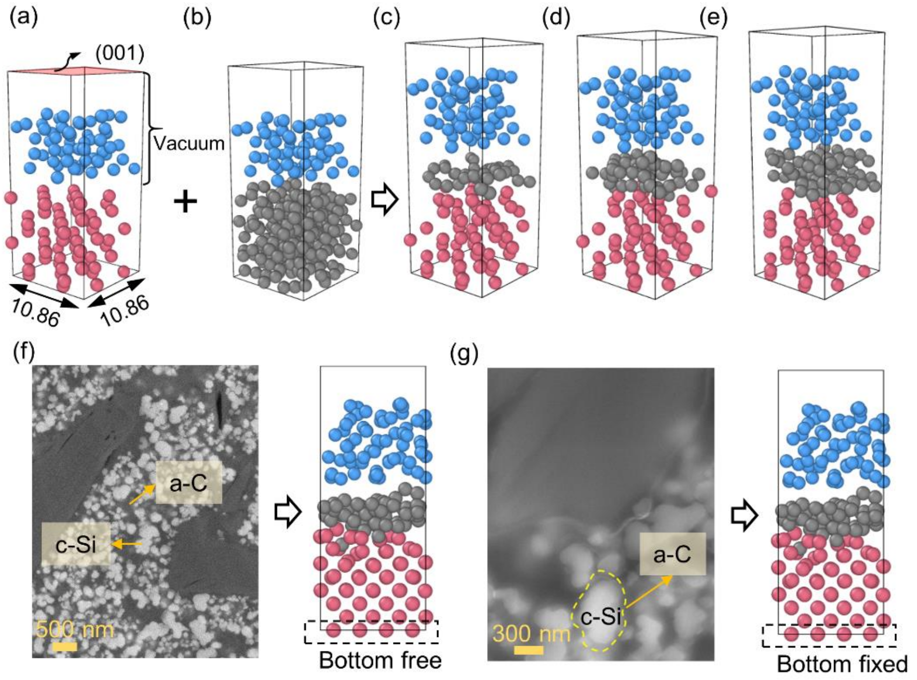

Figure 7 Atomic structures of (a) c-Si, (b) a-C, and the corresponding Si/C composite

composed with these two materials, with various a-C layer thicknesses of (c) 2 Å (d) 3 Å (e) 4 Å. The definition of two composite mode in this study: (f) mixture mode (bright particles are c-Si and dark particles pointed out by the arrow are carbon black (a-C)) and (g) core-shell mode [73]. (Si: red dot; C: black dots; Li: blue dots)

2.2 Li diffusion behavior in pure bulk c-Si and a-C material

Before investigating the Li diffusion behavior in Si/C composite material composed with c-Si and a-C, the Li diffusion in these two raw materials was first studied. The evolution of the structure during Li diffusion in c-Si was analyzed by the radial pair distribution function (RDF) (Figs. 8 (a)-(c)). It reveals that the numbers of both Si-Si and Li-Li pairs decrease during the Li diffusion, while the number of Li-Si pairs increases, indicating that both the Si-Si bonds and Li-Li bonds are interrupted, and Si atoms and Li atoms are attracted to form the Si-Li bonds. The amorphization phenomenon can be observed during the lithiation process in c-Si, which leads to the formation of the a-LiSi phase (Fig. 8 (d)). This process is completed around 3 ps, after which the peaks become almost constant. This amorphization can also be demonstrated that the g (r) graphs of Si-Li and Li-Li pairs in this c-Si are very similar to the corresponding graphs of a-Si after ~3 ps in Ref. [109].

For the a-C material, the final structure after 25 ps of lithiation indicates that the Li diffusion in bulk a-C material is not sufficient with this simulation time (Fig. 8 (e)). This is because the Li diffusion in carbon material usually demands an ion channel formed by the C matrix, like the layered structure in graphite and multi-layer graphene [110]. However, the a-C structure in the present study is more like a complex disordered network, which provides few opportunities for Li atoms to diffuse in. Thus, a-C material is usually used as the additional material to improve the diffusion or structural performance of the composite structure materials, like the coating layer and shell layer in some coated particle and core-shell particle anodes [14, 111].

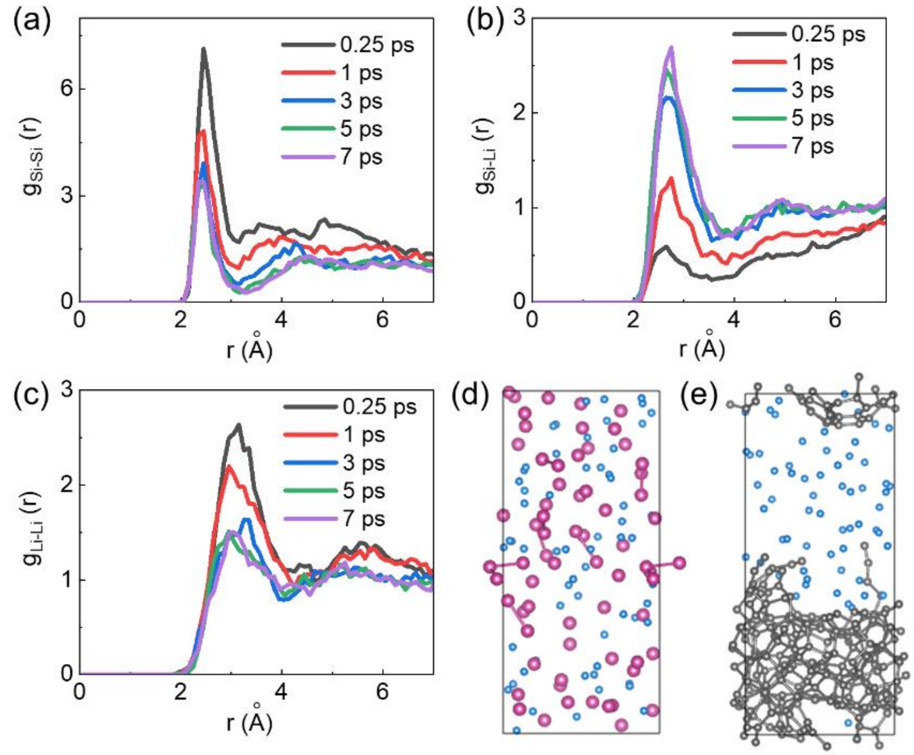

Figure 8 The radial pair distribution function g(r) at 1200 K for (a) Si-Si pair, (b) Si-Li pair, and (c) Li-Li pair at various stages of lithiation, as shown by time steps. The final structures after 25 ps of lithiation process of (d) c-Si and (e) a-C materials. Here in (d) and (e), the atoms in pink, grey, and blue are Si atom, C atom, and Li atom, respectively.

2.3 Li diffusion behavior in Si/C composite material

The structure changes of Si/C composite materials of both the mixture mode and core-shell mode with various C layer thicknesses during the lithiation process are first analyzed. For the mixture mode (Fig. 9), the Li atoms tend to diffuse into Si and C simultaneously, especially in the Si/C (2) and Si/C (3) (@1 ps in Figs. 9 (a) and (b)), while the Li atoms diffuse into Si first for the Si/C (4) (@1 ps in Fig. 9 (c)). This depends on the atomic structure of the C layer. For the Si/C (2), the Si is not completely covered by the C layer. Thus, some initial voids allow the Li atoms to pass through the C layer more easily. For the Si/C (3), although the Si is completely covered by the thicker C layer compared with the Si/C (2), the Li atom can still easily pass through the C layer via the ion channels formed during the relaxation process. These ion channels in the Si/C (3) are parallel to the Li diffusion direction. For the Si/C (4), ion channel (or layered structure) can also be observed during the relaxation, which, however, is perpendicular to the Li diffusion direction. Thus, it is difficult for the Li atoms to pass through the C layer in Si/C (4) such that the Li atoms tend to diffuse into Si directly from the bottom instead. Overall, the Li atoms are observed to diffuse gradually into the Si material by breaking and expanding the Si-Si bonds. The C layer structure is also expanded during the lithiation process, and some of the C-C bonds are interrupted. The expansion behavior will be quantitively analyzed in the following section. The Li, C, and Si atoms are completely mixed at around 14 ps, indicating that 25 ps is sufficient for the lithiation process in Si/C composite material as mixture mode.

For the core-shell mode (Fig. 10), the Li atoms are forced to diffuse into Si by passing through the C layer first. Thus, the diffusion speed highly depends on the C layer structure in this mode. According to the analysis above for the mixture mode, the Li atoms pass through the C layer faster in the Si/C (2) and Si/C (3) compared with the Si/C (4), demonstrated by the structures at 14 ps and 28 ps in Fig. 10. The Li, C, and Si atoms are completely mixed at around 50 ps, indicating that 60 ps is sufficient for the calculations in the core-shell mode.

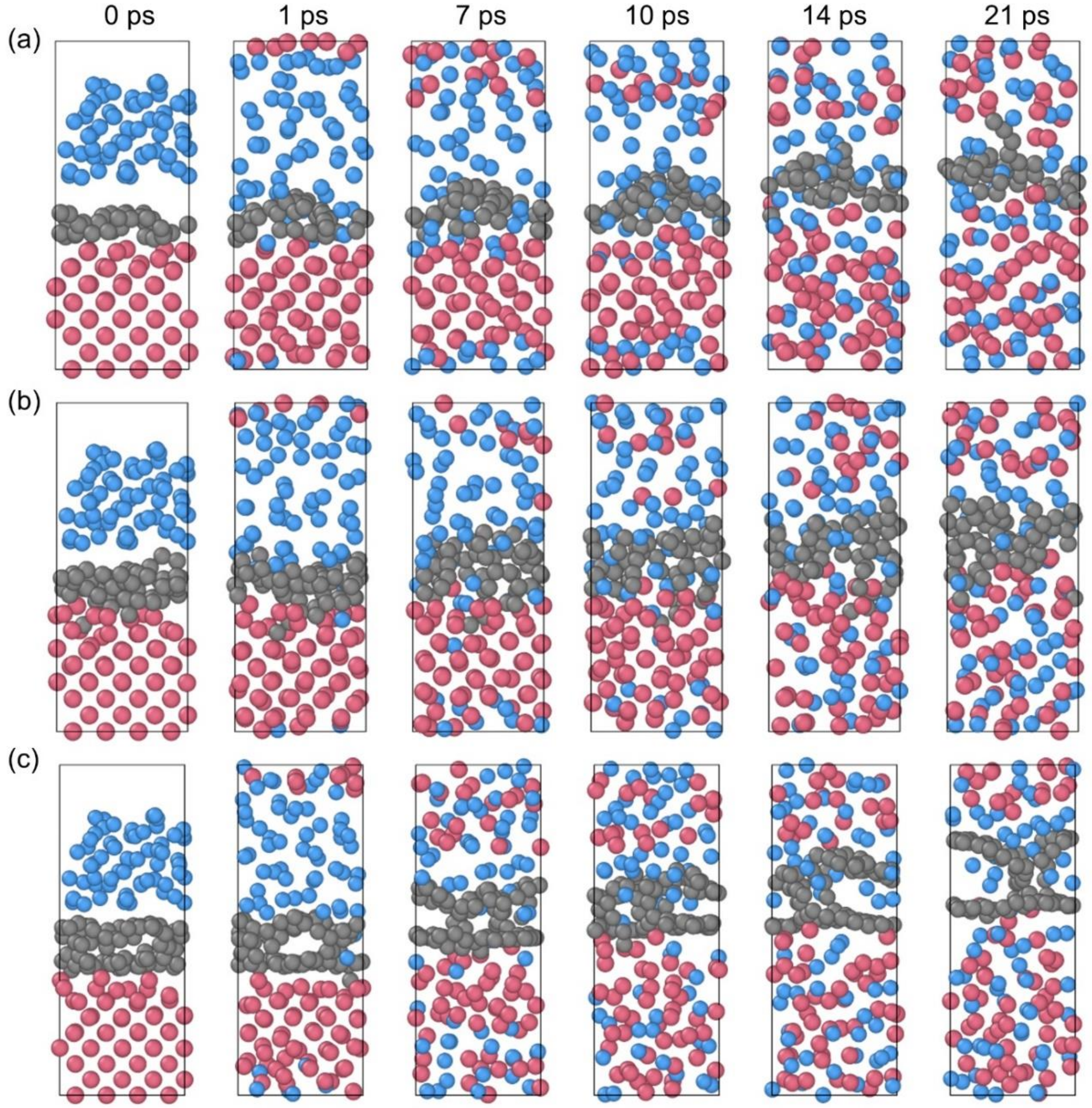

Figure 9 Structural snapshots of Li diffusion in Si/C composite systems (mixture mode) at 1200 K with C layer thicknesses of (a) 2 Å (b) 3 Å (c) 4 Å, respectively, at various simulation times during the lithiation process.

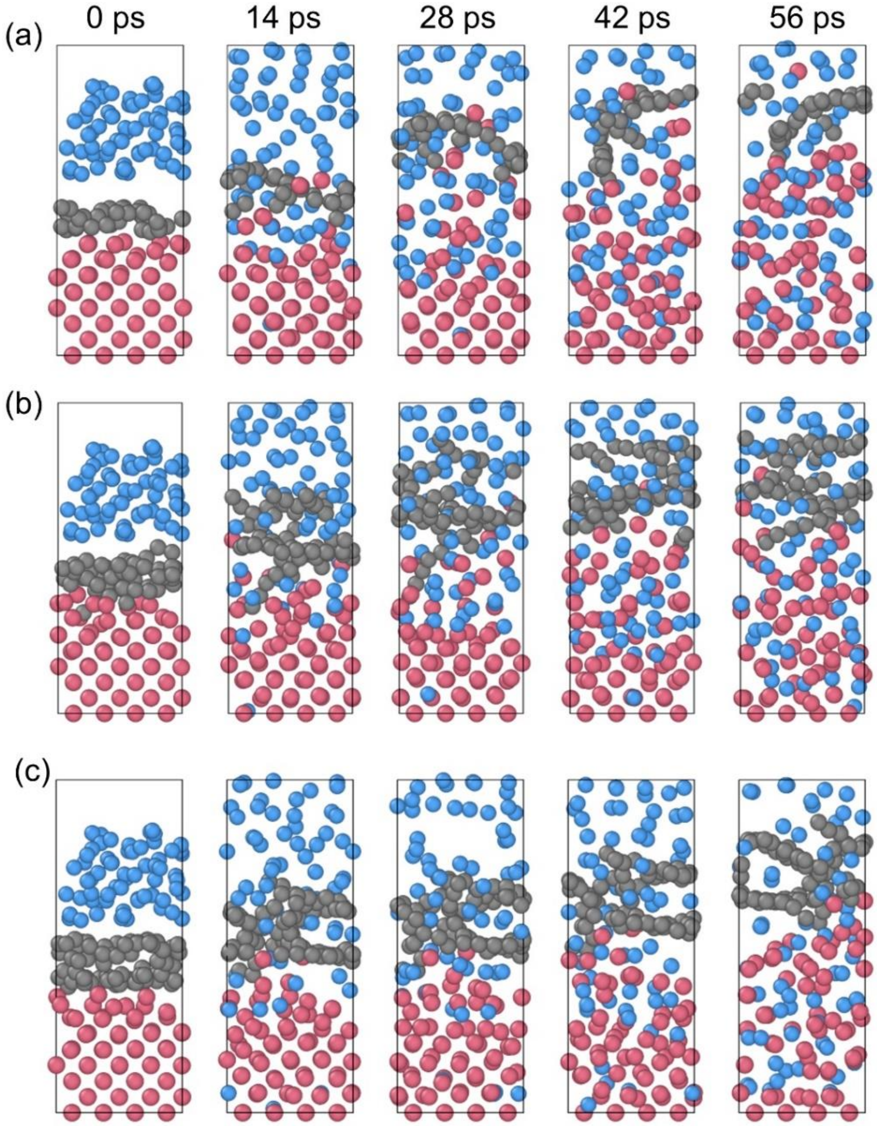

Figure 10 Structural snapshots of Li diffusion in Si/C composite systems (core-shell mode) at 1200 K with C layer thicknesses of (a) 2 Å (b) 3 Å (c) 4 Å, respectively, at various simulation times during the lithiation process. Pink, gray, and blue represent Si atoms, C atoms, and Li atoms, respectively.

To further analyze the structural change during the lithiation process, the RDF is calculated for both two modes (Figs. 11 and 12). For the mixture mode, the RDF plots of Si-Si pair in the initial structures with various C layer thicknesses show an obvious crystalline characteristic with several RDF peaks (Fig. 11 (a)) and are almost overlapped because the initial Si-Si lattice in all the three structures is almost identical. After the full lithiation process, the RDF plots change from crystalline characteristic to the amorphous one for all three structures. The peaks of RDF for Si-Si of all the three structures slightly shift from 2.35 Å to 2.45 Å due to the charge transfer from Li to Si [112]. If we look into the dot lines in Fig. 11(a), a slight difference of the peak values among the three structures can be found. This can be further explained by the Si/C interfacial structures (Fig. 11 (c)) that the formation of Si-C bonds during the lithiation causes the decreasing of Si-Si bond numbers. Different amounts of Si-C bonds form among three structures during the lithiation due to the variety of the initial C layer atomic structures. Thus the numbers of Si-Si bonds are different among the three structures. For instance, the C atomic structure in Si/C (4) shows a horizontally layered structure that provides less facially free C atoms to bond with Si, consequently leading to a larger amount of Si-Si bonds. The positions of RDF peaks for Si-Li, C-Li, and Li-Li are 2.7 Å, 2.25 Å, and 3.05 Å (Fig. 11 (b)), respectively, that are consistent with the literature [113]. An obvious difference of peak values for the C-Li bonds among three structures can be seen from the dash lines in Fig. 11 (b). This can be explained by the local atomic structures extracted from the three unit cells (Fig. 11 (d)). For the Si/C (2), most of the Li atoms are absorbed on the surface of the C layer instead of inserting into it, which means part of the C-Li bonds should not be counted. For the Si/C (3), a large number of Si-C bonds at the Si/C interface leaves no space for Li atoms to combine with C atoms, thus the number of C-Li in Si/C (3) is the least among three structures. For Si/C (4), the layered structure in C layer and the void at the Si/C interface provide the storage space for Li atoms, which causes the relatively large number of C-Li bonds.

For the core-shell mode, the crystalline characteristic can also be found for the initial structures while the second peaks of Si-Si bonds decrease but keep there for all the three structures after lithiation due to the fixed Si atoms at the bottom (Fig. 12 (a)). The first peaks of RDF for Si-Si of all the three structures also shift from 2.35 Å to 2.4 Å. The positions of RDF peaks for Si-Li, C-Li, and Li-Li are 2.75 Å, 2.25 Å, and 3.05 Å (Fig. 12 (b)), respectively, that are very similar to the mixture mode. To explain the differences of the peak values of Si-Li bonds and C-Li bonds among the three structures, we analyze the local atomic structures near the Si/C interface in Fig. 12 (c). During the lithiation process, the atomic structures of the C layer evolve differently from the different initial structures among the three Si/C composite structures. Different from the mixture mode, the Si/C (2) and Si/C (3) of core-shell mode generate obvious voids at the Si/C interface, while the void in the Si/C (4) is relatively small. Besides, the C layers in both the Si/C (3) and Si/C (4) develop the layered structure in different directions that provide spaces for Li atom storage. Thus, the Si/C (3) exhibits the largest C-Li peak value since it possesses both the interfacial void and layered space in the C layer, while the Si/C (2) and Si/C (4) share similar C-Li peak values. The peak values of the Si-Li pairs show the opposite trend to the C-Li pairs because the more stored Li atoms in the C layer leads to fewer Li atoms diffusion into Si.

It reveals that the atomic structures of the C layer and the Si/C interface change more during the lithiation in core-shell mode than in mixture mode. This is because that all the Li atoms must pass through the C layer to diffuse into Si in core-shell mode, which constantly affecting the atomic structures of the C layer and Si/C interface in the whole lithiation process, while only part of the Li atoms can diffuse into Si directly in mixture mode, which partially reduces the effects on structural change of C layer and Si/C interface.

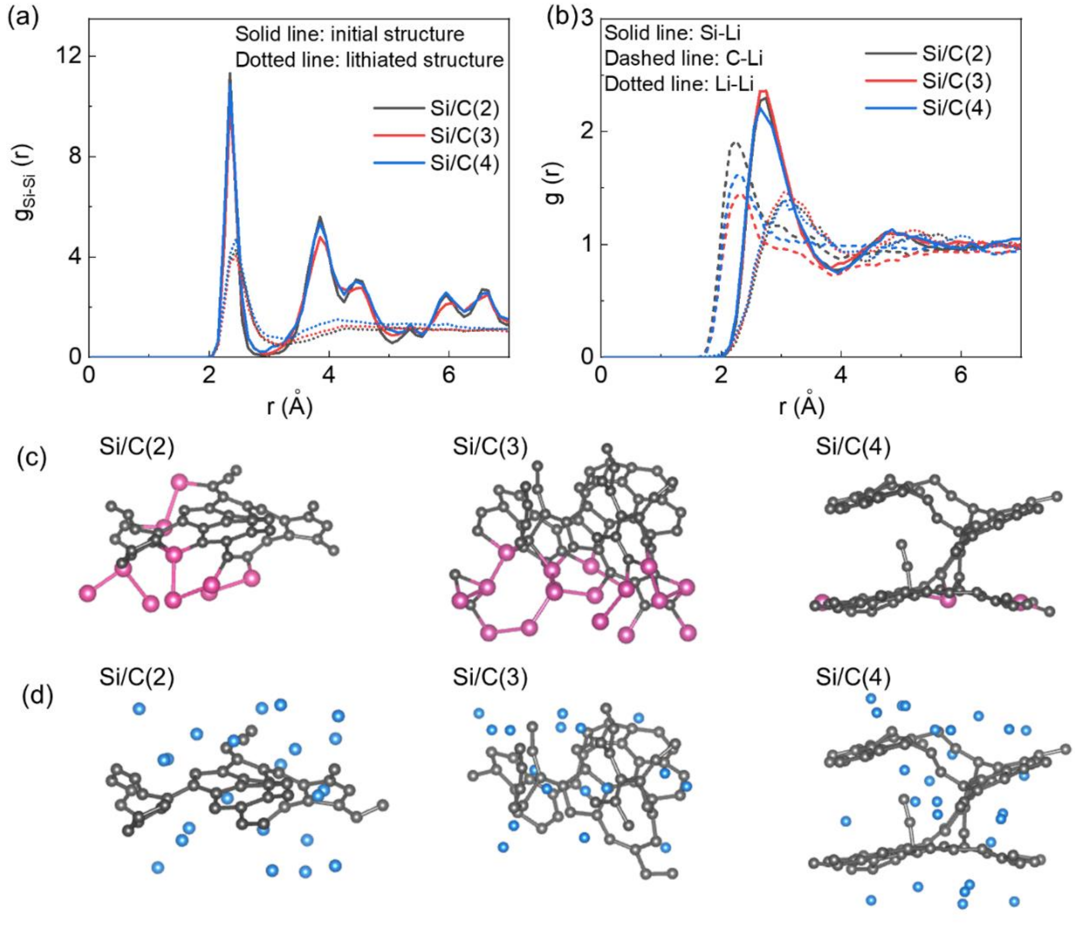

Figure 11 The RDF at 1200 K for (a) Si-Si pair at both the initial state and the lithiated structure, and (b) Si-Li, C-Li, and Li-Li pairs in lithiated structures of Si/C composite system (mixture mode) with various C layer thicknesses. The Si/C interfacial structures from the fully lithiated Si with various C layer thicknesses are shown in (c), while the Li atoms distributions in C layer with various C layer thicknesses are shown in (d). Pink, gray, and blue represent Si atoms, C atoms, and Li atoms, respectively.

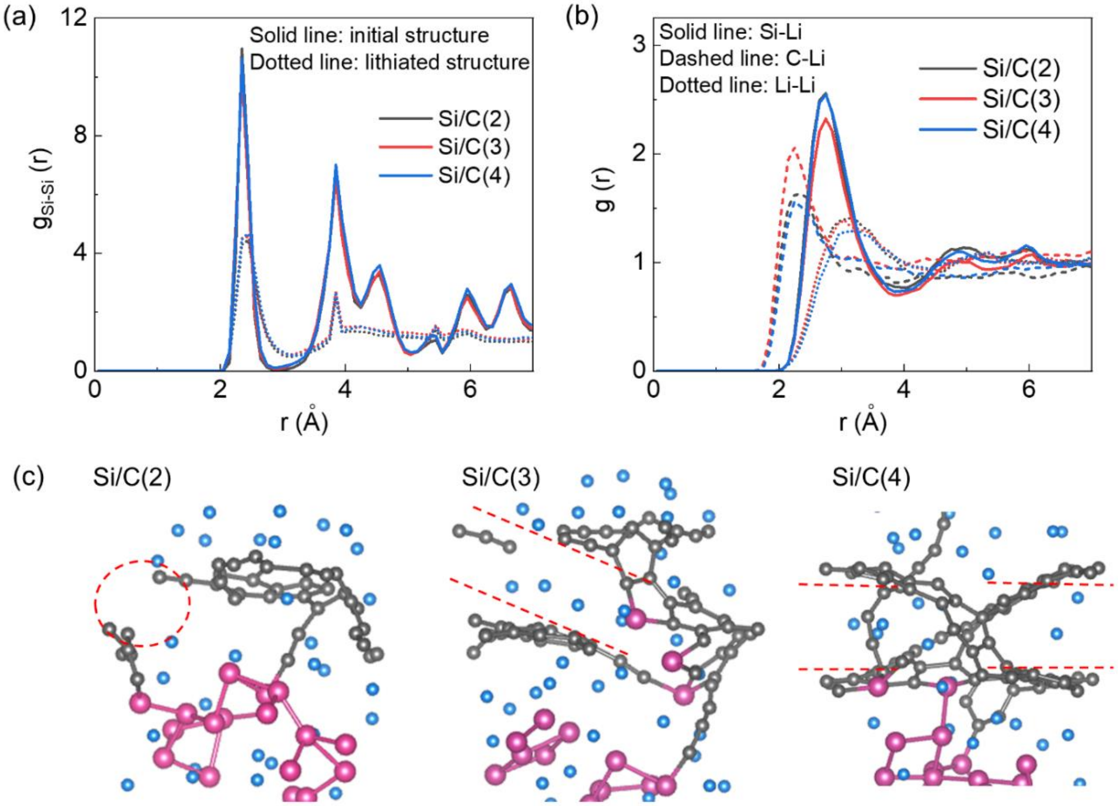

Figure 12 The RDF at 1200 K for (a) Si-Si pair at both the initial state and the lithiated structure, and (b) Si-Li, C-Li, and Li-Li pairs in lithiated structures of Si/C composite system (core-shell mode) with various C layer thicknesses. The Li distributions in C layers and near the Si/C interfacial structures from the fully lithiated LiSi with various C layer thicknesses are shown in (c). Pink, gray, and blue represent Si atoms, C atoms, and Li atoms, respectively.

The volume changes after the lithiation process of all the structures in two modes are also analyzed (Fig. 13). The initial thicknesses of the C layer and Si layer are defined as t_C^0 and t_{Si}^0, respectively, while the corresponding final thicknesses are t_C and t_{Si} (Fig. 13 (a)). Then, the volume expansion ratios of the C layer, Si layer, and the Si/C structure are calculated as t_C / t_C^0, t_{Si} / t_{Si}^0, and $\left(t_C + t_{Si}\right) / \left(t_C^0 + t_{Si}^0\right)$, respectively. It is demonstrated that both two modes show the same tendency of volume expansion, i.e.,a thicker C layer produces a smaller volume expansion in terms of Si layer and Si/C structure (Fig. 13 (b)).

Nevertheless, the volume expansion of the Si layer in the core-shell mode is ~7% smaller than that in the mixture mode for all the three C layer thicknesses. This is because the Li atoms can diffuse into Si directly in the mixture mode where the C layer restriction on Si expansion is weakened. The solid red line and red dash line in Fig. 13 (b) are almost overlapped, which means that the C layer expansion ratios are the same in the two modes. In addition, the C layer expansion ratios almost keep the same with the increasing C layer thickness. Thus, the overall Si/C structure expansion behavior is similar to that of the Si layer. It is confirmed from this study that the core-shell mode has better performance on limiting the Si volume expansion than the mixture mode.

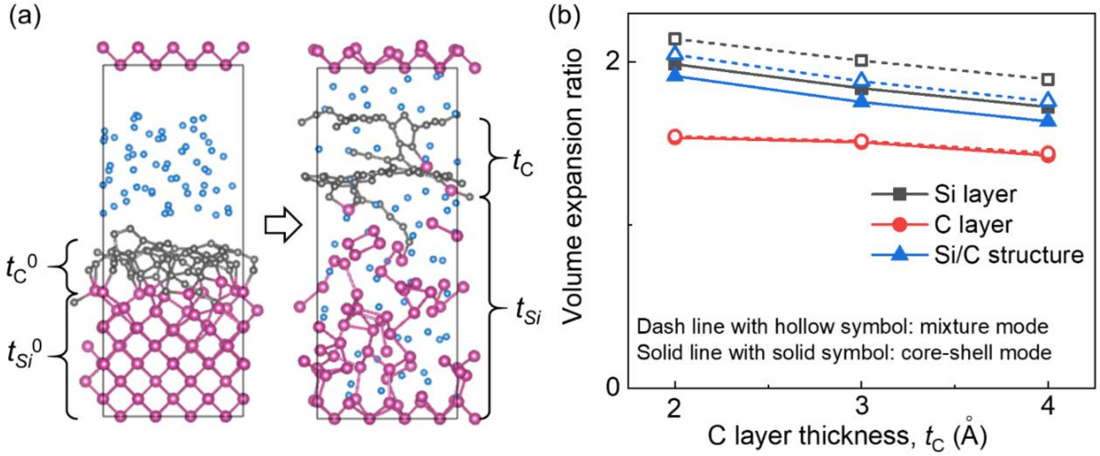

Figure 13 (a) Volume expansion parameters definition; (b) volume expansion ratio at 1200 K for Si/C composite system (both mixture mode and core-shell mode) with various C layer thicknesses.

To quantitively define the diffusivity of Li in Si/C composite materials of both mixture mode and core-shell mode, we calculate the MSD of Li atoms as a function of AIMD time steps using the following equation

$$\mathrm{MSD} = \left\langle \left| r_i(t) - r_i(0) \right|^2 \right\rangle = \frac{1}{N}\sum_{i=1}^{N} \left| r_i(t) - r_i(0) \right|^2 \tag{7}$$

where $r_i(t)$ represents the positions of the specific atom at time t during the AIMD process, N is the total atomic number and the operator '$\langle \ \rangle$' denotes the average value over all the atoms. The diffusivity at a specific temperature is determined by MSD using the Einstein relation:

$$\mathrm{D} = \lim_{t \to \infty} \frac{MSD}{nt} \tag{8}$$

where n is a constant and n = 2, 4, or 6 for one, two, or three-dimensional diffusions, respectively.

The linear fits of the MSD curves are applied within the time range that the Li atoms are fully mixed with the Si/C composite structures. Thus, the time ranges of t >14 ps and t >45 ps for the mixture mode and core-shell mode, respectively, are selected based on Figs. 9 and 10. Note that there are fluctuations at the last several Pico seconds, thus, the end part of MSD is eliminated for the linear fit (Fig. 14). According to the results of linear fit and Eq. (8), the diffusivities of Li in the Si/C composite are summarized in Table 1. The diffusivity of bulk c-Si is about $7.75\times10^{-5}\ \mathrm{cm^2/s}$ at 1200 K which is very close to the calculated values reported in the literature [109]. It indicates that the addition of C atoms as amorphous layers improves the Li diffusion in Si material up to ~170% in both mixture mode and core-shell mode. Such improvement should be attributed to the high electronic and ionic conductivities and Li diffusivity of C material. The improvement degree of Li diffusivity in Si/C composite by the addition of a-C layer is linearly related to the thickness of the C layer in mixture mode, that increasing the C layer thickness from 2 Å to 4Å slightly weakens the improvement by ~4.48%. The difference of Li diffusivity among the three structures with various C layer thicknesses is ignorable in mixture mode because the Li atoms can diffuse either through the C layer or directly into Si, which consequently leads to an overall equivalent effect on Li diffusivity of the whole Si/C composite system. However, for the core-shell mode, the Li atoms can only diffuse into Si through the C layer as we mentioned above. Thus, the C layer structures play an important role in the Li diffusivity improvement. If the C layer provides an efficient "channel" for Li atoms to pass through, like the void in Si/C (2) and the voids and layered structure parallel to the diffusion direction in Si/C (3) (Fig. 12 (c)), the Li diffusivity can be improved more. Although the Si/C (4) generates layered structures as ion channels as well during lithiation, these channels are perpendicular to the Li diffusion direction and thus are inefficient compared with the Si/C (3).

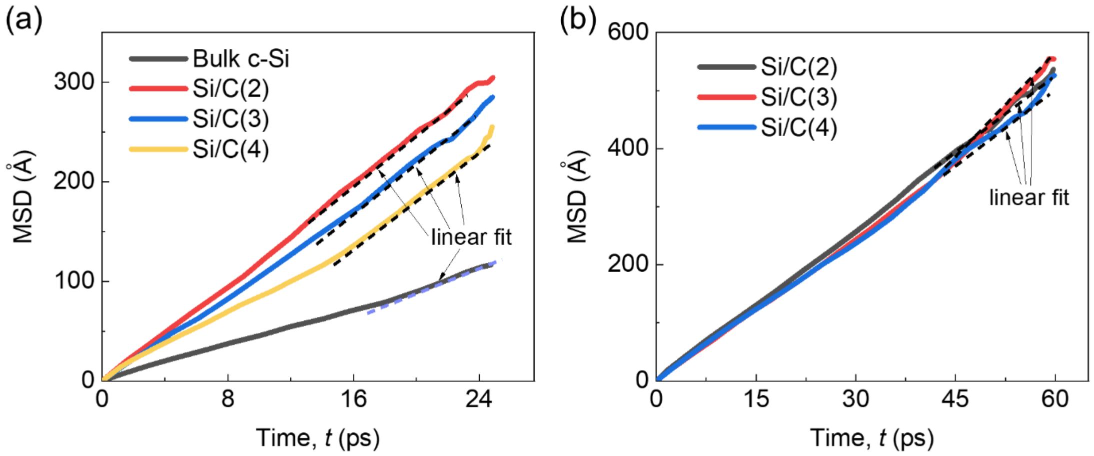

Figure 14 The MSDs for Li atoms in Si/C composite system at 1200 K for (a) pure c-Si

and mixture mode and (b) core-shell mode.

Table 1 Computed diffusion coefficients (cm^2/s) at 1200 K

Type	Bulk c-Si	Si/C (2)	Si/C (3)	Si/C (4)
Mixture mode	7.75e-5	2.097e-4	2.028e-4	2.003e-4
Core-shell mode	\	1.545e-4	1.953e-4	1.435e-4

2.4 Conclusions

DFT calculations were performed to investigate the Li diffusion behavior in Si/C composite anode materials. Two typical structures of the Si/C composite were considered in this chapter, i.e., the mixture and the core-shell modes. The AIMD results demonstrate that in the mixture mode, the Li atoms tend to diffuse in Si material first in the Si/C (4) because there is no efficient ion channel in the C layers for Li atoms to pass through fast compared with the Si/C (2) and Si/C (3), while the overall diffusion efficiencies are similar in all three structures. In the core-shell mode, Li atoms are forced to pass the C layer first, and thus, the diffuse speed is highly related to the C layer structure. The RDF results of these two modes further explain the structural evolution during the lithiation process, confirming that the initial structure of the C layer and the Si/C composite modes strongly affect the Li diffusion process. The volume expansion of different structures with various C layer thicknesses in two modes is also analyzed, and the results show that the volume expansion is smaller with a thicker C layer in both two modes, but the restriction of the C layer for Si volume expansion is ~7% more obvious in the core-shell mode. Finally, it is revealed by the MSD and diffusivity calculation that the Li diffusion properties in Si material are enhanced by the addition of C layers in both mixture mode and core-shell mode. The Li diffusivity in mixture mode shows a small dependency on C layer thickness that increasing the C layer thicknesses will slightly decrease the diffusivity. The Li diffusivity is not linearly related to C layer thickness in core-shell mode. However, for the core-shell mode, the atomic structures of the C layer significantly affect the Li diffusion properties. Results provide key insights into the fundamental mechanism of Li diffusion in Si/C composite materials and pave the road for future electrochemical system modeling in continuum scale.

CHAPTER 3 QUANTITATIVE RELATIONSHIP BETWEEN ELECTROCHEMISTRY AND MECHANICAL FAILURE

In this chapter, a sequentially coupled multiscale model considering mechanical and electrochemical fields is established and validated, which also includes a quantitative model describing the relationship between separation and electrochemical performance. Then, a comprehensive parametric study is carried out based on the calibrated model. Dominant governing factors are discussed, and the results provide insights into the high-capacity anode design.

3.1 Method and model validation

3.1.1 Model system

We focus on the anode material composed of Si/C core-shell particles (Fig. 15 (a)). The electronic paths are cut-off when the separation of Si core and C shell occurs after several cycles (Figs. 15 (a)-b), which generates the inactive particles and further leads to the capacity fade. To reveal the fundamental mechanism of this failure problem, simple geometry with two spherical core-shell particles is considered in this study (Fig. 15 (b)). Note that the irregular shapes of the particles are all simplified as a sphere, based on which a representative volume element is extracted and further represented by a two-dimensional (2D) axisymmetric model to study the separation at the particle-level (Fig. 16). The one-dimensional (1D) battery model, including an anode, cathode, and separator, is employed to study the electrochemical performance of LIB using Si/C core-shell particle anode.

These two models are coupled by transferring the Li flux computed in the 1D model into the 2D model while feeding the separation gap computed from the 2D model back into the 1D model (Fig. 15 (c)). The governing equations used in the study are introduced in the following sections.

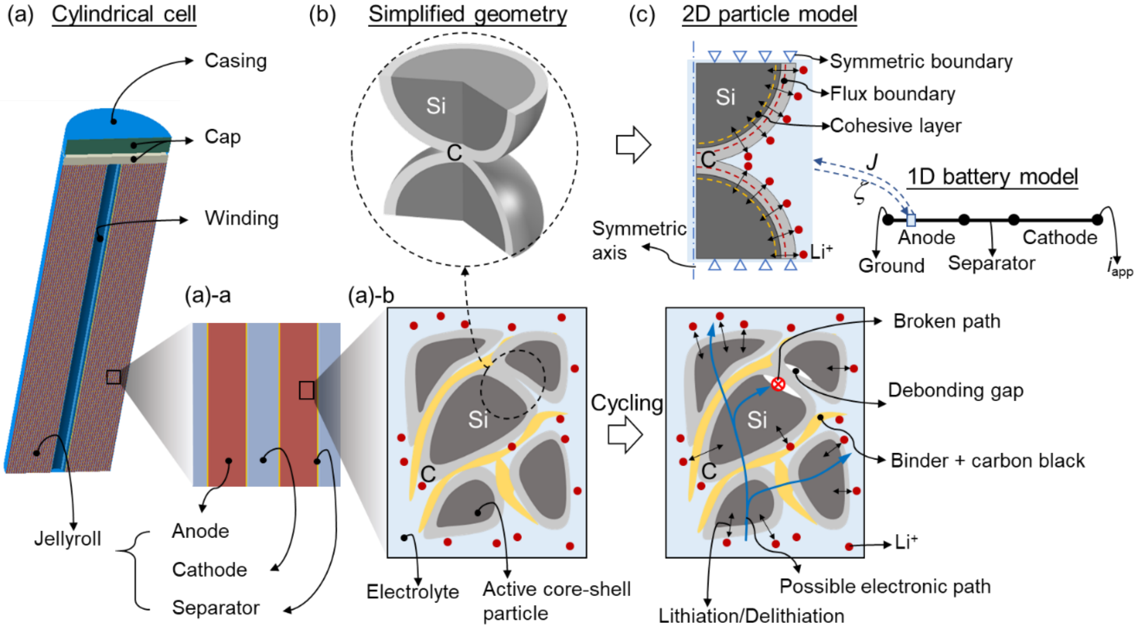

Figure 15 (a) Illustration of a typical cylindrical battery and the multiscale components: (a)-a the unit cell of jellyroll including an anode, cathode and separator; and (a)-b the composite anode structure with Si/C core-shell particles and the debonding mechanism illustration. (b) The simplified geometry model for simulation. (c) The boundary conditions for the 2D particle contact model and 1D battery model, as well as the coupling strategy between these two scales.

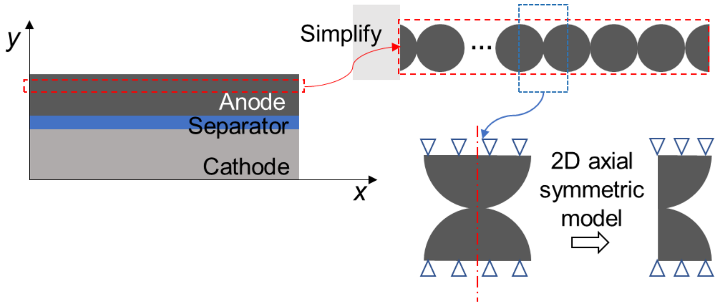

Figure 16 The assumption of particle packing geometry in the electrode and the simplification of the 2D particle model.

3.1.2 1D battery model

The current density at the surface of the active particles is given by the Butler-Volmer equation as

$$i = i_0 \left\{ \exp\left[\frac{(1-\beta)}{RT} \right] - \exp\left(-\frac{\beta F \eta}{RT} \right) \right\}, \tag{9}$$

where $i_0 = F k_c^{\alpha_a} k_a^{\alpha_c} \left(c_{s,\max} - c_{s,\mathrm{surf}} \right) \left(c_{s,\mathrm{surf}} \right)^{\alpha_c} \left(c_e / c_{e,ref} \right)^{\alpha_a}$ is the exchange current density and $\eta = \phi_s - \phi_e - E_{ref} - \phi_{SEI} - \Delta\eta$ is the overpotential with the last term $\Delta\eta = R_{\mathrm{int}} \cdot i$ related to the separation effects described in the following part. The charge conservation and mass conservation can be described as

$$\nabla \cdot \mathbf{i_e} = a_s i, \ \nabla \cdot \mathbf{i_s} = -a_s i \tag{10}$$

$$\text{and } \varepsilon_e \frac{\partial c_e}{\partial t} = -\nabla \cdot \mathbf{J_e} + \frac{a_s i}{F}, \tag{11}$$

respectively, where $a_s = 3\varepsilon_s / r_p$. The kinetics of the current density in electrolyte and solid phase can be written as

$$\mathbf{i_e} = -\kappa_e^{eff} \left[\nabla \phi_e - \frac{2RT}{F} \left(1 + \frac{d \ln f_\pm}{d \ln c_e} \right) \left(1 - t_+ \right) \nabla \ln c_e \right] \tag{12}$$

$$\mathbf{i_s} = -\kappa_s^{eff} \nabla \phi_s \, . \tag{13}$$

The Li^+ flux density in the electrolyte is given by

$$\mathbf{J_e} = -D_e^{eff} \nabla c_e + \frac{t_+}{F} \mathbf{i_e} \, . \tag{14}$$

The kinetics of the parasitic reaction of the SEI layer can be expressed as

$$i_{SEI} = -(1+HK)\frac{i_p i}{\exp(\frac{\alpha\eta_{SEI}F}{RT}) + \frac{q_{SEI} f i_p}{i}}, \tag{15}$$

where $q_{SEI} = Fc_{SEI} / A_v$ and f is a parameter based on the SEI properties.

For the boundary conditions, a ground is assumed on the surface of the anode, while a charging current, i_{app} is employed on the surface of the cathode (positive value represents charging), as shown in Fig. 15 (c).

3.1.3 2D particle model

An electro-chemo-mechanical coupled model is established for the separation study at the particle level. The Fick's second law is used in the battery model for Li^+ diffusion, which is also the governing equation for the electrochemistry at particle level for Si core and can be expressed as

$$\frac{\partial c_s}{\partial t} + \frac{1}{r^2}\frac{\partial r^2 J_s}{\partial r} = 0. \tag{16}$$

Considering the stress effects, the flux J_s can be further described as

$$J_s = A\frac{\partial c_s}{\partial r} + B\frac{\partial \sigma_h}{\partial r}, \tag{17}$$

where

$$A = \frac{D_s^{eff} F}{RT}\frac{\partial E_{ref}}{\partial c_s},\ B = \frac{D_s^{eff} F}{RT}\Omega \tag{18}$$

with the effective diffusivity $D_s^{eff} = D_0\left(\frac{c_s}{c_{s,\max}}\right)\left(c_{s,\max} - c_s\right)$. The boundary conditions and initial conditions are

$$\frac{\partial c_s}{\partial r} = 0 \text{ at } r = 0$$

$$J_s = J \text{ at } r = r_p \tag{19}$$

$$c_s(r) = c_s^0 \text{ at } t = 0 \text{ s}$$

where J is the average Li$^+$ flux at the active particle surface calculated from the 1D battery model and is applied at the surface of the Si core, as shown in Fig. 15 (c).

The hydrostatic stress σ_h in the Si core is computed from the mechanical model of which the equilibrium equation is [114]

$$\frac{\partial \sigma_{rr}(r,t)}{\partial r} + \frac{2}{r}\left[\sigma_{rr}(r,t) - \sigma_{\theta\theta}(r,t)\right] = 0. \tag{20}$$

A perfect plasticity model is considered here with yield stress $\sigma_y = \sigma_y^0 - 0.9\left(c_s / c_{s,\max}\right)$. Therefore, the total strain can be described as

$$\varepsilon = \varepsilon_{ij}^e + \varepsilon_{ij}^p + \varepsilon_{ij}^l, \tag{21}$$

where the components are deduced in the Appendix A (Eqs. (A1-A5)) [112]. For the C shell, viscoelastic material is adopted by the Maxwell model. The C shell and Si core are assumed to be in contact at the beginning, which ensures a continuous displacement at the interface until separation.

For the separation calculation, the cohesive zone model is adopted, which has been widely used in the studies of battery electrodes damage [83, 95, 115]. The onset of the separation is predicted by the quadratic failure criterion [116].

$$\left(\frac{\langle \tau_{\mathrm{I}} \rangle}{N}\right)^2 + \left(\frac{\tau_{\mathrm{II}}}{S}\right)^2 + \left(\frac{\tau_{\mathrm{III}}}{T}\right) = 1. \tag{22}$$

where τ is the element traction with the subscript I, II, and III represents separation Mode I (tensile mode), Mode II (shear mode), and Mode III (tear mode), respectively. The bracket $\langle\ \rangle$ is the Macaulay bracket defined as

$$\langle x \rangle = \begin{cases} 0, & x < 0 \\ x, & x \geq 0 \end{cases}. \tag{23}$$

The total mixed-mode relative displacement u_m is defined as

$$u_m = \sqrt{\langle u_{\mathrm{I}} \rangle^2 + u_{\mathrm{II}}^2}\ . \tag{24}$$

The Benzeggagh-Kenane (B-K) criterion is used for separation propagation in this study, from which the total critical energy release rate is [117]

$$G^c = G_{\mathrm{I}}^c + \left(G_{\mathrm{II}}^c - G_{\mathrm{I}}^c\right)\left(\frac{G_{\mathrm{II}}}{G_{\mathrm{I}} + G_{\mathrm{II}}}\right)^{\alpha}. \tag{25}$$

From this model, the separation of Si core and C shell can be obtained, based on which the interfacial resistance used in 1D battery model can be written out as [5]

$$R_{\mathrm{int}} = R_{\mathrm{int}}^{\mathrm{ref}}\,(e^{\zeta/\zeta_{\mathrm{ref}}} - 1)\,, \tag{26}$$

where the gap ζ is transferred to the 1D battery model and influences the overpotential (Eq. (9)), as shown in Fig. 15 (c).

3.1.4 Coupling strategy

The Li^+ flux, J can be transported from the 1D battery model to the diffusion model of the 2D particle model, and conversely, the gap ζ is transferred from the mechanical model of 2D particle model to the 1D battery model, by which the multiscale model is achieved (Fig. 17). For the 2D particle model, the electro-chemo-mechanical model is coupled by translating the Li^+ concentration, c_s from the diffusion model to the mechanical model, and transporting the hydrostatic stress, σ_h from the mechanical model back to the diffusion model.

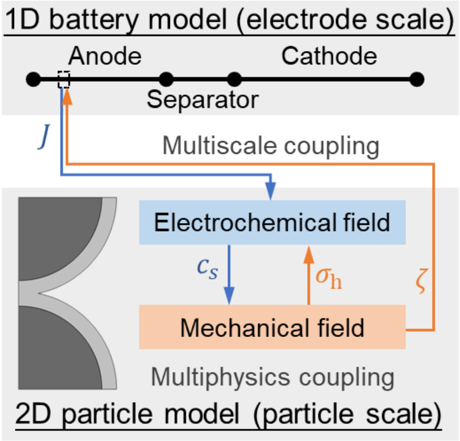

Figure 17 Schematic of the coupling strategy

3.1.5 Numerical simulation

The coupled model developed in the above sections will be implemented into the finite element (FE) simulation platform, COMSOL Multiphysics. The 1D battery model is directly used from the module library with Si anode, LCO cathode, and LiPF6-based electrolyte. The open-circuit potential (OCP) curves of electrodes are used for the equilibrium potential, E_{ref} (Fig. 18 (a)). The Li^+ flux calculated in this model is transferred into the 2D model and applied on the surface of the Si core. The 2D particle model is achieved by the solid mechanics module and the PDE module for the simulation of mechanical behavior and diffusion behavior, respectively. Only the Li^+ diffusion in Si core is considered [73], while the C shell only behaves mechanically as a linear elastic material. A contact method with the cohesive zone is employed at the interface of Si and C to achieve the separation behavior. The adhesion and de-cohesion interfaces under the contact setting are used. The side surface of the C shell is free. The symmetric boundary condition is applied on the top and bottom of the two contact particles (Fig. 15 (c)). The parameters used in the model are summarized in Table 2.

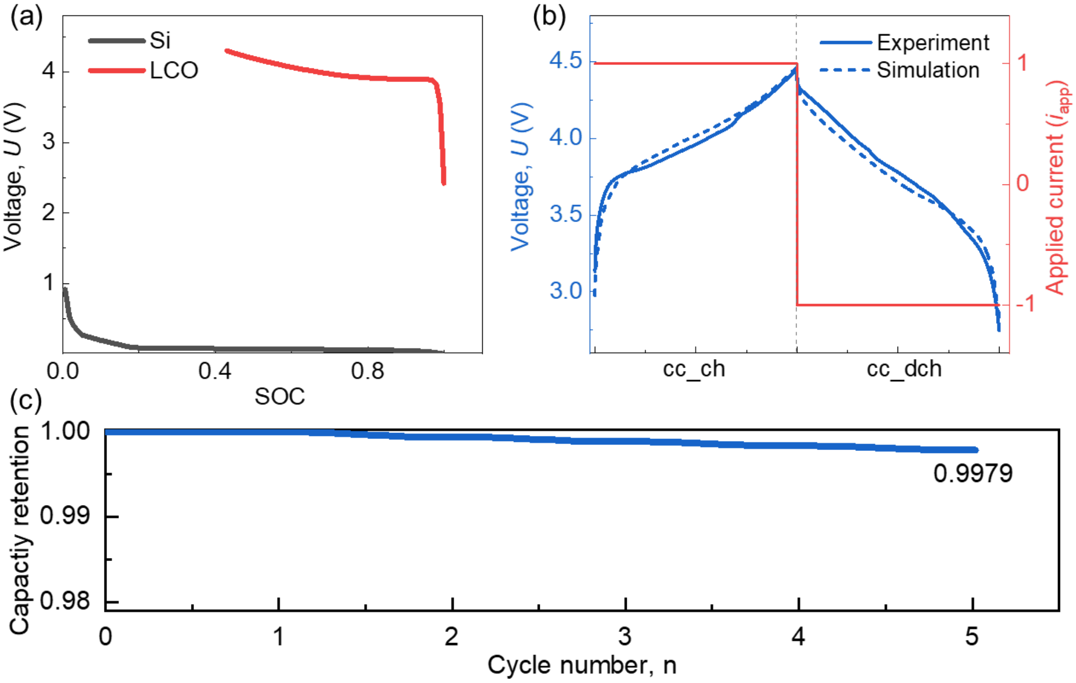

Figure 18 (a) The open-circuit potential of the anode and cathode material used in the simulation; (b) The profile of applied current, and voltage comparison between simulation result and experiment data in one cycle; (c) The capacity retention considering SEI effects only after five cycles.

Table 2 Summarization of input parameters in the model

Parameter	Symbol	Value
1D battery model		
Anode thickness	H_{anode}	100 μm (estimated)
Cathode thickness	H_{cathode}	183 μm (estimated)
Separator thickness	$H_{\text{separator}}$	52 μm (estimated)
Volume fraction of solid in the anode	ε_s^a	0.471 (estimated)
Volume fraction of electrolyte in the anode	ε_e^a	0.503 (estimated)

Volume fraction of solid in the cathode	ε_s^c	0.297 (estimated)
Volume fraction of electrolyte in the cathode	ε_e^c	0.63 (estimated)
Electrical conductivity of cathode [118]	$\kappa_s^{cathode}$	100 S/m
Electrical conductivity of anode [119]	κ_s^{anode}	1 S/m
Initial Li-ion concentration in electrolyte [120]	C_e^0	1000 mol/m^3
Diffusion coefficient in electrolyte [51]	D_e	7.5×10^{-11} m^2/s
Transference number [120]	t_+	0.363
Transfer coefficient	α_a α_c	0.5
Reference interfacial resistance	$R_{\mathrm{int}}^{\mathrm{ref}}$	2×10^{-3} $\Omega\cdot\mathrm{m}^2$ (estimated)
2D particle model		
Partial molar volume of Si [121]	Ω	9×10^{-6} m^3/mol
Modulus of Si [122]	E_{Si}	$E_{Si}(c_s)=150-100c_s/c_{s,\max}$ GPa
Maximum Li concentration in Si [119]	$c_{s,\max}$	278000 mol/m^3
Diffusion coefficient in Si [121]	D_0	1.67×10^{-14} m^2/s
Radius of Si core	r_p	85 nm (estimated)
Reference gap	ζ_{ref}	0.25 nm (estimated)
Critical normal strength [73]	N	1 GPa
Critical shear strength [73]	S	1.2 Gpa
Critical tensile energy release rate	G_{I}^c	2 J/m^2 (estimated)
Critical shear energy release rate	G_{II}^c	5 J/m^2 (estimated)
Mode mixity exponent	α	2.28

3.1.6 Model validation

A 0.5C charging/discharging test was simulated using the model developed without consideration of SEI formation and separation gap effect for one cycle. It is revealed that the model can well capture the experimental results with the same loading condition (Fig. 18 (b)) in terms of the voltage profile. Then, the cycling loading at a rate of 0.5 C for five cycles is applied to the model considering the SEI formation and gap effect, respectively. The capacity retention in this study is calculated by the following equation

$$C_r^n = t_{dch}^n / t_{dch}^1 . \tag{27}$$

The capacity fade after five cycles caused by the SEI formation is about 0.2% which is negligible compared to the gap effects (1.56%) (Fig. 18 (c)). Besides, the effect of SEI formation is very similar among various cases when the radius of the Si core keeps unchanged. Thus, in the following parametric studies, only the gap effect is considered and discussed using the validated model for five cycles. For the parametric study, the charging rate C, core/shell ratio $r_{c/s}=R_{Si}/t_c$, shell modulus E_c, and shell viscosity μ are considered, among which the one with 1C (40 A applied current) rate, $r_{c/s}$=5.67, E_c=40 GPa, and μ =4e5 GPa·s is regarded as the baseline. The detailed parametric study is summarized in Table 3. Note that only one parameter is varied at one time.

Table 3 Parameters used for parametric study

Parameter	Symbol	Value
Charging rate	C	0.75 C, 1 C, 1.25 C
Core/shell ratio	$r_{c/s}$	5.67, 4.47, 3.09
C shell modulus	E_c	40 GPa, 64 GPa, 85 GPa
C shell viscosity	μ	4e5 GPa·s, 6.4e5 GPa·s, 8e5 GPa·s,

3.2 Mechanical behavior

We can see the contact stress at the Si/C interface increases nonlinearly in the charging process due to the expansion and the plastic deformation of the Si core (Fig. 19 (a)). At the end of the charging process (point *a*), the contact stress reaches its peak value, and the corresponding stress distribution at this point indicates the plastic deformation zone in Si core because the Mises stress in that area reaches the yield strength (Fig. 19 (b)). When the discharging process begins, the contact stress starts to decrease until zero where the separation occurs at point *b,* leading to the smaller stresses within Si core near the contact surface (point *c*). At point *b*, the initiation criterion is satisfied, thus triggering the gap propagation. The gap increases very slow at the beginning and then sharply rises until the ultimate value (point *c*), which contributes to the interfacial resistance in the battery model. Note that the negative value of the gap (Fig.19 (a)) in the charging process and the early discharging process is caused by the penalty contact method used in this model, which allows a small penetration during the modeling. When calculating the interfacial resistance R_{int} (Eq. (26)), the negative ζ is regarded as zero.

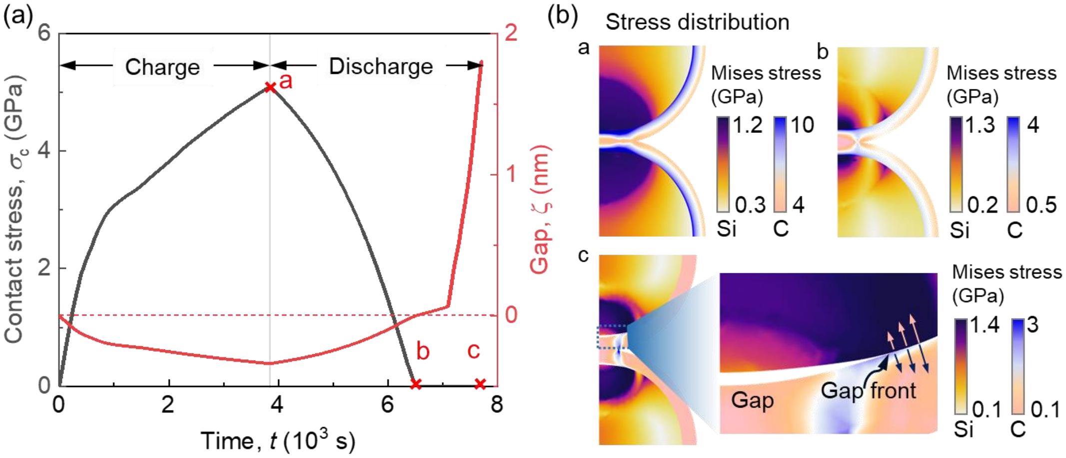

Figure 19 (a) evolution profile of contact stress and the gap at the Si/C interface under contact area; (b) Mises stress distribution and deformed shape at the specific time indicated in (a).

3.3 Electrochemical behavior

The major difference between the voltages calculated from models with gap effects and without gap effects shows at the end of the discharging process (Fig. 20 (a)). The model with gap effects shows a shorter discharging period and a smaller voltage at the end of the discharging process, which reveals that the separation gap can cause the capacity fade. Fig. 20 (b) shows the nonuniform distribution of Li^+ concentration in the Si core which is caused by the nonuniformly distributed stress indicated in Fig. 19 (b). It has been demonstrated that the tensile stress attracts the Li^+ [73]; hence the Li^+ concentration at the contact zone is smaller than that far from the contact area before the gap occurs (point *a*-*c*). After the separation happens, the smaller stress generated near the contact surface astricts the Li^+ diffusion, which causes the larger Li^+ concentration at that zone (point *d*) and thus reduces the output capacity.

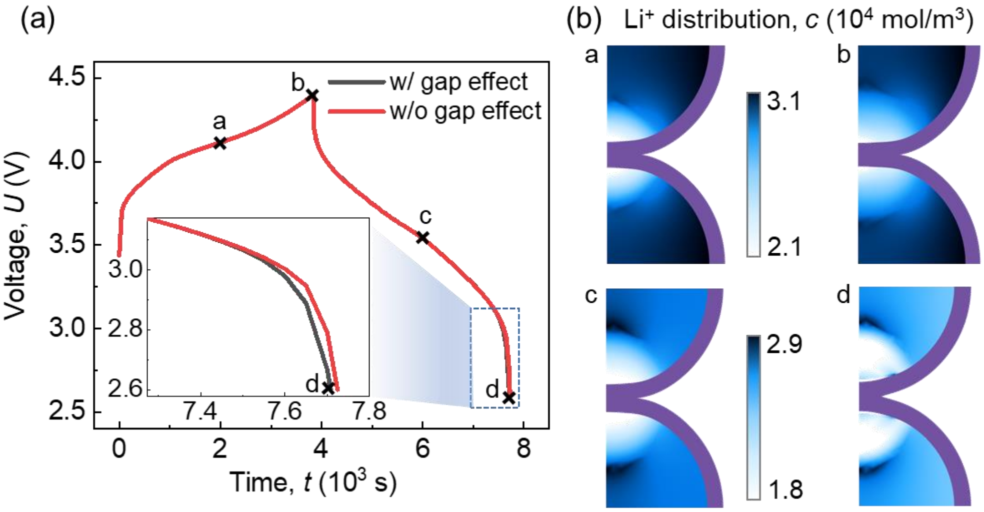

Figure 20 (a) Voltage profile of the simulation results with and without gap effect consideration; (b) Li^+ concentration distribution in Si core at the specific time indicated in (a). Note that the Li^+ concentration in C shell is always zero since the diffusion in C shell is not considered.

3.4 Mechanical stress and Li^+ concentration analysis

The mechanical stress and Li^+ concentration of particles at various charging rates are discussed here as the representative (Figs. 21 and 22), while the other cases for various shell thickness, shell modulus, and shell viscosity are not shown here due to the page limit.

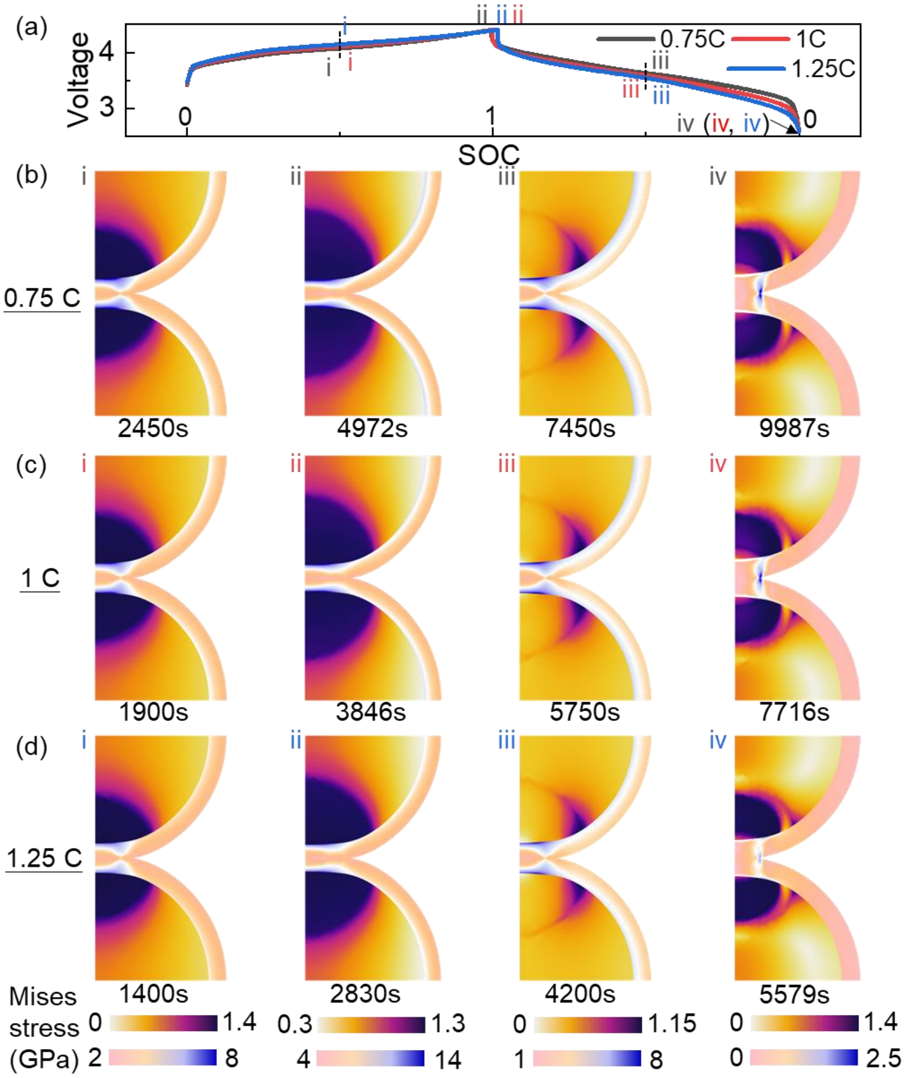

Figure 21 (a) The voltage profile for various charging rates. Four specific time points (point i in the charging process, and points ii, iii, and iv in the discharging process) are selected to analyze the corresponding stress distribution within the particles for (b) 0.75C rate, (d) 1C rate, and (d) 1.25C rate, respectively. Note that the same column shares the same legend bar at the bottom for figures (b)-(d).

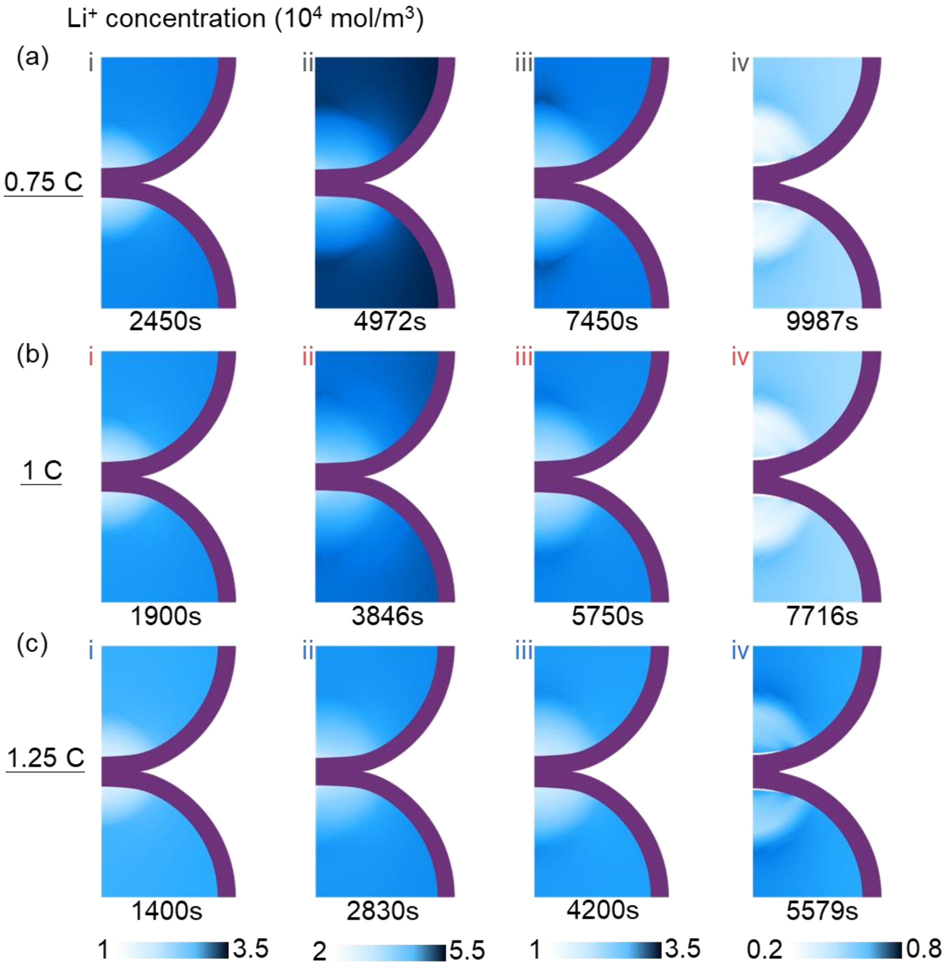

Figure 22 The Li$^+$ concentration distribution within the particles at the same time points in Fig. 7(a) (point i in the charging process, and points ii, iii, and iv in the discharging process) for (a) 0.75C rate, (b) 1C rate, and (c) 1.25C rate, respectively. Note that the same column shares the same legend bar at the bottom.

A similar stress distribution tendency is found for all three charging rates (Fig. 21 (b)-(d)). The difference among various rates is that a lower rate generates larger stress and plastic deformation zone during charging, which is attributed to the larger Li$^+$ concentration in the particle at a low charging rate (Fig. 22). In the discharging process, the largest stress zone is found at the beginning (point ii in Fig. 21(b)-(d)), which starts to decrease due to the loss of particle contact (point iii in Fig. 21(b)-(d)) mitigating the compressive stress.

Near the end of the discharging, the stress at the contact area increases again because the contraction of the Si core generates tensile stress at the interface which further increases the stress magnitude within the Si core (Point iv in Fig. 21(b)-(d)). At the end of the discharging, the stress shows a small value at the interface where the gap generates because the generation of the gap releases the tensile interaction. This small value is more obvious at the lower charging rate, which indicates a larger gap.

As Fig. 22 shows, The Li^+ concentration within Si core is larger at a lower charging rate (point i in Fig. 22(a)-(c)) in the charging process as mentioned above, because the mass transport rate is much smaller than the charge transport rate of which the effect is more obvious at larger charging rates. Thus, when the charging rate is large, the voltage reaches the setting value first before the Li^+ diffusion balanced. This larger concentration in the charging process leads to a larger deformation of Si core and thus larger stress. However, the Li^+ concentration gradient is more obvious at a lower charging rate due to the larger stress formed at the contact area (point ii in Fig. 22 (a)-(c)). In the discharging process, the Li^+ concentration at a lower charging rate is larger at the beginning (point iii in Fig. 22 (a)-(c)) due to the larger initial concentration value. Near the end of the discharging, the charging rate effect is indicated that the voltage decreases to the setting value before Li^+ can be extracted from the Si core at a higher charging rate, which finally leads to a larger residual Li^+ concentration value (point iv in Fig. 22 (a)-(c)).

3.5 Separation gap evolution

As discussed in the *Results* section, the separation gap at the Si/C interface takes the major responsibility for the mechanical degradation and capacity fade of such high-capacity battery using Si/C core-shell particle anodes. Thus, it is necessary to analyze the separation behavior among various configurations of the Si/C core-shell particles with the parameters summarized in Table 3, which may provide insights into the core-shell particle design to prolong the cycle life.

The separation gap mainly occurs at the end of each cycle and the beginning of the next cycle, lasting for about 30 minutes. This is because the separation is caused by the shrinkage of Si core in the discharging process, and the gap disappears gradually due to the re-contact of Si core and C shell in the charging process of the next cycle caused by the Si core expansion. For all the cases, a similar tendency is revealed that the gap increases along with the cycle number and keeps stable after several cycles (Fig. 23). This is because most of the irreversible deformation of Si core is generated in the first cycle, then the rest of the Si core materials not reaching the yield stress in the first cycle gradually enters the plastic stage in the following cycles, which causes the slow increase of the gap thickness.

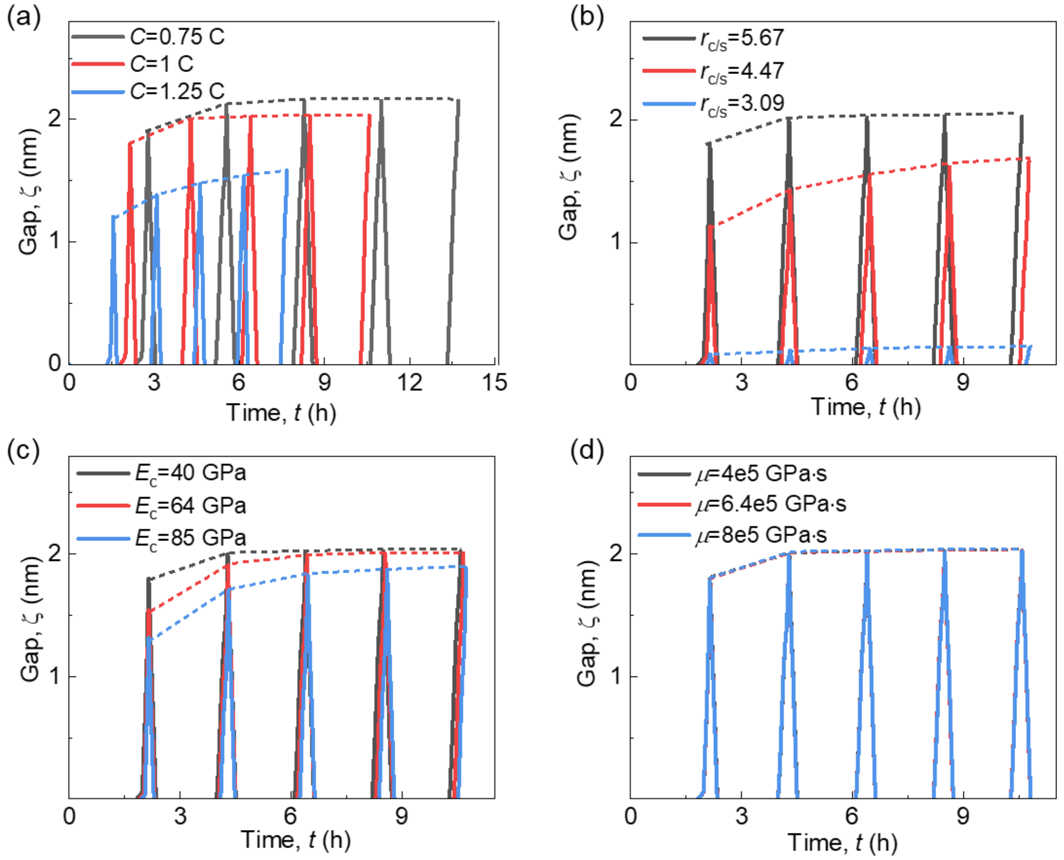

Figure 23 The gap evolution during 5 cycles with various (a) charging rates; (b) shell thickness; (c) shell modulus and (d) shell viscosity. The dash lines represent the changing tendency of the maximum values.

The separation is less likely to occur as the charging rate, *C* increases (Fig. 23 (a)), because the larger C-rate usually leads to a smaller amount of Li^+ diffusion in the charging process and further causes the smaller volume expansion of Si core. This smaller volume expansion alleviates the stress generation at the Si/C interface which finally leads to the smaller separation gap. The gap is smaller for particles with a smaller core/shell ratio $r_{c/s}$ (Fig. 23 (b)) mainly due to two responsible reasons: (1) a thick shell can limit the Si core expansion and reduce the gap, and (2) the thick shell would generate low energy release rate *G* and makes it less likely to exceed the critical value for separation. It indicates that particle with larger shell modulus, E_c has a smaller gap because the shell with large modulus plays a similar role as the thick shell (Fig. 23 (c)). Fig. 23 (d) shows that the viscosity, μ of the shell, has little effect on the separation.

3.6 Capacity retention analysis

The mechanical gap exponentially influences the interfacial resistance, as Eq. (26) shows. The evolution of interfacial resistance shows a similar trend to the separation gap with the magnitude of 0-10 $\Omega \cdot m^2$ (Fig. 24 (a)-(d)). To show the influence of this interfacial resistance, it is compared with the internal resistance of the battery in this study calculated as [123]

$$R_{in} = \frac{E_{OCV} - E_{cell}}{i_{app}}, \tag{28}$$

where E_{OCV} is the open-circuit voltage, and E_{cell} is the cell voltage. Only the internal resistances for various charging rates are shown in Fig. 24 (e), because the other cases share the same charging rates (1C) at which the internal resistance is almost the same. The internal resistance is much smaller than the interfacial resistance in terms of the magnitude. Nevertheless, internal resistance is a nominal value for the electrode and exists during the whole cycling process, while the interfacial resistance is a local value existing at the particle surface and only occurs in a short time window (from the end of the charging to the beginning of the discharging). Hence, the effect of the interfacial resistance is not tremendous but not neglectable.

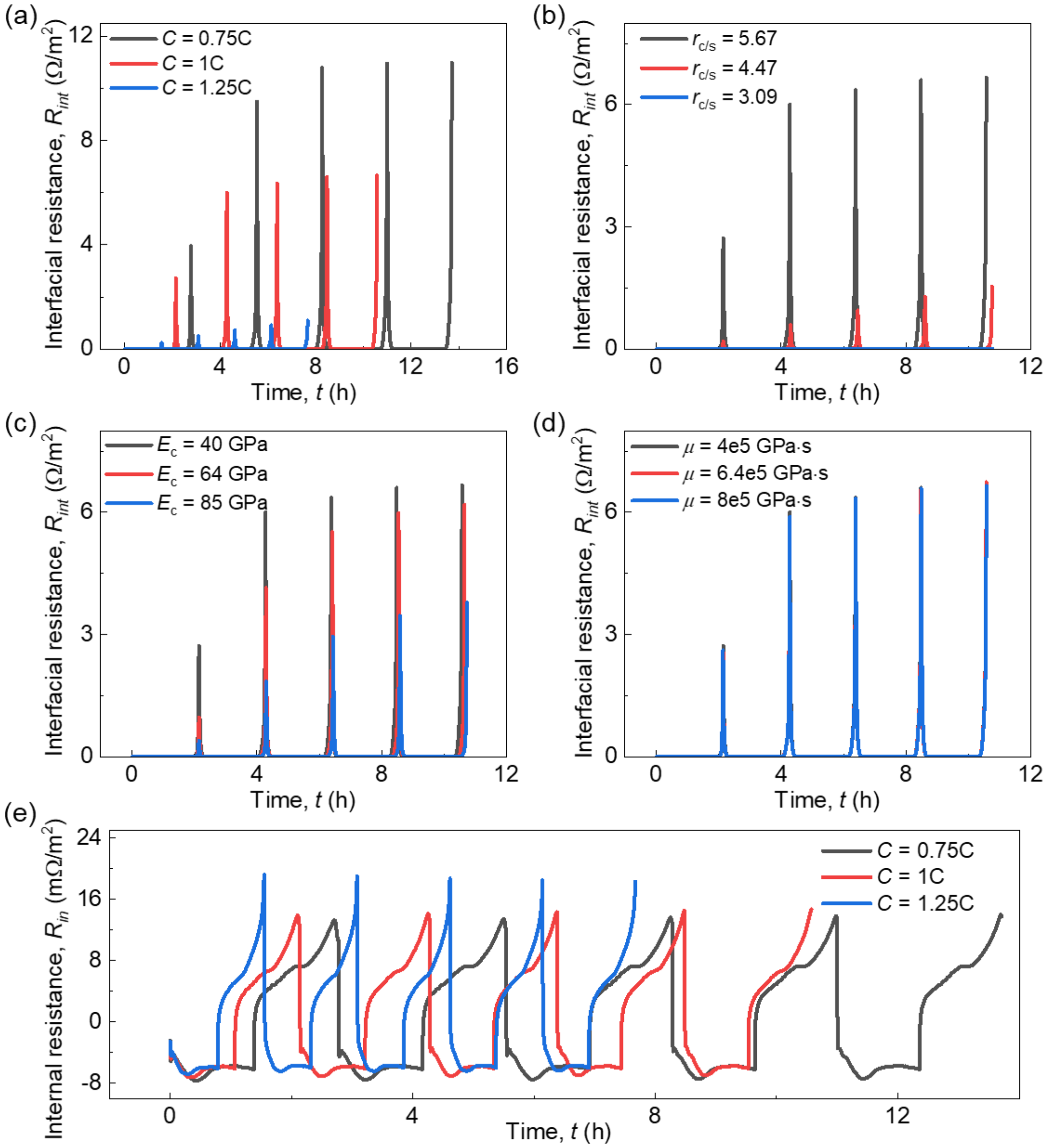

Figure 24 The interfacial resistance evolution during 5 cycles with various (a) charging rates; (b) shell thickness; (c) shell modulus and (d) shell viscosity, and the internal resistance evolution during 5 cycles for various charging rates.

The separation gap finally influences the electrochemical performance of the battery by reducing the capacity. Hence, capacity retention defined in Eq. (27) is used to analyze this effect among particles with different parameters. Here, the first cycle is considered as the initialization process, so the capacity retention is calculated based on the second cycle.

The overall trend is that the minimum capacity retention after 4 cycles is about 0.984 for all four parameters.

One may see that the capacity retention keeps almost unchanged when C increases from 0.75 C to 1 C, but then it increases at 1.25 C rate (Fig. 25 (a)). According to the equation of $\Delta\eta$, the potential loss is not only related to the R_{int} caused by the gap but also the local current density, i related to the charging rate C. The larger C can guarantee a smaller gap, but on the contrary, the i is larger with a larger C. However, the gap effect is dominant since the R_{int} is exponentially related to the gap. Therefore, in general, higher charging rates are beneficial for cycle life in terms of separation effects.

For the other three parameters, the charging rate is the same as 1C. Therefore, the capacity retention is mainly related to the separation gap that a smaller gap can ensure larger capacity retention. For the core/shell ratio, the battery using Si/C core-shell particles with $r_{\text{c/s}}$ smaller than 4.47 shows a very tiny capacity fade after four cycles (Fig. 25 (b)). The particles with E_{c} larger than 85 GPa can guarantee capacity retention larger than 0.995 after four cycles for the battery (Fig. 25 (c)), while the viscosity of the shell has no effect on the capacity performance (Fig. 25 (d)).

In summary, higher charging rates and battery using anode composed of core-shell particles with a thicker and stiffer shell can mitigate the electro-chemo-mechanical degradation caused by the separation.

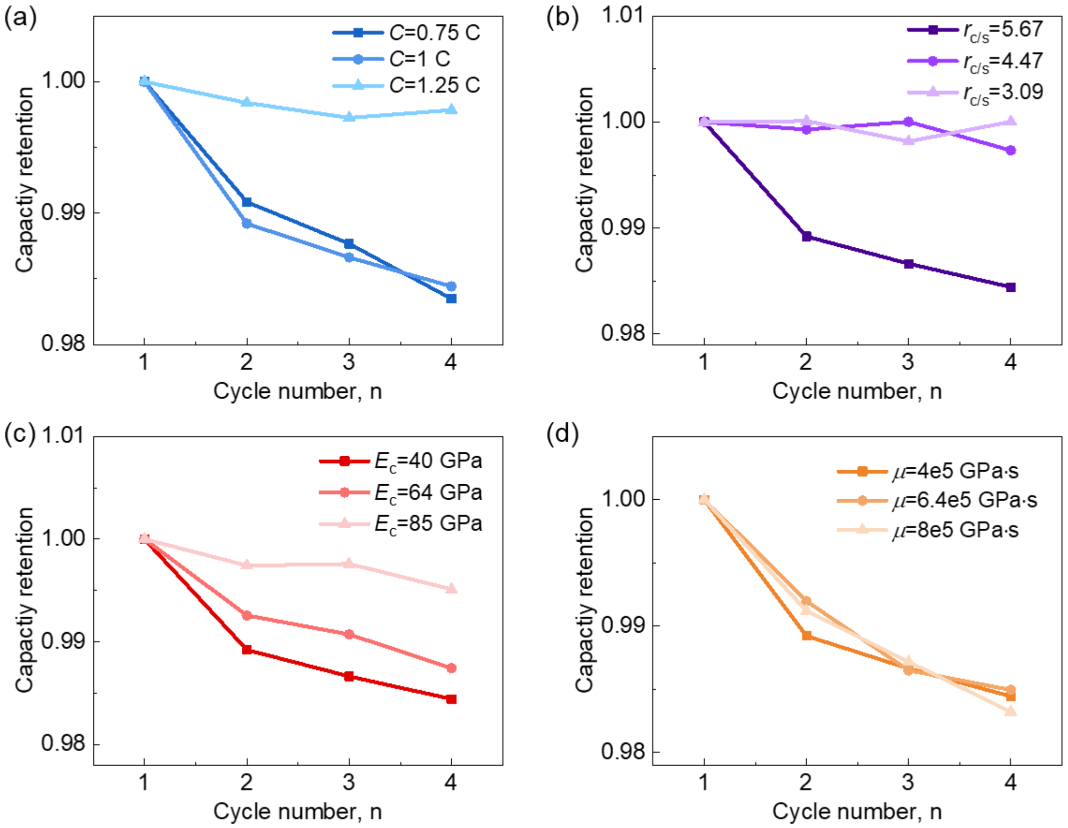

Figure 25 The capacity retention after 5 cycles with various (a) charging rates; (b) shell thickness; (c) shell modulus and (d) shell viscosity.

3.7 Conclusions

In this chapter, the electro-chemo-mechanical degradation of LIB with Si/C core-shell anode material was studied through simulation. A sequentially coupled multiscale model consisting 1D battery model and 2D particle model was established. For the 2D particle model, the diffusion model, the mechanical model, and the cohesive element model were coupled. This fully coupled model was validated by the voltage profile from the charging/discharging test and was then used for the parametric study. Four parameters were considered in this study, i.e., charging rate, core/shell ratio, shell modulus, and shell viscosity, and their effects on electro-chemo-mechanical degradation of LIB were analyzed.

The results show that larger charging rates, smaller core/shell ratio, and larger shell modulus can lead to the smaller separation gap, which mitigates the capacity fade, while the shell viscosity does not influence the gap formation and capacity retention. This study provides an efficient model for separation study about Si/C core-shell particles, as well as assists the engineering design of high-capacity anode and safe operation of LIB to prolong the cycle life.

CHAPTER 4 MULTIPHYSICS MODELING OF PARTICLES DURING LITHIATION/DELITHIATION PROCESS

In this chapter, we firstly construct a multiphysics computational model to mimic the lithiation/delithiation of two Si/C core-shell particles in contact. Meanwhile, we establish a theoretical model to understand the fundamental mechanism in the contact particles. We consider the strain rate effect in the above-mentioned computational model and analyze the rate-dependent behavior of contact Si/C core-shell particles. Besides, we introduce different shell properties, i.e. shell modulus and shell thickness, into the computational model to predict the coupling effects of these two factors on the charging rates. We demonstrate that the theoretical model can well predict the stress and deformation of contact core-shell particles which shows a good consistence with simulation results. Finally, we propose a design guideline about core-shell structure configuration based on the analysis

Further, to fundamentally understand the structure-properties relations of Si/C composite structures, we establish two-dimensional (2D) multiphysics models based on the electro-chemo-mechanical coupling strategy developed above for five representative Si/C nanostructures achievable in lab fabrication: core-shell structure,[29, 111, 124] yolk-shell structure,[31-32, 125] dual-shell structure,[35-36, 126] hollow core-shell structure,[39, 127] multicore-shell structure[128-129]. This study provides guidance on battery anode nanostructure design towards high energy density performance.

4.1 Modeling of contact stress among Si/C core-shell particles

4.1.1 Materials and methods

4.1.1.1 Material and model abstract

The multiscale structure of Si/C composite anode was characterized by SEM (scanning electron microscope) (see Figs. 26(a)-(c)). The particle shown in Fig. 26(a) is a Si-C composite particle of which the detailed configuration is shown in Fig. 26(c). The composite anode (Fig. 26(b)) was composed by Si-C composite particles and graphite particles, which is ready for production with a 28.5% increase of capacity and an 8% volume change increasing compared to traditional graphite anodes. The addition of Si makes the particle capacity higher than pure graphite particle while the volume change during charging/discharging process is greatly relieved compared with the pure Si particle. Fig. 26(c) depicts a Si nanoparticle wrapped with a C layer to form a Si/C core-shell particle.

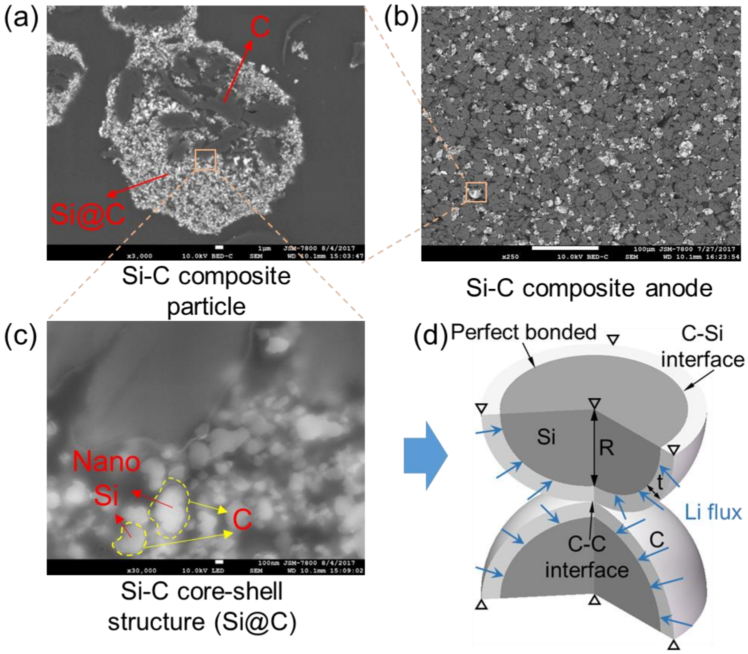

Figure 26 SEM images of materials and the extracted model. (a) composite particle

composed of Si/C core-shell particles and carbon particles (diameter is 20~30 um); (b) composite anode composed of particle shown in (a) and graphite; (c) Si/C core-shell structure (diameter of nano Si particle is around 100 nm). (d) Axisymmetric finite element model for two contact Si/C core-shell particles. R and t are the radius of Si and thickness of carbon shell, respectively. Blue arrows and hollow triangles indicate the constant Li flux and vertical constraint, respectively

In this study, the inelastic mechanical behavior of this Si/C core-shell particle during charging/discharging cycling were calculated based on COMSOL platform. More importantly, the strain rate-dependent properties were analyzed by incorporating it into the modeling process. Two sphere Si nanoparticles with radius R ranging from 50~54 nm, wrapped with a C layer with the thickness t ranging from 6~10 nm, are considered in the simulation (see Fig. 26(d)). Fig. 26(d) also illustrates the electrochemical and mechanical boundary conditions of the axisymmetric finite element model. The diffusion of Li-ion influenced by the stress distribution within the Si particles is trivial [72, 76, 130], thus this coupling effect is not considered in the present study as the shape change, and stress evolution may have low dependence on this coupling. As such, the diffusion of Li-ion is assumed to be mainly driven by the gradient of Li-ion concentration with a constant Li-ion diffusivity $D = 10^{-16}$ m^2/s [48]. Generally, when the battery cell is charged/discharged under a constant voltage or current, the current (or flux) on every point of the particle surface within the composite electrode may not be constant. However, it is assumed that the current (or flux) on the surface of particles is constant to simplify the problem. In this study, the Li-ion diffusion in C shell is not considered since the main shape changes are caused by Si. Si would change from crystalline to amorphous phase during the first cycling and keep in amorphous phase in the following cycles [131]. To avoid the effects of this phase change, we mainly considered the amorphous Si in the present study.

4.1.1.2 Governing equations for the computational model

The total strain of Si core during lithiation can be expressed by Eq. (21). And it is assumed to obey the J_2 flow rule that the plastic yielding occurs when the von Mises stress reaches the yield stress of Si. The yield stress of Si is related to the Li-ion concentration (Eq. (A5)). Furthermore, to describe the strain rate-dependent behavior of Si/C core-shell structure, a typical viscoplastic power-law is applied. From this power law function, the plastic stress related to the strain rate can expressed as

$$\sigma = \sigma_y \left(\dot{\varepsilon}_p / A \right)^{1/m} + \sigma_y \, . \tag{29}$$

Since the shape change of C shell during lithiation is trivial compared to that of Si and it has little effect on the mechanical behavior of Si, only elasticity of C shell was considered in this work without Li-ion diffusion. The Young's modulus of C shell, E_c, is set in range as 20~100 GPa with a varied thickness, *t*, ranging from 6~10 nm. This is constructed to see the influence of shell properties.

To simulate the mechanical behavior of Si-C core-shell particles, a constant current (or flux) is imposed on the surface of Si nanoparticles, of which the magnitude can be written as following

$$\left| \bar{J}_0 \right| = \frac{V}{S} c_{\mathrm{s,max}} C / [3600\,\mathrm{s}], \tag{30}$$

where the charging/discharging rate, *C*, is the theoretical inverse time in hours to complete the charging/discharging process. To study the strain rate (i.e. charging rate) dependent behavior, five different charging rates (0.5C, 2C, 5C, 8C, 10C) are applied.

4.1.2 Theoretical model development

4.1.2.1 Single core-shell particle with large deformation

Since the experiment measurement on stress evolution within nanoparticles is very difficult to conduct, theoretical analysis is an important method to reveal the fundamental mechanism. Although theoretical models for single particles about lithiation-induced swelling were established in previous literature, a complete model describing two contact core-shell particles is still lacking. Developing such a comprehensive model could not only enrich theoretical framework but understand the mechanism in mechanical behavior during electrochemical cycling.

A theoretical model for single core-shell particle with large deformation was established, as the following equations shows:

In Si core ($0 \le r \le a$):

$$\begin{aligned} \sigma_{rr,1} &= \sigma_{rr}^{cs} + \frac{2\Omega_1 E_1}{3(1-\upsilon_1)}\left(\frac{1}{a^3}\int_0^a cr^2\mathrm{d}r - \frac{1}{r^3}\int_0^r cr^2\mathrm{d}r\right) \\ \sigma_{\theta\theta,1} &= \sigma_{rr}^{cs} + \frac{\Omega_1 E_1}{3(1-\upsilon_1)}\left(\frac{2}{a^3}\int_0^a cr^2\mathrm{d}r + \frac{1}{r^3}\int_0^r cr^2\mathrm{d}r - c\right) \end{aligned} \tag{31}$$

$$u_1 = \frac{r(1-2\upsilon_1)\sigma_{rr}^{cs}}{E_1} + \frac{r\Omega_1}{3}\left[\frac{2(1-2\upsilon_1)}{1-\upsilon_1}\frac{1}{a^3}\int_0^a cr^2\mathrm{d}r + \frac{1+\upsilon_1}{1-\upsilon_1}\frac{1}{r^3}\int_0^r cr^2\mathrm{d}r\right] \tag{32}$$

In C shell ($a \le r \le b$):

$$\begin{aligned}\sigma_{rr,2} &= \frac{a^3}{b^3-a^3}\left[(\frac{b}{r})^3-1\right]\sigma_{rr}^{cs} \\ \sigma_{\theta\theta,2} &= -\frac{a^3}{b^3-a^3}\left[1+\frac{1}{2}(\frac{b}{r})^3\right]\sigma_{rr}^{cs}\end{aligned} \tag{33}$$

$$u_2 = -\frac{ra^3}{(b^3-a^3)E_2}\left[(1-2\upsilon_2)+\frac{1}{2}(\frac{b}{r})^3(1+\upsilon_2)\right]\sigma_{rr}^{cs} \tag{34}$$

where σ_{rr}^{cs} is the normal stress at Si/C interface (see Eq. (B1)).

4.1.2.2 Two contact core-shell particles

When discussing the stress in two contact core-shell particles, an elastic-plastic contact model is built. This model can be expressed by the following equations which are based on the theoretical model of single core-shell particle, as described in Table 4:

Table 4 Theoretical model components for two contact core-shell particles

Stress at core-shell particle surface	Stress at Si-C interface	Deformation
$\sigma_c = \frac{2wE^*}{\pi R^*}$	$\sigma_n = -\sigma_c(1+z^2/a^2)^{-1}$	$0 \le \delta \le \delta_y$
Computed by cubic Hermite polynomials		$\delta_y \le \delta \le \delta_p$
$\sigma_c = -\sigma_n(1+z^2/a^2)$	$\sigma_n = \beta\sigma_y + \sigma_{rr}^{cs}$	$\delta \ge \delta_p$
All the parameters used in the above models are explained in Appendix B		

This elastic-plastic contact model of two core-shell particles is compared with the simulation results based on the computation method described in the following sections, as shown in Fig. 27. The result shows good consistency, which means this contact model can be used to predict core-shell particle contact behaviors and help to reveal the mechanism of stress evolution during the fast charging rate simulation works.

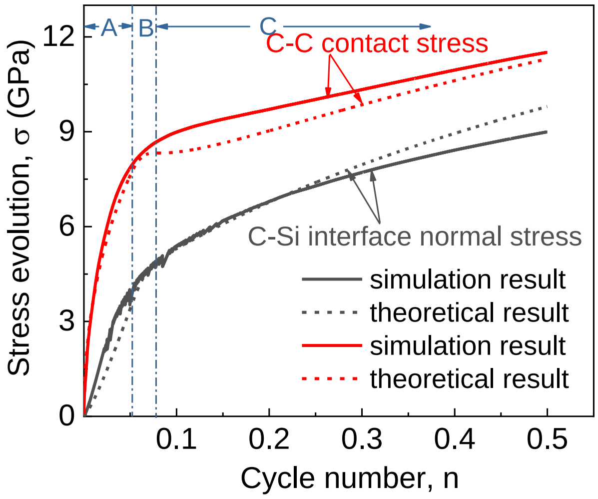

Figure 27 Comparison between simulation results and theoretical model. The stress evolution at Si-C interface and C-C contact area of two contact core-shell particles during the first charging process both deduced from the theoretical model and extract from simulation results, are compared.

4.1.3 Computational model validation

The rate factors are not considered in the theoretical models. To investigate the rate effects on this core-shell particle, computational method was selected to illustrate the rate-dependent behavior. Before investigating rate-dependent mechanical behaviors, the Si nanoparticle model is first validated, as shown in Fig. 28. No available experimental technique is available to accurately measure the stress distribution in nanoparticles currently, so the model in this work was validated by comparing the results with the model proposed in literature which had been demonstrated to be effective by the authors [132]. This proposed model in literature was realized in ABAQUS platform. All the parameters used in the model in this work, i.e., the geometrical, mechanical and diffusion-related parameters, are consistent with that in that model from the literature. However, we consider the problem from a fundamental way where Li^+ diffusion is carefully described and expressed in the electrochemical governing equations. Comparisons shown in Fig. 28 indicate the feasibility of this model, and it will be used in the following rate-dependent analysis.

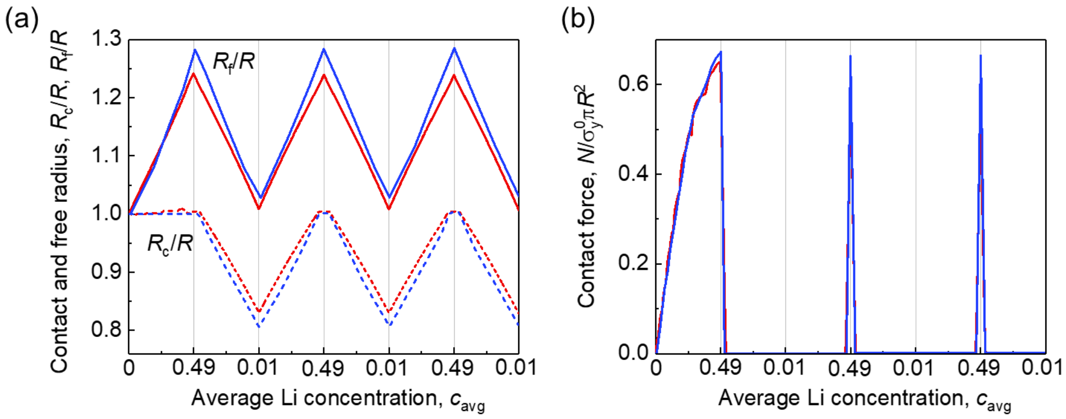

Figure 28 Model validation by comparing results in the present model with results of model in literature. Figures show the comparison on (a) Si radius evolution; (b) normalized contact force (N is the contact force, σ_y^0 is the initial yield stress and R is the initial radius of Si) Note: blue lines and red lines represent results of literature and this paper, respectively

Then this computational model was used to compare with the theoretical model. Firstly, single core-shell particle models were compared with each other, as shown in Fig. 29 (a)-(c), which shows a good consistence. It indicates that both the theoretical model and finite element model can well predict the stress evolution and displacement of the core-shell particle in lithiation process. The deviation between theoretical and simulation near the end of first half cycle is mainly attributed to the plastic deformation. This is because the theoretical model is based on the finite elastic deformation assumption. However, this small deviation is acceptable in this work when the model is used to describe the contact behavior described in the following sections. Because the plastic stage of the contact model will be described by another theory while the displacement results of this single core-shell particle model is mainly used to define the stage demarcation. (see Appendix B) Then as discussed in the above text, the theoretical model of two contact core-shell particles is also compared with the computation one and result shows good consistence.

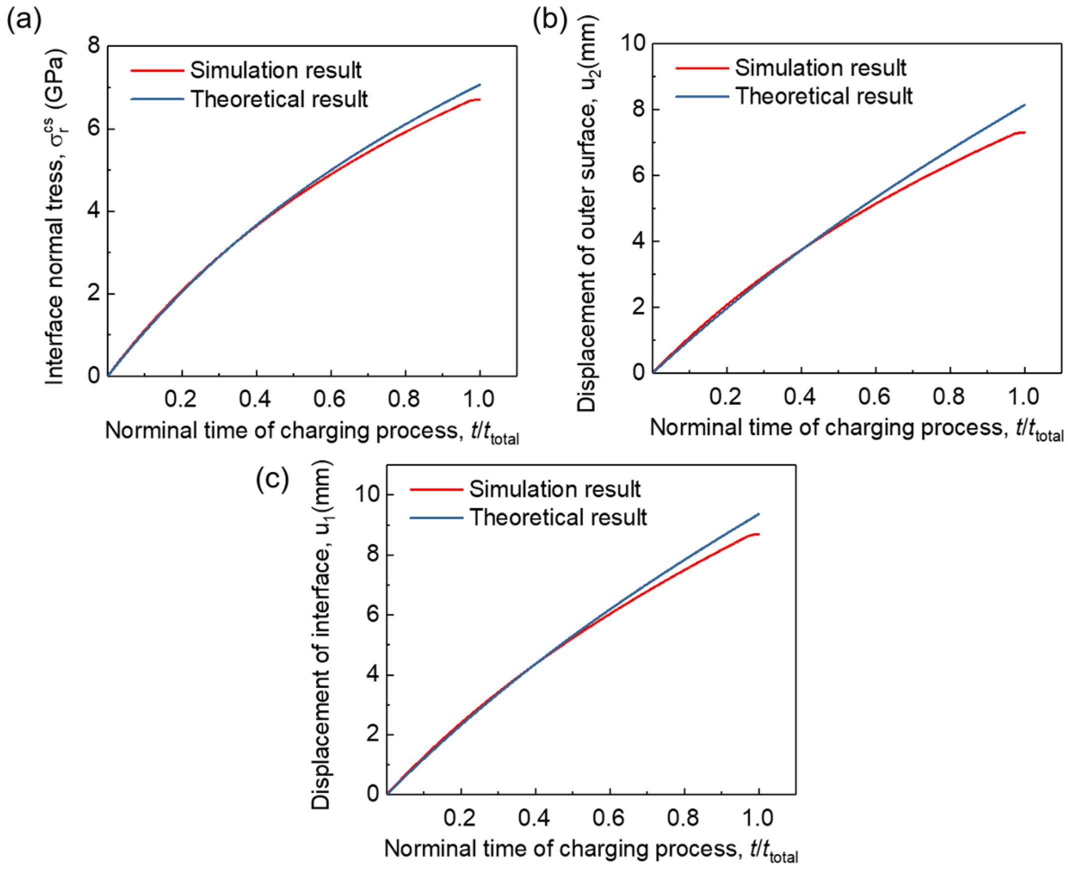

Figure 29 Comparison between simulation results and theoretical model during the first charging process. Comparisons on (a) Si-C interface normal stress; (b) displacement of the Si-C interface; (c) displacement of the outer surface of C shell.

4.1.4 Typical computational results

At every condition (different charging rate, different shell modulus and different shell geometry), both the stress evolution at Si-C interface and contact area of two particles and the displacement of core and shell can be extract from the computational model (see Figs. 30-34).

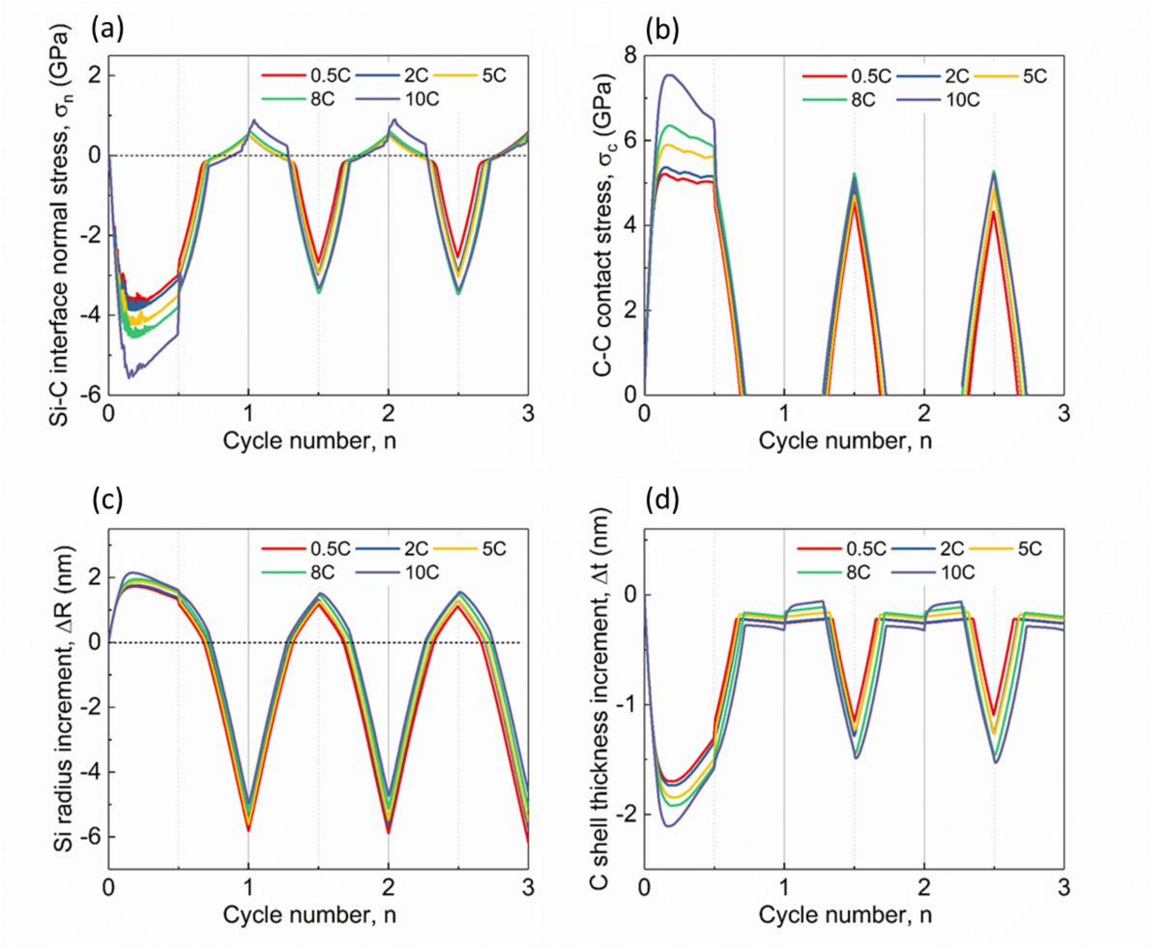

Figure 30 Simulation results for particles with C shell possessing modulus of 20 GPa and thickness of 6 nm during three charging/discharging cycles under different charging rate. (a) is the normal stress evolution at Si-C interface; (b) is the contact stress evolution at C-C contact area; (c) is the Si core radius increment evolution; (d) is the C shell thickness increment evolution.

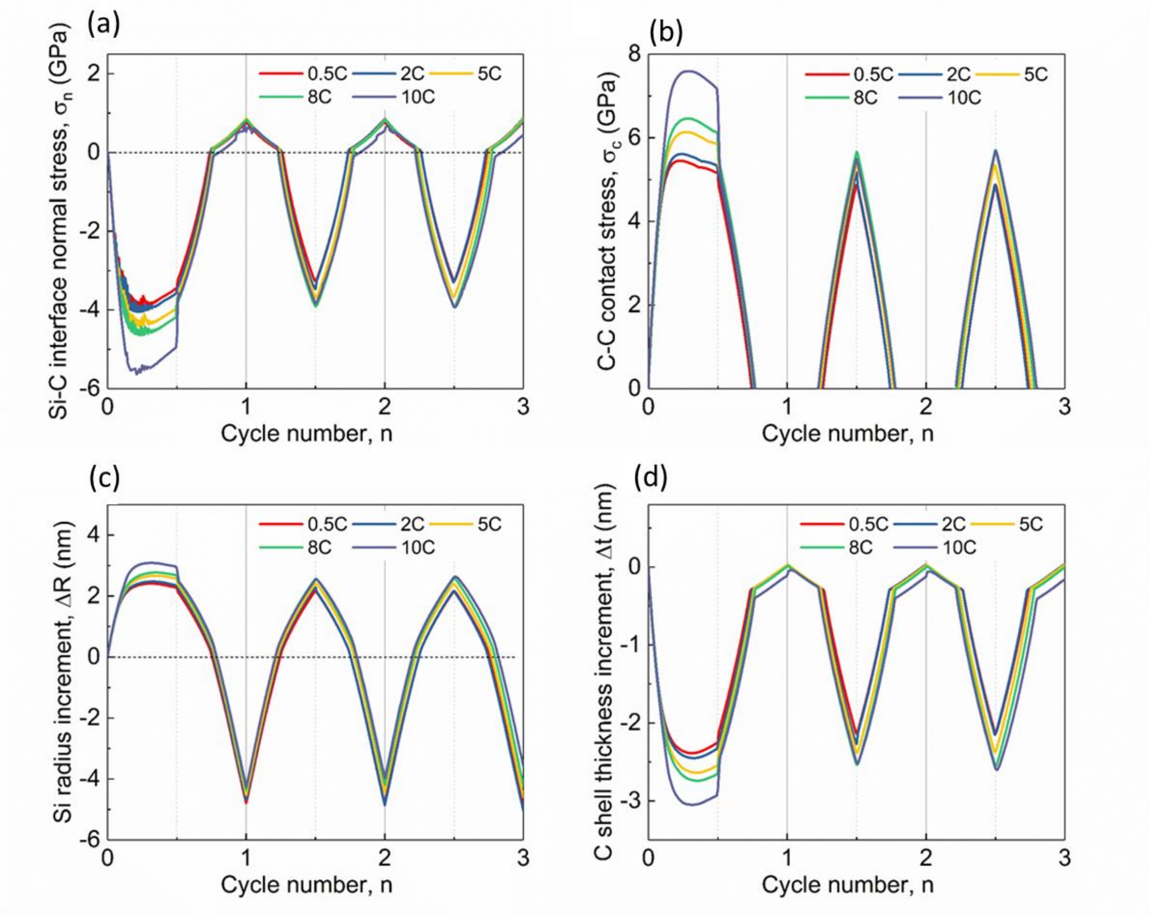

Figure 31 Simulation results for particles with C shell possessing modulus of 20 GPa and thickness of 8 nm during three charging/discharging cycles under different charging rate. (a) is the normal stress evolution at Si-C interface; (b) is the contact stress evolution at C-C contact area; (c) is the Si core radius increment evolution; (d) is the C shell thickness increment evolution.

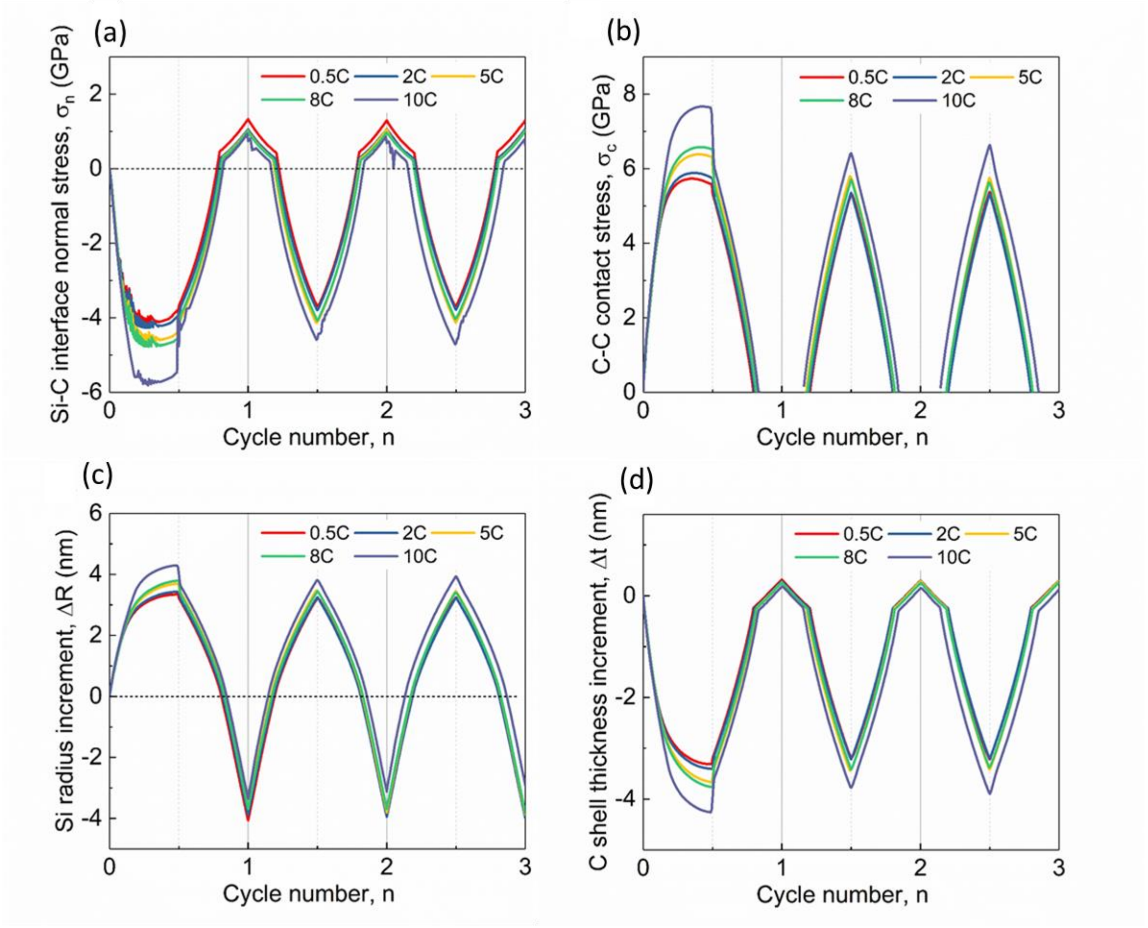

Figure 32 Simulation results for particles with C shell possessing modulus of 20 GPa and thickness of 10 nm during three charging/discharging cycles under different charging rate. (a) is the normal stress evolution at Si-C interface; (b) is the contact stress evolution at C-C contact area; (c) is the Si core radius increment evolution; (d) is the C shell thickness increment evolution.

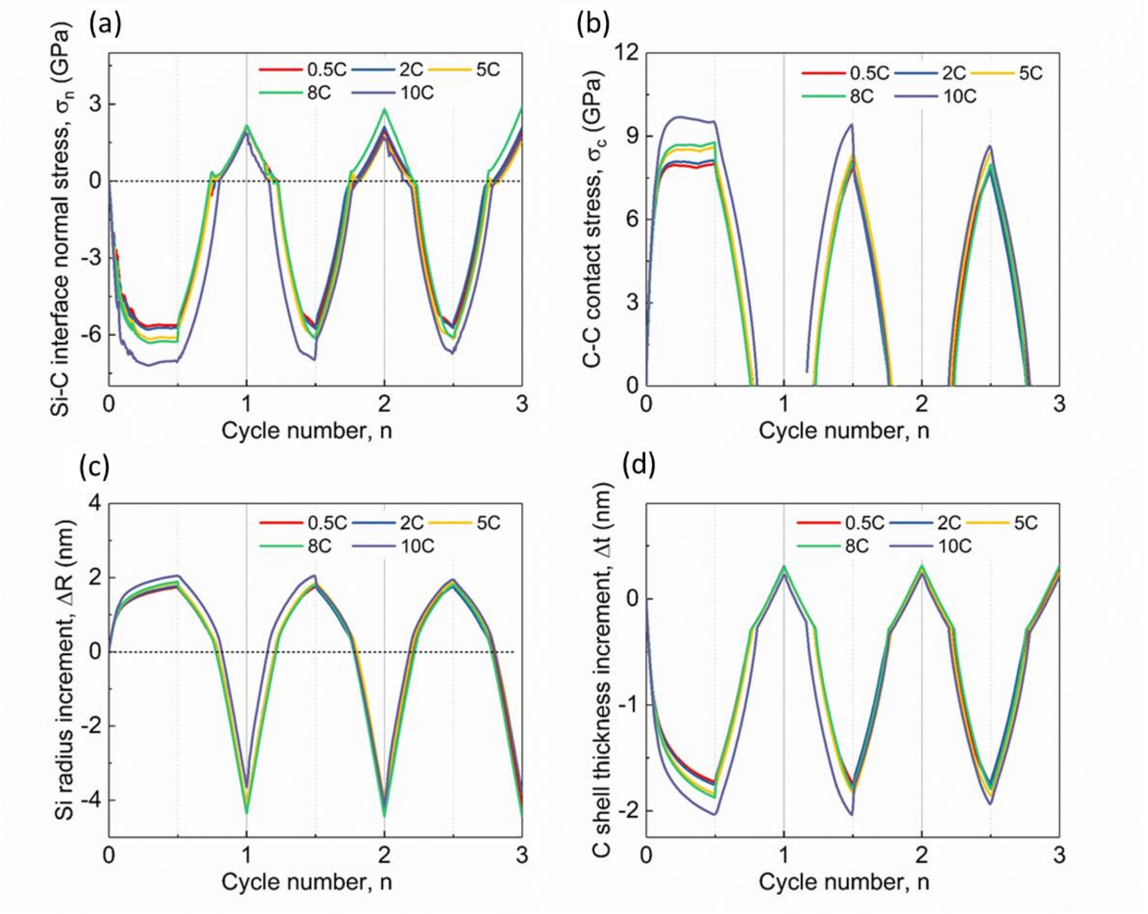

Figure 33 Simulation results for particles with C shell possessing modulus of 60 GPa and thickness of 10 nm during three charging/discharging cycles under different charging rate. (a) is the normal stress evolution at Si-C interface; (b) is the contact stress evolution at C-C contact area; (c) is the Si core radius increment evolution; (d) is the C shell thickness increment evolution.

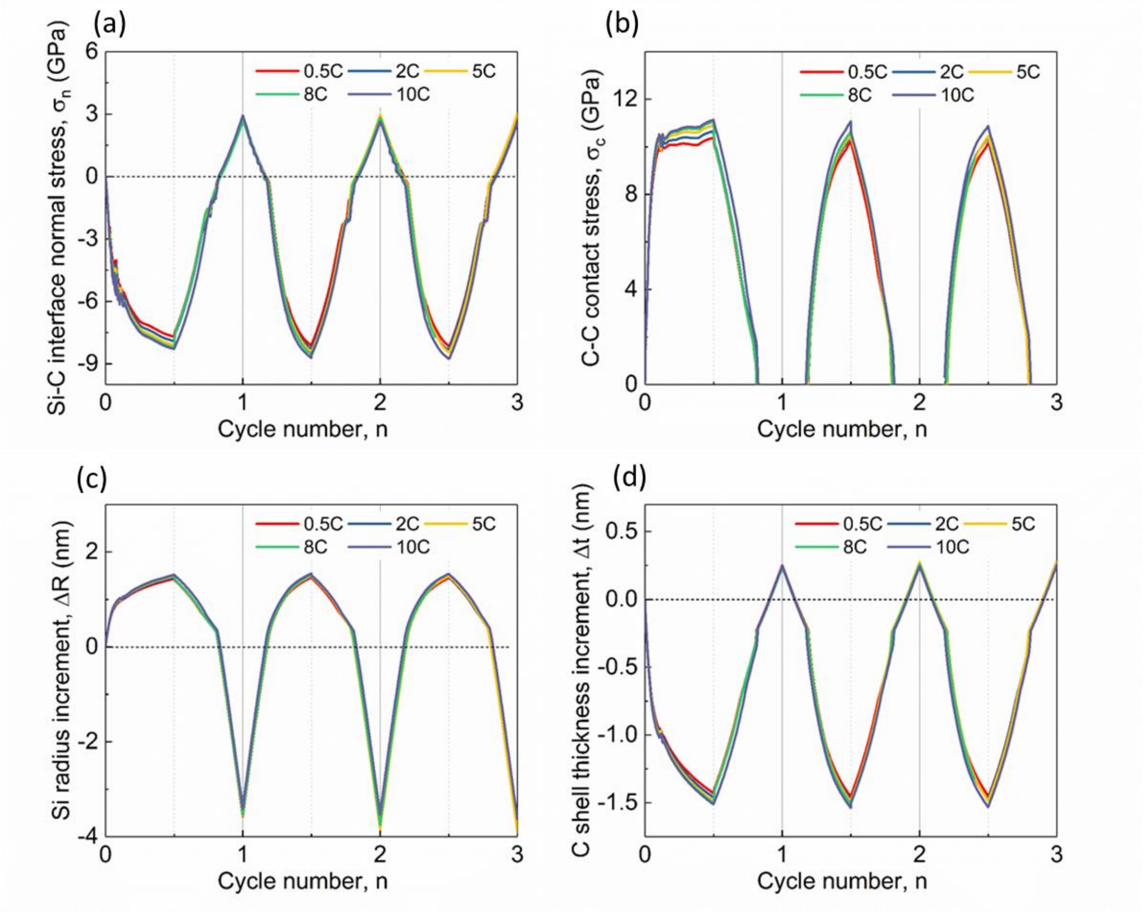

Figure 34 Simulation results for particles with C shell possessing modulus of 100 GPa and thickness of 10 nm during three charging/discharging cycles under different charging rate. (a) is the normal stress evolution at Si-C interface; (b) is the contact stress evolution at C-C contact area; (c) is the Si core radius increment evolution; (d) is the C shell thickness increment evolution.

As shown in Fig. 35, the stress evolution at Si-C interface and C-C contact point, as well as stress distributions and shape changes at some specific time points under 0.5 C charging rate with C shell possessing a 100 GPa modulus and 10 nm thickness are discussed to show the typical tendency. Generally from Fig. 35(a), one may observe that the stress in C shell is bigger than that in Si core, which indicates that the shell in core-shell structure plays a dominate role in protecting core materials. Focusing on the charging process of first cycle, there are two obvious regions that are elastic region and the plastic region. The end of the elastic region, point *a*, is a time point when swelling displacement, $u = \delta_y$, which means Si core begin to yield. As shown in Fig. 35(b), the Si core begins to show an obvious decline of radius under the contact area. Before point *a*, it is the C shell to be compressed by swelling Si core while the radius of Si core increases uniformly without obvious constraint under the contact area. Then the Si core undergoes plastic deformation, which makes the curve show a decline of slop until it reaches its peak value, point *b*. At this point, Si core and contact part of C shell are in the state of compression while the free side of C shell is in the state of tension which is the driving force of shell fracture, as shown in Fig. 35(c). Then in the discharging process of the first cycle, the contact stress shows a nonlinear decrease to zero at point *c*. Two C shells begin to separate from each other that the stress at C-C contact area reaches zero while tensile stress has formed at Si-C interface and in Si core around the contact region, as shown in Fig. 35(d). Finally, at the end of the first cycle, a gap shows between two particles and an obvious region of tensile stress formed around the Si-C interface under the contact area, which is the main driving force for debonding of core and shell, shown in Fig. 35(e). This tensile stress can be attributed to that the plastic contact occurring in the first charging process produces permanent shape change (or plastic deformation). Then the shrink of the Si core in discharging process would produce an effect like dragging on C shell. Since the interface between Si core and C shell is assumed to be perfectly bonded in the simulation procedure, this dragging motion would certainly produce tensile stress.

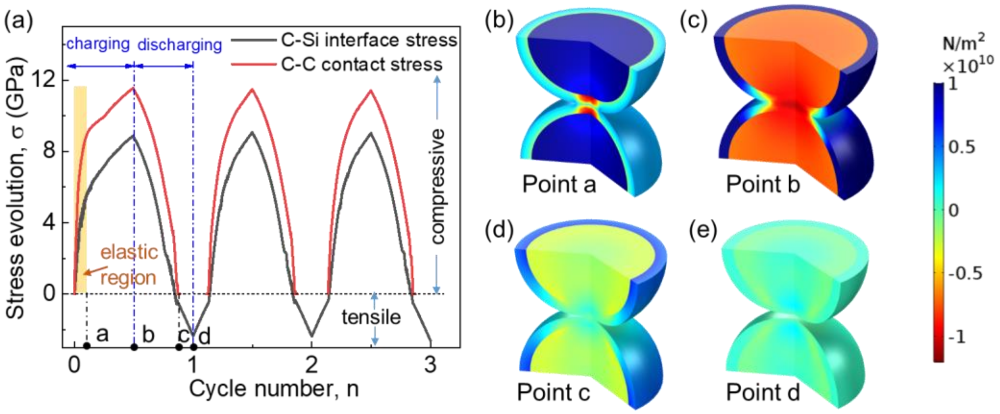

Figure 35 Typical simulation results of two contact core-shell particles with C shell of 10 nm thickness and 100 GPa modulus. (a) Stress evolution curves at the Si-C interface and C-C contact point during three charging/discharging cycles and (b)-(e) stress distributions and shape changes at some specific time points during first cycle that (b) is the initiation of plastic contact at point *a*, (c) is the end of charging process at point *b*, (e) is the time that two C shell separate at point *c* and (e) is the end of a complete cycle at point *d*.

The curves in the second cycle and third cycle are almost the same and are different from the first cycle that there’s no obvious plastic behavior. This can also be attributed to the plastic deformation in the first charging process that when it is charged to the same SOC there will be no plastic contact behavior in the second and all the next cycles. To demonstrate this, a seven-cycling process of this model was studied, and the stress and deformation evolutions from the 2nd cycle to the 7th cycle clearly show that they share almost the same curve, as shown in Fig. 36. Note that such results assume that no fatigue and failure properties are considered in the present model. Therefore, for simplicity, only the first 3 cycles will be discussed in the following parametric studies.

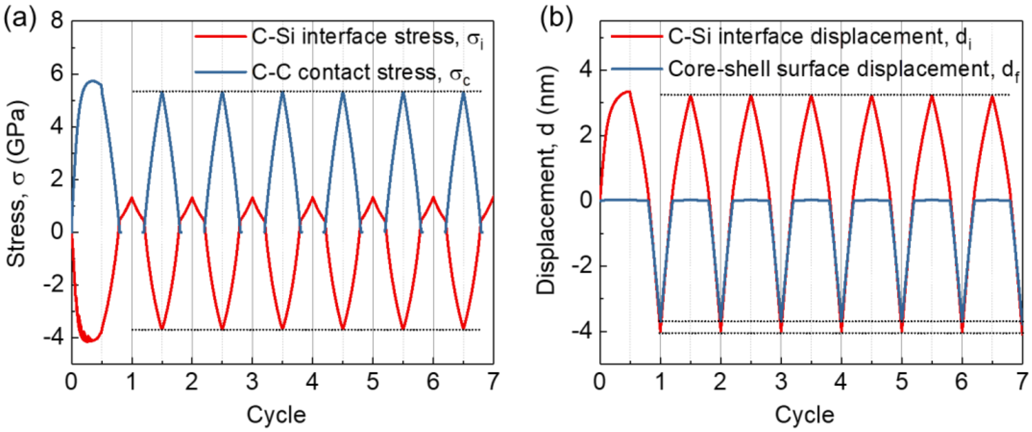

Figure 36 Simulation results for Si/C core-shell contact particles in seven cycles. (a) Stress evolution at the Si-C interface and C-C contact area; (b) deformation evolution at the Si-C interface and the core-shell particle surface.

As mentioned previously, it's difficult to measure the stress within nanoparticle materials. Although the in-situ method has already been applied in measuring stress in thin film materials, the different geometric and boundary conditions make it impossible to use the same method for particle materials. Nevertheless, the experiment results from film material can still be referred to by considering the stress evolution trend and magnitude. In this way, the computational model in the present study is considered to be effective since the governing equations are all demonstrated and widely used by researchers, and the computational results shown in Fig. 35 have a similar trend and stress magnitude with an experimental result in the literature [133]. The differences are mainly caused by the material geometric, boundary condition, electrochemical loading condition, and the scale effect. In return, the effective computational model can be used to reveal the stress-diffusion coupling behaviors which is difficult to be studied through experimental methods, especially the mechanism in such a small scale. Based on this, we may develop new testing method to measure the stress. For nanoindentation machine or atomic force microscopic (AFM) measurements, one may calculate the stress by setting the same boundary and loading condition in the computational model as those in experiments. As such, this model can be used to assist the stress measurement of active particle materials in-situ."

The rate-related effects are included in the computational model. To further evaluate the influence of rate-dependent under various scenarios, e.g., various Young's modulus and thickness of C shell are adopted in simulation. Four typical parameters are extracted to compare and analyze the rate-dependent behavior with different C shell modulus and thickness, i.e. maximum Si-C interface normal stress, $\sigma_n^{\max}$, maximum C-C contact stress, $\sigma_c^{\max}$, maximum Si radius change at cycle end, R/R_0, and maximum C thickness change, $\left(t/t_0\right)_{\max}$, as shown in Fig. 37. The details are discussed in the following two sections.

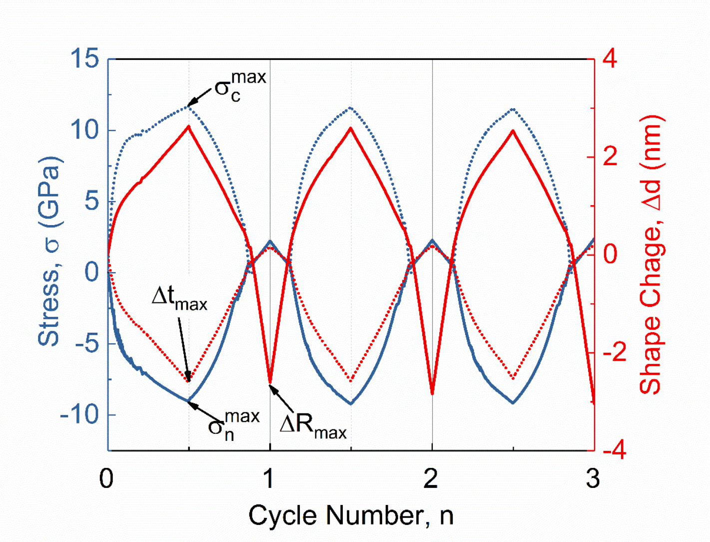

Figure 37 Typical parameters extract from stress curve and deformation curve: maximum Si-C interface normal stress, $\sigma_n^{\max}$, maximum C-C contact stress, $\sigma_c^{\max}$, maximum Si radius change at cycle end, $R/R_0 = (R_0 + \Delta R_{\max})/R_0$, and maximum C thickness change,

$\left(t/t_0\right)_{\max} = (t_0 + \Delta t_{\max})/t_0$.

4.1.5 Rate-dependent analysis

4.1.5.1 Different Young's modulus of C shell

Three different Young's modulus of C shell (20GPa, 60GPa, 100GPa) are adopted in the simulation. Fig. 38(a) shows that $\sigma_n^{\max}$ has evident rate dependency for three different shell moduli. When the charging rate increases, the normal stress at Si-C interface will increase with all three moduli. A stiffer shell will induce higher stress at every charging rate. Note that core-shell particles with lower shell modulus show higher sensitivity to charging rate, which means a stiffer shell material can be used in fast charging conditions on the premise that the stress level doesn't go beyond the fracture limits. On the other hand, the stress in particles with softer shells (20 GPa) would decrease in 2nd and 3rd cycles and keep stable. Similar conclusions can be drawn from Fig. 38(b) that core-shell particles with lower shell modulus show higher sensitivity to charging rate with respect to contact stress, and the stress magnitude decline in 2nd and 3rd cycles would be low. Actually, according to the theoretical model, contact stress is related to interfacial normal stress. Therefore, it is understandable that these two stresses show similar results about the rate dependency.

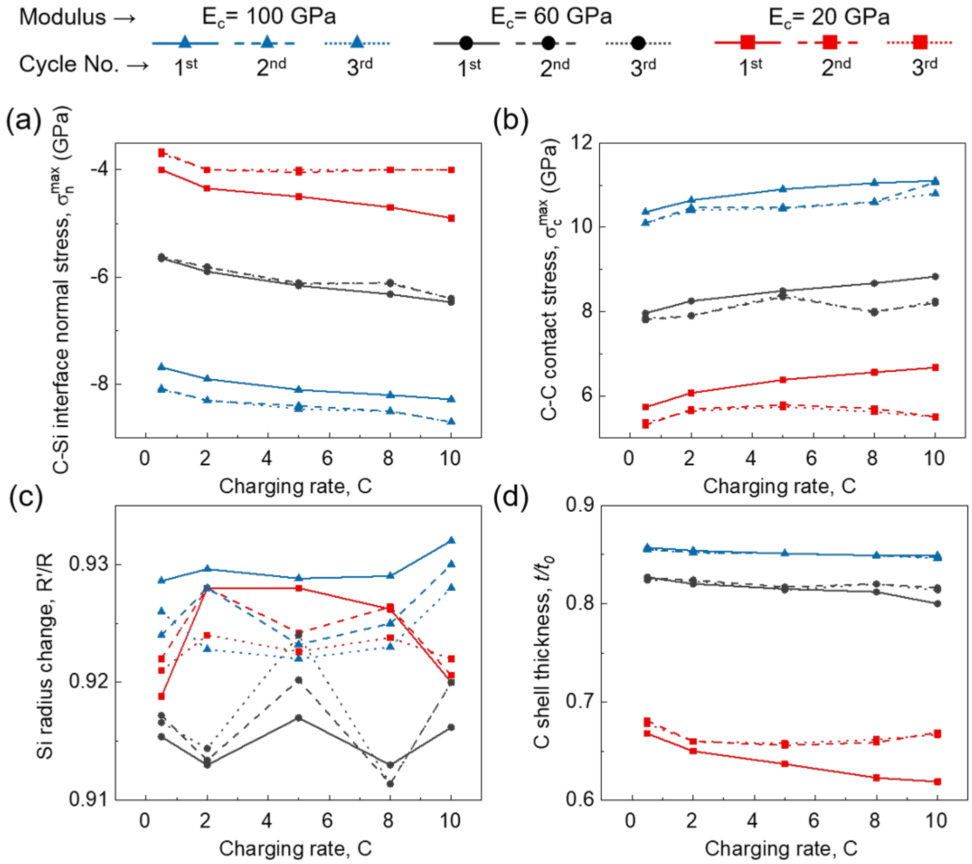

Figure 38 Rate-dependent behavior with different Young's modulus of C shell. (a) is the maximum normal stress at Si-C interface at different charging rates; (b) is the maximum contact stress at C-C contact area at different charging rates; (c) represents the permanent shape change of Si core at cycle end at different charging rates; (d) is the maximum thickness changing of C shell during cycling at different charging rates.

As for deformations, Fig. 38(c) shows that the relation between charging rate and final radius decline at cycling end is not strong. The final Si radius difference among different charging rate is within 0.01 (i.e. 0.5 nm) and can be ignored. Results among particles with three different shell moduli also show little difference (within 0.03, i.e. 1.5nm). Thus, it is safe to conclude that the permanent shape change of Si core almost has no relation with the charging rate and C shell modulus. This may be attributed to that the plastic deformation of Si during lithiation is mainly caused by the swelling of the whole core-shell particle and the constraint from the other particle. According to theoretical results, the total swelling deformation of a free particle could be expressed by Eq. (34) which shows that u_2 is mainly dominated by E_1 (i.e. modulus of Si core). Thus, Si core shape changes with different C shell modulus (E_2) show few differences. However, in terms of C shell thickness, there is an obvious trend that softer C shells are more likely to be compressed during lithiation and are more sensitive to charging rate which means it is easier to fracture, especially in high charging rate, as shown in Fig. 38(d). This also can be explained by the theoretical model. According to Eq. (32) and (34), u_1 decreases with an increasing E_2 while u_2 almost keeps unchanged, so $\left(t/t_0\right)_{\max}$ is smaller with a higher shell modulus. As for rate dependency, the yield stress is higher at a higher charging rate, which induces a longer elastic stage. Then the deformation of Si-C interface (u_1) is larger due to this longer elastic stage before reaching plastic stage. Similar to the stresses, maximus C shell thickness change will keep stable after the second cycle if particles are charged into the same SOC.

To sum up, the core-shell particle with a stiffer C shell is less sensitive to charging rate, and the stiffer shell is less likely to fracture. However, the effects on Li-ion diffusion of hydrostatic stress caused by the shell would not be ignored anymore if the shell is too stiff. An optical value of shell modulus could be obtained through further study.

4.1.5.2 Different thickness of C shell

To see the coupling effect of charging rate and C shell thickness, three different values of C shell thickness (6 nm, 8 nm, and 10 nm) are adopted. Fig. 39(a) shows that C shells of different thicknesses have little effect on the rate sensitivity of Si-C interface stress in the first cycle, and there is little difference between stress magnitudes when shell thickness increases. However, in the 2nd and 3rd cycles, there’s a clearer trend that the stress magnitude is higher while the rate sensitivity is lower with a thicker C shell. Note that in Fig. 39(b), when it comes to contact stress particles with thicker C shell have higher magnitude and is almost equally sensitive to charging rate in the first cycle. In 2nd and 3rd cycle, magnitudes of contact stress are similar to the first cycle that thicker shell induces higher stress, but the sensitivity to charging rate behaves differently with the first cycle that particles with thinner shell are more sensitive from an overall view. All particles with three different thickness values would have a magnitude decline of stress and keep stable in the second and third cycle when they are charged into the same SOC. The difference is that the stress magnitude of particles with the thinner shell would decline more than those with the thicker one. This could be explained by the deformation properties discussed in the following.

Note from Fig. 39(c), a clear trend could be concluded that particles with thicker C shells would have smaller Si permanent shape change while the sensitivity to charging rate is higher in those with thinner shells. This smaller shape change of particle with a thicker shell can also be explained by Eq. (34) that when ratio b/a increases displacement u_2 will decrease, which leads to a smaller permanent shape change. It is also straightforward to understand that a thicker C shell has a stronger constraint to Si swelling during lithiation.

Thus, the reason why particles with thinner shells would show more decline of stress in second and third cycle is that they undergo more plastic deformation in first cycle that it would take them longer to contact with other particles. Then the stress of these particles caused by diffusion and contact will be lower compared to those with thicker shells. As for the C shell thickness change, Fig. 39(d) shows that a thicker C shell is more likely to be compressed. It can be demonstrated by Eq. (32) and (34) that $(u_2\text{-}u_1)/(b\text{-}a)$ will decrease as the ratio b/a increases. The charging rate dependency is almost the same among all the particles with different C shell thicknesses.

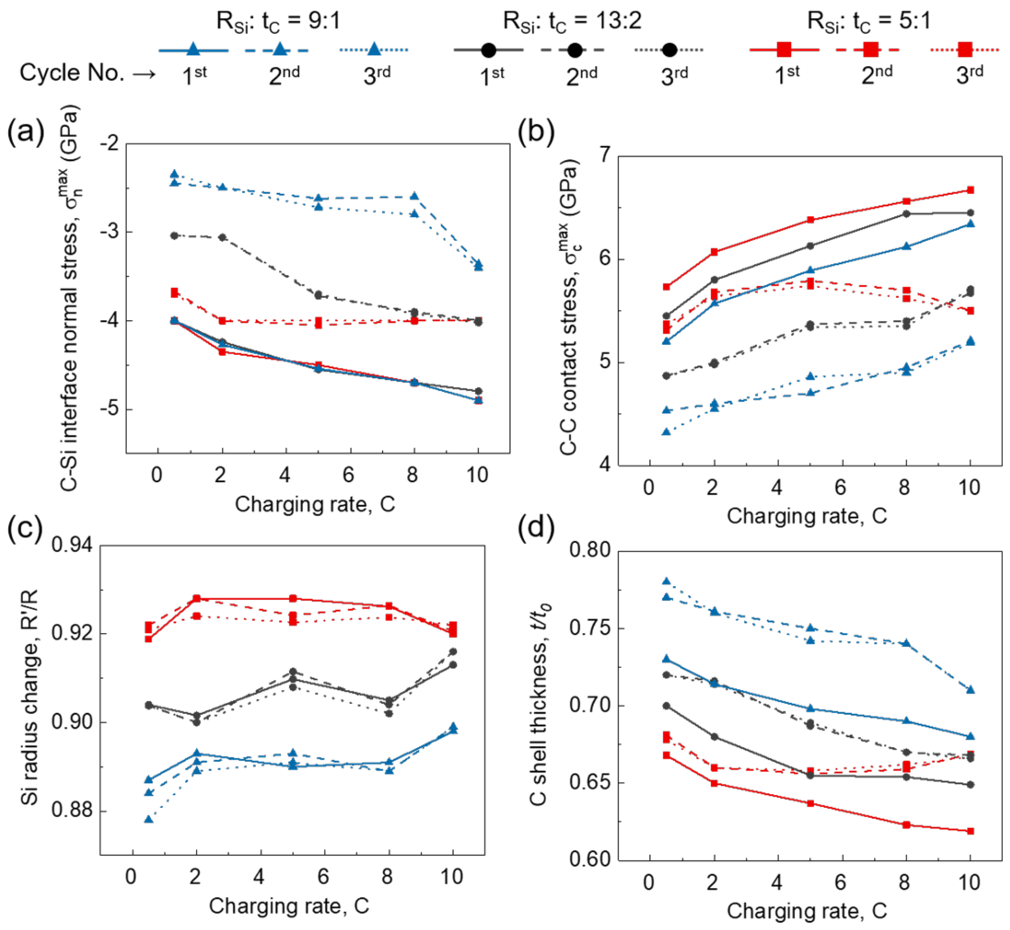

Figure 39 Rate-dependent behavior with different ratios of Si radius and C shell. (a) is the maximum normal stress at Si-C interface at different charging rates; (b) is the maximum

contact stress at C-C contact area at different charging rates; (c) represents the permanent shape change of Si core at cycle end at different charging rates; (d) is the maximum thickness changing of C shell during cycling at different charging rates.

In conclusion, the charging rate shows little dependence to the thickness of C shell that particles with different C shell thickness show similar rate dependency. However, particles with thicker shells produce smaller Si shape change along with nearly the same magnitude of stress. Hence, increasing the thickness of C shell would reduce the possibility of capacity degradation caused by shell failure and reinforce the performance at a high charging rate at the cost of decreasing overall capacity.

4.1.6 Stress and rate-dependent effect on electrochemical performance

As for the electrochemical behavior, a widely known diffusion model is used in the present study as Eqs. (16)-(18) show. Then this model is coupled with the solid mechanics model and applied in the COMSOL platform. Eq. (17) shows that the diffusion flux of lithium-ion depends on the stress field and the same conclusion can be made from Fig. 40. Figs. 40 (a) and (b) are the Li concentration along the particle radius right under the contact point (as the arrow on the first semi-particle in Fig. 40 (c) shows) during charging and discharging under 0.5C charging rate, respectively. Fig. 40 (a) shows that the concentration would decline near the particle surface (contact area), i.e. stress effect area expands. This is mainly attributed to the large stress gradient in that area caused by the contact. Besides, the decreasing of concentration moves toward the particle center along with charging time, as shown in Fig. 40 (a). This can be easily explained that the contact area increases due to the expansion and then causes a larger zone of stress effect, as shown in the first three particles in Fig. 40 (c). However, note that from Fig. 40 (b) and the last three particles in Fig. 40 (c), the stress effect area almost remains the same during the discharging process. This can be attributed to the plastic deformation (i.e., permanent shape change/deformation) that mainly occurs in the first charging process. In the following cycles, the permanent shape change would lead to an unchanged area of the stress effect zone in the discharging process.

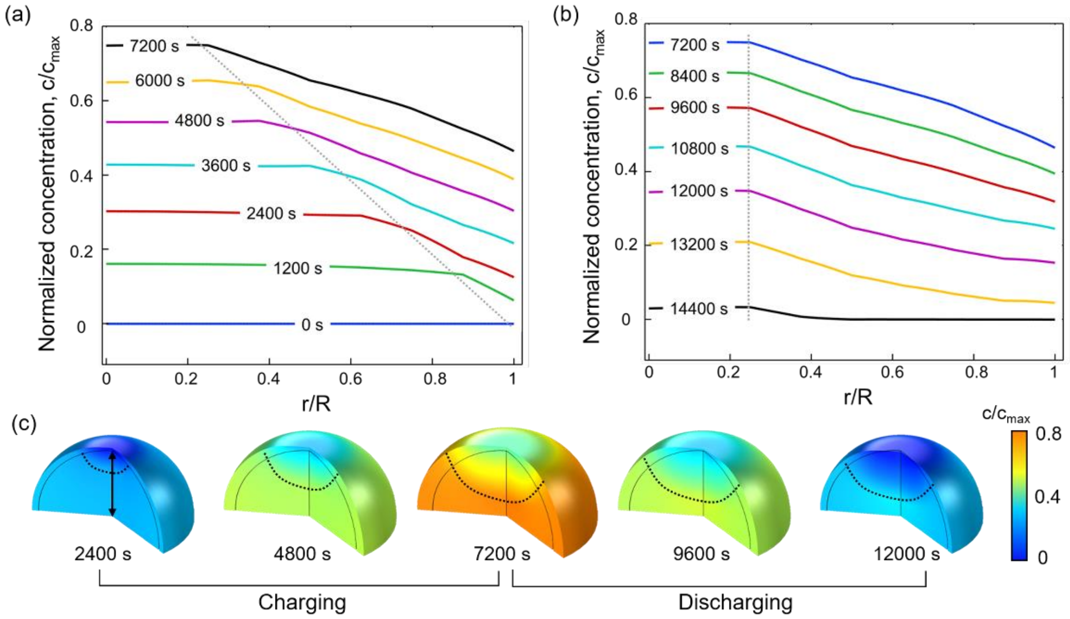

Figure 40 Lithium-ion concentration in radial direction under contact area with 0.5C charging rate. (a) Concentration distribution at different time during charging process; (b) concentration distribution at different times during charging process; (c) concentration distribution within the Si particle in the complete charging/discharging cycling. (The dot line in (c) indicates the obvious boundary of stress high effect and low effect zones)

One can know from section 4.5 that the stress magnitude would increase when the charging rate increases. To study the rate-dependent effect on the electrochemical performance, the Li^+ concentration distribution in radial direction under 0.5C and 10C are compared representatively, as shown in Fig. 41. It indicates that the rate-dependent property has little effect on the Li+ diffusion, as Fig. 41 (a) shows. To explain this, the hydrostatic stress gradient at two specific time points in 0.5C and 10C are extracted and compared in Fig. 41 (b). According to Eq. (17), the stress mainly affects the Li^+ diffusion by stress gradient. Fig. 41 (b) shows that the hydrostatic stress gradients of 0.5C and 10C charging rate cases have little difference. Thus, we may conclude that even the higher rate may increase the stress both at the contact area and within the particles which may further cause the mechanical failure of the particle, the Li^+ diffusion may be influenced less from higher rates before the particle fracture occurs.

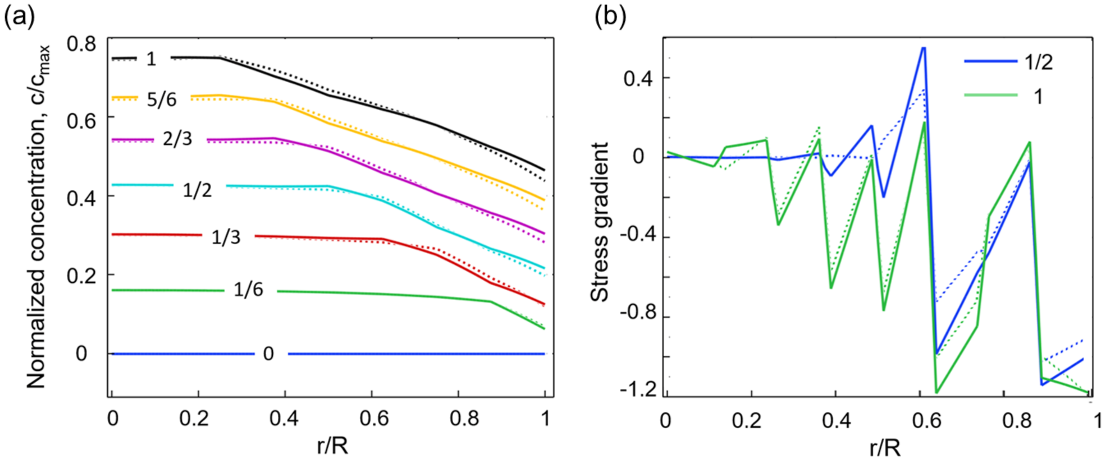

Figure 41 Lithium-ion concentration distribution and stress gradient distribution. (a) Lithium-ion concentration distribution and (b) Hydrostatic stress gradient distribution at two specific time points in radial direction under contact area with 0.5C and 10C charging rate, respectively. (The solid line and dot line represent the results in 0.5C and 10C charging cases, respectively; the numbers (i.e. 0, 1/6, 1/2, etc.) are dimensionless charging cycle (i.e. current time divided by total charging time))

4.1.7 Conclusions

An axisymmetric finite element computational model about two contact Si-C core-shell particles were developed to investigate the rate-dependent mechanical behavior during lithiation/delithiation cycling. In the meantime, a theoretical model on the contact core-shell particles was developed by dividing the whole charging process into three stages, i.e., elastic stage, mixed elastic-plastic stage, and plastic stage, which could help to explain the mechanism of mechanical behaviors. The theoretical model can well consist of the typical numerical computation results (0.5 C charging rate without rate effects). To study the rate-dependent behavior, five charging rates (0.5C, 2C, 5C, 8C, and 10C) were applied in FE model. Besides, three different shell modulus and thickness were considered in simulation as well. Results show that particles with softer C shells are more sensitive to charging rate with respect to Si-C interface normal stress and C-C contact stress. When it comes to particles with different thicknesses, all parameters show rate dependency, but only parameters in 2nd and 3rd cycles show different sensitivity among different initial thicknesses that particles with a thinner shell are more sensitive. It also indicates that particles with stiffer C shell would exhibit high stress but are less likely to fracture, while particles with a thicker C shell would produce less Si permanent shape change with not so high stress. In other words, core-shell particles with stiffer and thicker C shells would reduce the Si swelling and permanent shape change at the cost of capacity decline. In terms of electrochemical performance, the contact behavior would cause a high nonuniform stress gradient which influences the Li^+ diffusion. However, high rates show a similar effect on the diffusion behavior as low rates. To conclude, an optimal assembly can be obtained by further calculation based on this study, and the methodology in this paper would provide a guideline on core-shell structure design for future high capacity batteries aiming to fast charging.

4.2 Modeling on Si/C Composite Nanostructures

4.2.1 Method

Five representative structures are considered in this part (Fig. 42)

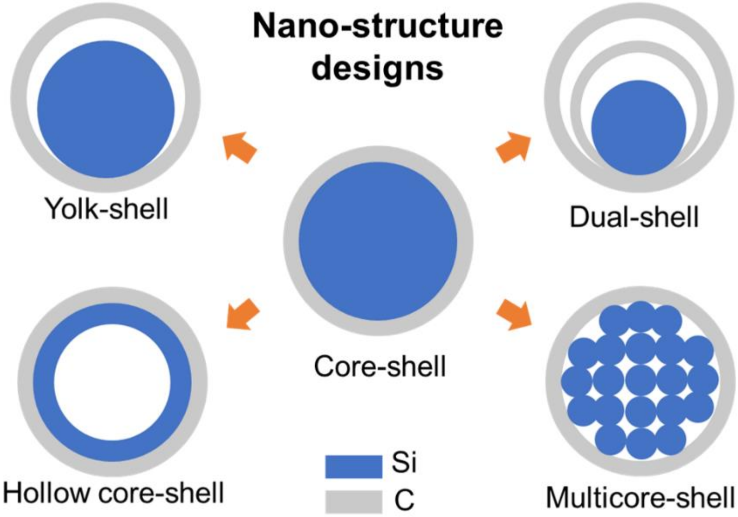

Figure 42 Five representative nanostructures designed for Si/C composite anode nanomaterials used in this study. Core-shell is the basic structure; the four other structures are evolved based on the core-shell structure.

In the modeling part of the present paper, two assumptions are adopted to achieve this governing mechanism: the continuity of (i) electrochemical potential and (ii) Li^+ flux at the interface of Si core and C shell. For the diffusion behavior in both the Si core and C shell, it is simplified by the classic Fick's second law holds as follows:

$$\frac{\partial c_s}{\partial t} + \nabla \cdot \mathbf{J} = 0\,, \tag{35}$$

where the Li-ion flux **J** can be expressed as Eqs. (17) and (18). To solve the above partial differential equations, the weak form of Eq. (35) is developed as follows:

$$\int_{S}\left(\frac{\partial c}{\partial t}+\nabla\cdot\mathbf{J}\right)\cdot\hat{c}\mathrm{d}S=0. \tag{36}$$

Taking the core-shell structure as an example, the weak forms for Si core (subscript "Si") and C shell (subscript "C") can be expressed as

$$\begin{aligned}
&\int_{S_{Si}}\left(\begin{array}{l}-\hat{c}_{s,Si}\dfrac{\partial c_{s,Si}}{\partial t}+A_{Si}\left(\dfrac{\partial \hat{c}_{s,Si}}{\partial x}\dfrac{\partial c_{s,Si}}{\partial x}+\dfrac{\partial \hat{c}_{s,Si}}{\partial y}\dfrac{\partial c_{s,Si}}{\partial y}\right)\\ +B_{Si}\left(\dfrac{\partial \hat{c}_{s,Si}}{\partial x}\dfrac{\partial \sigma_{h,Si}}{\partial x}+\dfrac{\partial \hat{c}_{s,Si}}{\partial y}\dfrac{\partial \sigma_{h,Si}}{\partial y}\right)\end{array}\right)\mathrm{d}S_{Si}\\
&=\int_{\Gamma_{Si}}\hat{c}_{s,Si}(\mathbf{J}_{Si}\cdot\boldsymbol{\upsilon})d\Gamma_{Si}\\
&\int_{S_{C}}\left(\begin{array}{l}-\hat{c}_{s,C}\dfrac{\partial c_{s,C}}{\partial t}+A_{C}\left(\dfrac{\partial \hat{c}_{s,C}}{\partial x}\dfrac{\partial c_{s,C}}{\partial x}+\dfrac{\partial \hat{c}_{s,C}}{\partial y}\dfrac{\partial c_{s,C}}{\partial y}\right)\\ +B_{C}\left(\dfrac{\partial \hat{c}_{s,C}}{\partial x}\dfrac{\partial \sigma_{h,C}}{\partial x}+\dfrac{\partial \hat{c}_{s,C}}{\partial y}\dfrac{\partial \sigma_{h,C}}{\partial y}\right)\end{array}\right)\mathrm{d}S_{C}\\
&=\int_{\Gamma_{C}}\hat{c}_{s,C}(\mathbf{J}_{C}\cdot\boldsymbol{\upsilon})d\Gamma_{C}-\int_{\Gamma_{Si}}\hat{c}_{s,C}(\mathbf{J}_{Si}\cdot\boldsymbol{\upsilon})d\Gamma_{Si}
\end{aligned}\quad, \tag{37}$$

where $\boldsymbol{\upsilon}$ is the normal vector of the boundary Γ. The initial conditions and boundary conditions are listed here:

$$c_{s,Si}=c_{s,Si}^{0},\ c_{s,C}=c_{s,C}^{0}\ \text{ at }\ t=0 \tag{38}$$

$$\nabla c_{s,C}=0\ \text{ at }\ x,y=0 \tag{39}$$

$$\mathbf{J}_{2}\cdot\boldsymbol{\upsilon}=\frac{V_{Si}c_{s,Si}^{\max}+V_{C}c_{s,C}^{\max}}{S}C/t\ \text{ at boundary}\ \Gamma_{C}, \tag{40}$$

where t = 3600 s. To accurately describe the electrochemical behavior of the Si/C composite materials, the chemical potential and lithium-ion flux are assumed to be continuous across the core-shell interface:

$$\begin{matrix} \mu_{Si} = \mu_C \\ \mathbf{J}_{Si} \cdot \boldsymbol{\upsilon} = \mathbf{J}_C \cdot \boldsymbol{\upsilon} \end{matrix} \quad \text{at boundary } \Gamma_{Si} \tag{41}$$

For mechanical behavior, the equilibrium equation is

$$\nabla \cdot \mathbf{T} + \mathbf{B} = 0 \tag{42}$$

where **T** is the nominal stress calculated by **T = C : E**, with stiffness matrix **C** and elastic strain matrix **E**, and **B** is the body force, which equals zero here. According to the multiplicative decomposition law, the total deformation can be expressed as

$$\mathbf{F} = \mathbf{F_e} \cdot \mathbf{F_p} \cdot \mathbf{F_l}, \tag{43}$$

where **F** represents the deformation gradient and the subscripts "**e**," "**p**," and "**l**" represent elastic distortion, plastic deformation, and lithiation-induced volumetric deformation, respectively. The volumetric deformation is related to the Li^+ concentration, *c*. The yield law used here is the Von Mises law, and the hardening model is the perfect plasticity model. The displacement and radial stress at the core-shell interface are continuous as

$$\begin{matrix} u_{Si} = u_C \\ \sigma_{rr,Si} = \sigma_{rr,C} \end{matrix} \quad \text{at boundary } \Gamma_{Si}. \tag{44}$$

As Equations (17), (18) and (43) indicate, the diffusion model and mechanical model are coupled by transferring parameters σ_h and *c* between the two models. All the governing equations are applied to the specific structures and calculated via the COMSOL platform (COMSOL 5.3).

To study the performance of different nanoparticle structures considering the effects of surrounding particles, we select a representative volume element (RVE) to describe the behaviors of the entire anode. Without the loss of generality, we adopt a regular stacking with a stacking density of 0.68 to represent the stacking configuration of the battery anode. Then, to save the computational time and sources, as well as to obtain better convergence, we apply 2D simplification (Fig. 43a). For the modeling part, we define the contact area between C and Si to be a small circle (same in all cases with a radius about 25 nm) here to match the real situation in the Si/C yolk-shell related structure (Structures 2 and 3). For simplicity and without consideration of the anode level or cell level mechanical deformation, the symmetric boundary condition is applied on each side of the RVE, and Li^+ flux is imposed on the surface of each designated nanoparticle (Fig. 43a). The Si core and C shell are bonded together at the interface. For core-shell and multicore-shell structures, the middle points of the RVE are assumed to be fixed. To compare the electrochemical properties among different nanostructures, we keep the same charging/discharging rate (1 C) in all simulation cases.

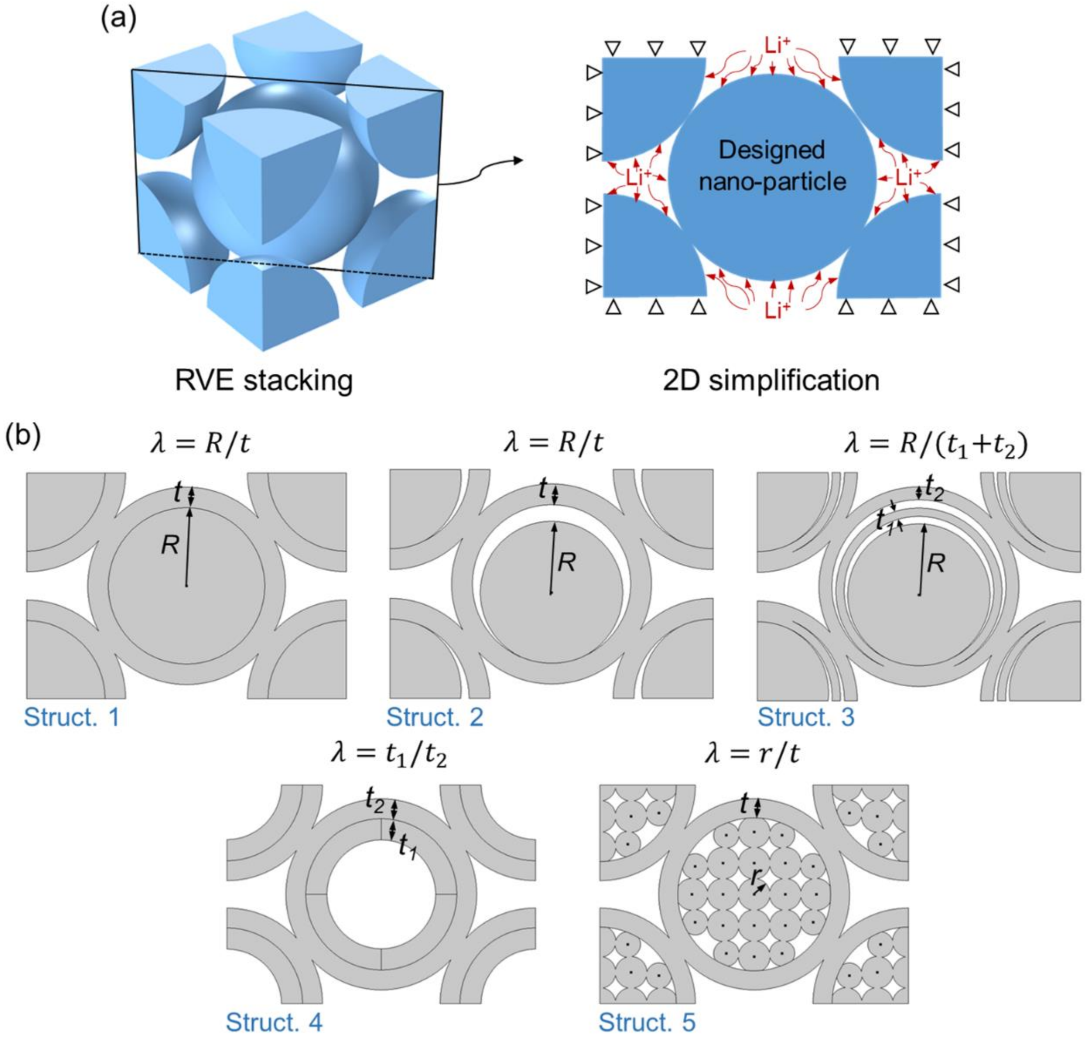

Figure 43 Illustration of simulation settings of (a) geometry model simplification and boundary conditions of mechanical and electrochemical sub-models and (b) parametric settings for different nanostructures. The ratios, λ, and all the geometric parameters in structure 1~5 are listed in Table 5.

In the present study, five representative structures are targeted: core-shell (Structure 1), yolk-shell (Structure 2), dual-shell (Structure 3), hollow core-shell (Structure 4), and multicore-shell (Structure 5) (Fig. 43b). The ratio λ is defined as the ratio of Si core-related geometry factor (radius or thickness) and C shell thickness (Fig. 43b), which represents the proportion of Si core and C shell that a large value of λ means a large proportion of Si. When selecting the geometric parameters of the yolk-shell structure, the void space should not exceed the maximum value calculated as $V_{\mathrm{void}}^{\max} = \frac{4}{3}\pi(c_{\mathrm{s,max}}\Omega - 1)R_{\mathrm{Si}}^{3}$, which is enough to hold the expansion of Si core. Through this way, space is fully utilized to ensure a high actual capacity. For each structure, three different configurations with different λ are considered (Table 5). Different structures share the same material properties (i.e., the Si core) and C shell material (Table 6).

Table 5 Geometric parameters and core-shell ratios of different nanostructures

Structure	Configuration	R (r), nm	t, nm t_1, nm	 t_2, nm	λ
1	1	80	20		$\lambda_1 = 4$
	2	75	25		$\lambda_2 = 3$
	3	70	30		$\lambda_3 = 2.33$
2	1	72	20		$\lambda_1 = 3.6$
	2	68	20		$\lambda_2 = 3.4$
	3	64	20		$\lambda_3 = 3.2$
3	1	72	8	12	$\lambda_1 = 3.6$
	2	68	8	12	$\lambda_2 = 3.4$
	3	64	8	12	$\lambda_3 = 3.2$
4	1	\	32	20	$\lambda_1 = 1.6$
	2	\	22.4	20	$\lambda_2 = 1.12$
	3	\	20	20	$\lambda_3 = 1$
5	1	17.02	20		$\lambda_1 = 0.851$
	2	16.49	20		$\lambda_2 = 0.825$
	3	16	20		$\lambda_3 = 0.8$

Table 6 Input parameters and values in the established multiphysics model

Parameter	Symbol	Value
Partial molar volume of Si[121]	Ω_{Si}	9×10^{-6} $\mathrm{m^3/mol}$
Partial molar volume of C[134]	Ω_{C}	3.17×10^{-6} $\mathrm{m^3/mol}$

Modulus of Si[122]	E_{Si}	$E_{Si}\ (c_{Si})$
Modulus of C[134]	E_C	$19.25 + 82.23x$ GPa
Maximum Li concentration in Si[119]	$c_{s,\mathrm{Si}}^{\max}$	278,000 mol/m^3
Maximum Li concentration in C[135]	$c_{s,\mathrm{C}}^{\max}$	31,507 mol/m^3
The diffusion coefficient in Si[121]	$D_{0,Si}$	1.67×10^{-14} m^2/s
The diffusion coefficient in C[136]	$D_{0,C}$	1×10^{-9} m^2/s
Yield stress of Si[137]	$\sigma_{y,Si}$	$\sigma_{y,Si}^0 - 0.9(c_C / c_{C,\max})$ GPa
Initial yield stress of Si[137]	$\sigma_{y,Si}^0$	1.5 GPa

4.2.2 Li^+ diffusion analysis

The core multiphysics behavior for Si/C composite particles described here should be the coupling of the Li^+ diffusion process and mechanical response of the nanostructures. The open-circuit potential (OCP) curves of Si [138] and C [139] were selected after a pre-study of various OCP curves from references [138, 140-142] about the key factors concerned in this manuscript (Appendix C and Figs. C1-3), which can be divided into two representative stages: the potential of C is larger than that of Si in Stage I, while it changes to a lower one in Stage II (Fig. 44a). According to the previous study, the Li^+ diffusion behavior is highly related to material OCP.[60] Therefore, the diffusion process in the core-shell structure can be described analogizing from the Ref. [60] as follows (Fig. 44b). In stage I, most of the Li^+ from the electrolyte will preferentially diffuse into the C shell, and only a small portion of lithium ions are alloyed with the Si core. In contrast, the process in stage II is that most of the Li^+ pass through the shell and is first alloyed with the Si core. For yolk-shell related structures, the diffusion mechanism should be identical, except that the Li^+ diffusion path at Si/C interface in yolk-shell structure provides a relatively narrow path for Li^+ to pass through (Fig. 44c). The diffusion process in the anode material is usually complex, however, it is simplified as Fick’s second law in this study when focusing on the mechanical failure behavior, overall electrochemical capacity performance, and the corresponding coupling effects.

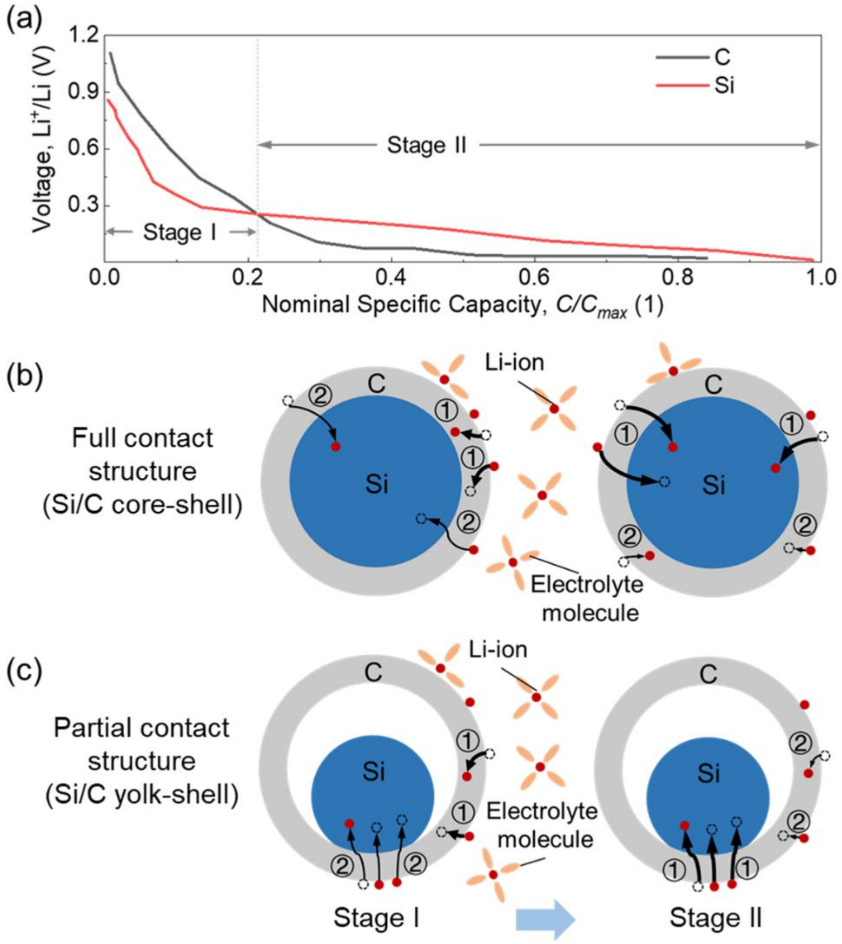

Figure 44 (a) OCP curves of Si and C [138, 139], and illustration of basic lithium-ion diffusion process for (b) core-shell structure and (c) yolk-shell structure. ① is the first priority diffusion path, and ② indicates the secondary priority path.

4.2.3 Si/C mechanical behavior and failure mode

In this study, each of the selected five nanostructures has three different configurations, defined by the ratio of Si core related geometry factor (radius or thickness) and C shell thickness. Here, the mechanical behavior and failure modes of the core-shell structure (Structure 1) that is 200 nm in diameter are selected to show the typical response of such nanostructures during the lithiation/delithiation cycling (Fig. 45). The radius of the Si core and the thickness of the C shell of the three configurations are 80–20, 75–25, and 70–30 nm, respectively.

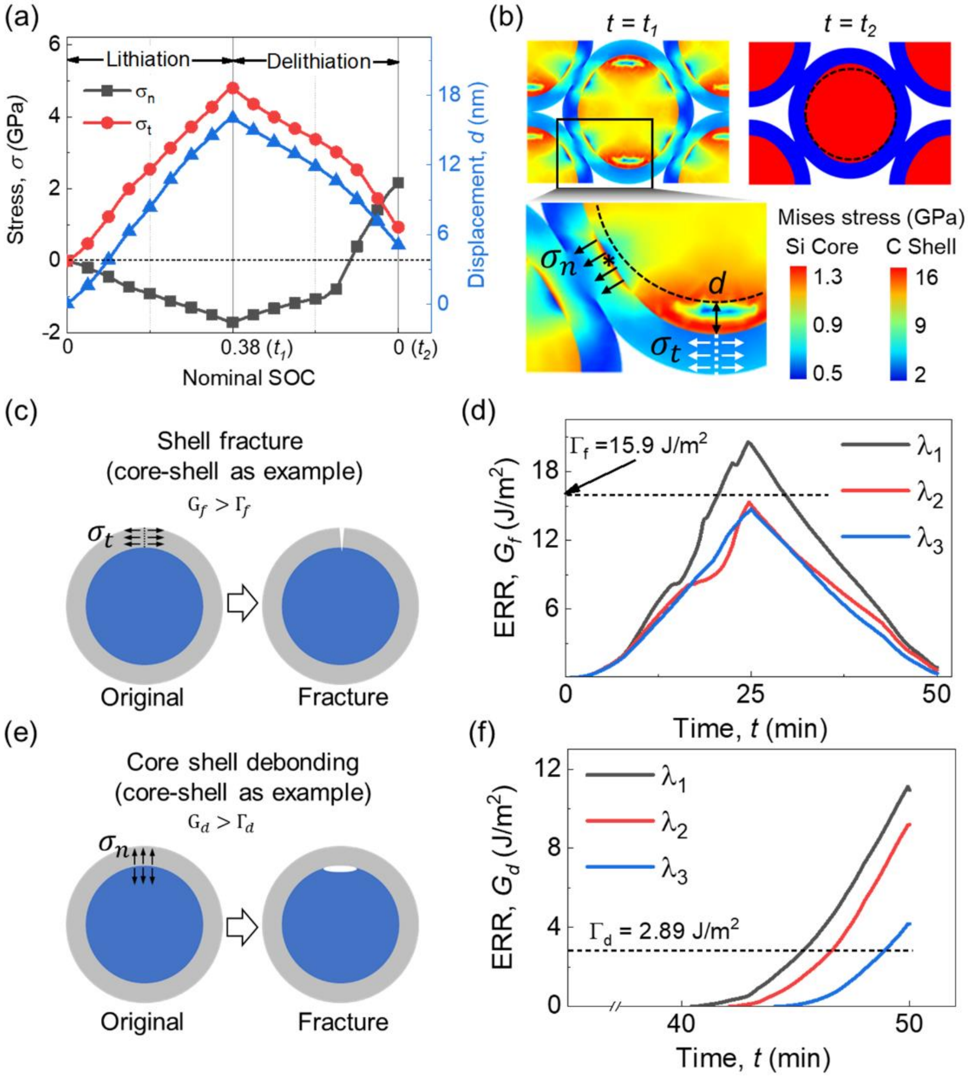

Figure 45 Computation results of a core-shell structure (Structure 1) during lithiation-

delithiation cycling. (a) Maximum normal stress and hoop stress evolution, and deformation profile; (b) Von Mises stress contour plots at the end of lithiation, t_1, and the end of delithiation, t_2; definition of (c) shell fracture and (e) core-shell debonding; energy release rate evolution of (d) shell fracture and (f) core-shell debonding of three configurations (λ_1, λ_2, λ_3 defined in the Method section) of core-shell structure.

As shown in Fig. 45a, the normal stress σ_n at the core-shell interface is in compressive stress status and increases (becoming more negative) during lithiation. This compressive stress is caused by the resistance of the C shell to the expansion of the Si core preventing an ultra-large deformation in lithiation. At the end of lithiation ($t = t_1$), a non-uniform distribution of normal stress σ_n in the Si/C bulk is observed as shown in Fig. 45b. At the core-shell interface, the maximum normal stress occurs in the contact area of two particles, and the maximum compressive stress is in the center of the C shell at the corresponding contact area. As for Si core, the stress is symmetrically distributed with the maximum normal stress occurring at the same position under the contact area. During the delithiation process, normal stress σ_n decreases (smaller absolute value; here, "positive" and "negative" refer to the "tensile" and "compression" stresses, respectively). At the end of delithiation ($t = t_2$), the maximum stress in the Si core is close to the yield stress of the Si material with a perfect plastic model (where plastic stress equals the yield stress all the time) applied. The Si core cannot resume its original shape due to the plastic deformation (Fig. 45b). This shape change further promotes normal stress (tensile) near the end of delithiation in Fig. 45a, which could lead to a debonding failure of the core-shell. The relatively uniformly distributed stress with a value of ~1.5 GPa (yield stress) is caused by the addition of the residual stress and the increased modulus.

When the particle is in lithiation, the expansion of the Si core produces the tensile hoop stress σ_t in the shell, as shown in Fig. 45b. Such tensile stress is the reason for the C shell fracture. We observe that the general profile of σ_t is very similar to that of displacement d because it is the deformation of the core that generates the hoop stress in the shell (Fig. 45a). The maximum hoop stress occurs in the C shell, where there is no contact (Fig. 45b). The magnitude and evolution of the stress in Fig. 45a demonstrates good agreement with the ab initio calculations [78] and multibeam optical stress sensor (MOSS) data [74] from the previous literature, respectively, qualitatively validating the model.

Generally, nanosized Si particles (R < 100 nm) do not fracture during cycling. Thus, in this study, only the C shell fracture and core-shell debonding are considered. The fracture energy release rate (ERR), G_f, describing the fundamental driving force of the fracture, serves as a key parameter to describe the failure behavior among various structures, and it can be defined in Equation (45) as

$$G_f = Z\left(\bar{\sigma}_{\theta\theta}\right)^2 t / E_C, \tag{45}$$

where $\bar{\sigma}_{\theta\theta} = \left(2\int_{R_{in}}^{R_{out}} \sigma_{\theta\theta} r \mathrm{d}r\right)/t$ is the average hoop stress in the C shell. Since the hoop stress is not tangentially uniform, the maximum mean value, which represents the most dangerous position (Fig. 46), is adopted in Equation (1). Here, $Z = 2$ for channel crack in a spherical shell and $t = R_{out} - R_{in}$ is the shell thickness. If G_f is larger than the critical value Γ_f, the shell fractures (Fig. 45c). The fracture toughness of nanosized carbon is taken as $\Gamma_f = 15.9$ J/m^2.[143]. The ERR of core-shell debonding, G_d, is given by Equation (46):

$$G_d = \pi (\sigma_n)^2 t / E_e, \tag{46}$$

where $E_e = 2E_{Si}E_C / (E_{Si} + E_C)$ is the effective Young's modulus. Similarly, the maximum normal stress at the interface is used as σ_n here (Figs. 45b and 47). If G_d is larger than the critical value Γ_d, the shell and core separate and thus form a debonding-type fracture (Fig. 45e). The critical energy release rate for core-shell debonding is set as Γ_d =2.89 J/m^2.[78]

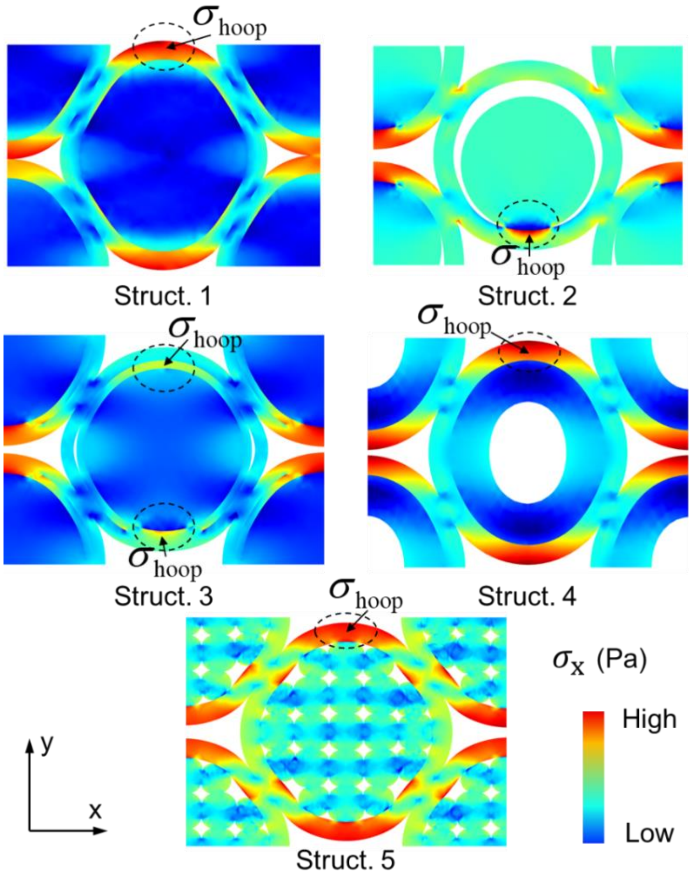

Figure 46 Stress component (x-direction) distribution in different structures. The place most likely to fracture is marked by the dashed circle, where the maximum hoop stress is indicated.

The ERR of shell fracture (G_f) increases during lithiation and exceeds the critical value, about 21 J/m^2, for the λ_1 = 4 configuration in the core-shell structure (Fig. 45d). With this configuration, a greater Si core proportion can directly lead to a more substantial swelling effect on the C shell, which in return causes more substantial hoop stress and shell fracture. However, the shell fracture is less likely to happen for a Si/C composite with lower configuration numbers ($\lambda_2 = 3$ and $\lambda_3 = 2.33$). For core-shell debonding, ERRs (G_d) of all the core-shell structures with λ_1, λ_2, λ_3 exceed the critical value with a range of 4.6~11 J/m^2 and the most dangerous position is the contact area between particles (Fig. 47). As mentioned before, the debonding of the core-shell structure is mainly caused by the severe Si core expansion so that the debonding ERR decreases with smaller Si proportion in the core-shell structure.

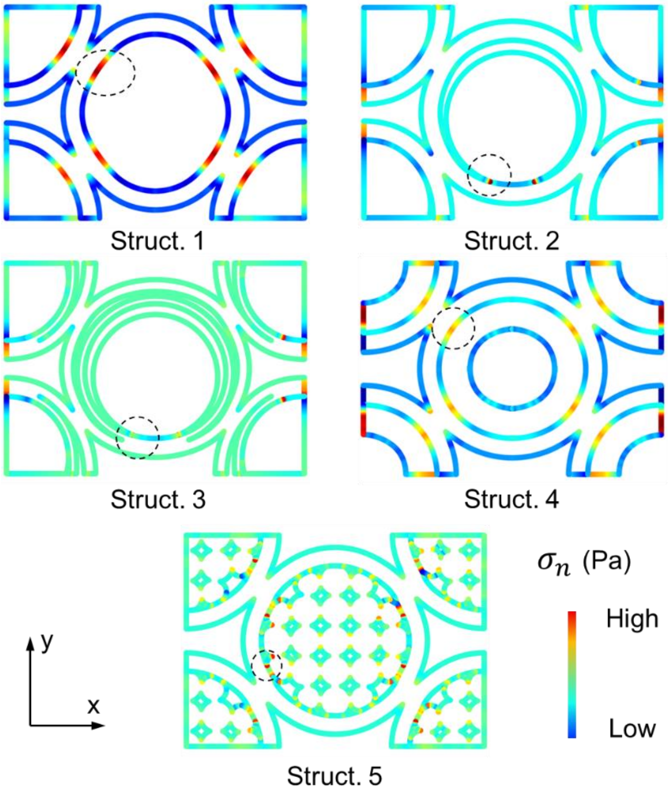

Figure 47 Normal stress distribution in Si/C interface of different structures. The place most likely to produce core-shell debonding is marked by the dashed circle.

4.2.4 Electrochemical behavior

According to the diffusion theory discussed above, it is rational that Li^+ diffuses into the C shell first and then alloys with Si core during the lithiation process (Fig. 48a). However, the Li^+ concentration distributions in both Si core and C shell are not uniform. Fig. 48b demonstrates that the concentration gradient is highly related to stress status due to the stress driving Li^+ diffusion mechanism. Li^+ is prone to be attracted by tensile stress,[5] such as to leave a Li^+ insufficient area within the largest compressive stress zone in the contact position between C shells (Fig. 48b). The Li^+ concentration near the Si/C interface is more significant since the compressive stress is smaller compared to the center of the contact area. Thus, a larger Li^+ concentration can be found in the same position in the Si core because the Li diffusion in Si core is dominated by the potential at the Si/C interface. Li^+ concentrations at four time points (t_1~t_4) retain the same distribution tendency (Fig. 48b). Therefore, results demonstrate that the Li^+ diffusion is driven by the combination of concentration gradient, stress gradient, and OCP of materials in Si/C core-shell structures.

The theoretical specific capacity of active material is linearly related to the Li^+ concentration.[144] Thus, the Li^+ concentration is used to determine the capacity performance of the studied structures with some variables defined here for better understanding. The theoretical Li^+ concentration c_{theo} at a certain state of charge (SOC) value for the anode representative volume element (RVE) lithiated from SOC = 0 can be written as Equation (47):

$$c_{\text{theo}} = \frac{Ct_{\text{charging}}}{t}\left(\frac{V_{Si}c_{s,Si}^{\max} + V_C c_{s,C}^{\max}}{V_{RVE}}\right). \tag{47}$$

where t = 3600 s. When the RVE is fully lithiated, $Ct_{\text{charging}} / t = 1$, the term $(V_{Si}c_{s,Si}^{\max} + V_C c_{s,C}^{\max}) / V_{RVE}$ represents the maximum Li^+ concentration within the RVE. The actual Li^+ concentration c_{act} at the same SOC can be calculated by Equation (48):

$$c_{\text{act}} = \frac{V_{Si}c_{s,Si} + V_C c_{s,C}}{V_{RVE}}, \tag{48}$$

where the $c_{s,Si}$ and $c_{s,C}$ are the Li^+ concentration in Si core and C shell from the simulation, respectively. These two variables for the same model should be the same if all the active materials in the anode can be fully used. However, the modeling results show that the c_{act} cannot reach c_{theo} due to the electro-chemo-mechanical coupling effects, which means only partial active materials are used. Thus, the ratio $c_{\text{nom}} = c_{\text{act}} / c_{\text{theo}}$ (0~1), which is called the normalized capacity, can describe the percentage of active materials that can be effectively utilized for Li^+ storage. As Fig. 48(c) shows, the C_{nom} of core-shell structure with λ_1 exhibits a peak value of 0.713, which means about 70% capacity is achieved. This further demonstrates that the structural effects influence the capacity performance due to the multiphysics coupling control mechanism (see the *Method* section for more details).

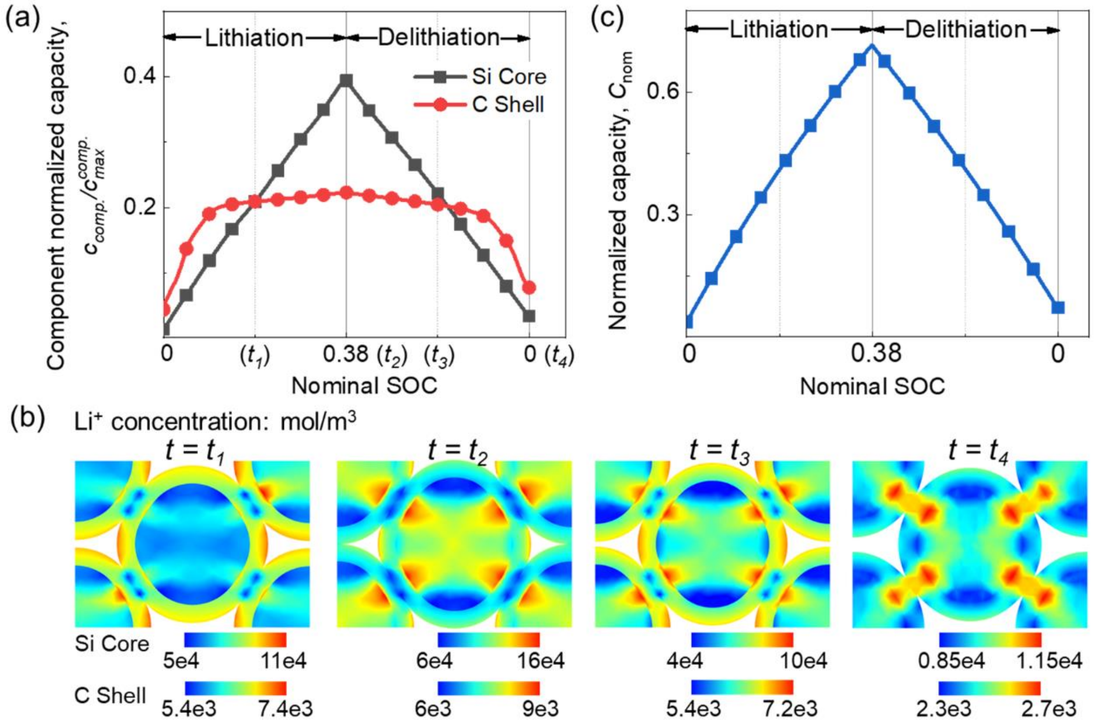

Figure 48 Simulation results of a core-shell structure (Structure 1) during lithiation-delithiation cycling. (a) Specific Li$^+$ concentration (actual Li$^+$ concentration divided by the maximum Li$^+$ concentration of component Si and C, respectively) profile. (b) Li$^+$ concentration contour plots during lithiation (t_1), at the end of lithiation (t_2), during delithiation (t_3) and at the end of delithiation (t_4). (c) Active material utilization rate, R_m.

4.2.5 Behaviors in various structures

4.2.5.1 Mechanical behavior

Similar to modeling work for core-shell structure, governing parameters for mechanical failure (i.e., G_f and G_d) and electrochemical property (i.e., c_act) were calculated from the simulation results for the other four structures (Figs. 49–51). Then the peak values during the lithiation and de-lithiation cycle are summarized and plotted in Fig. 52 to compare the mechanical failure behavior among five representative structures with three configurations for each. (For specific values, see Table 6). The larger value of c_act here also represents a larger proportion of Si core in the RVE.

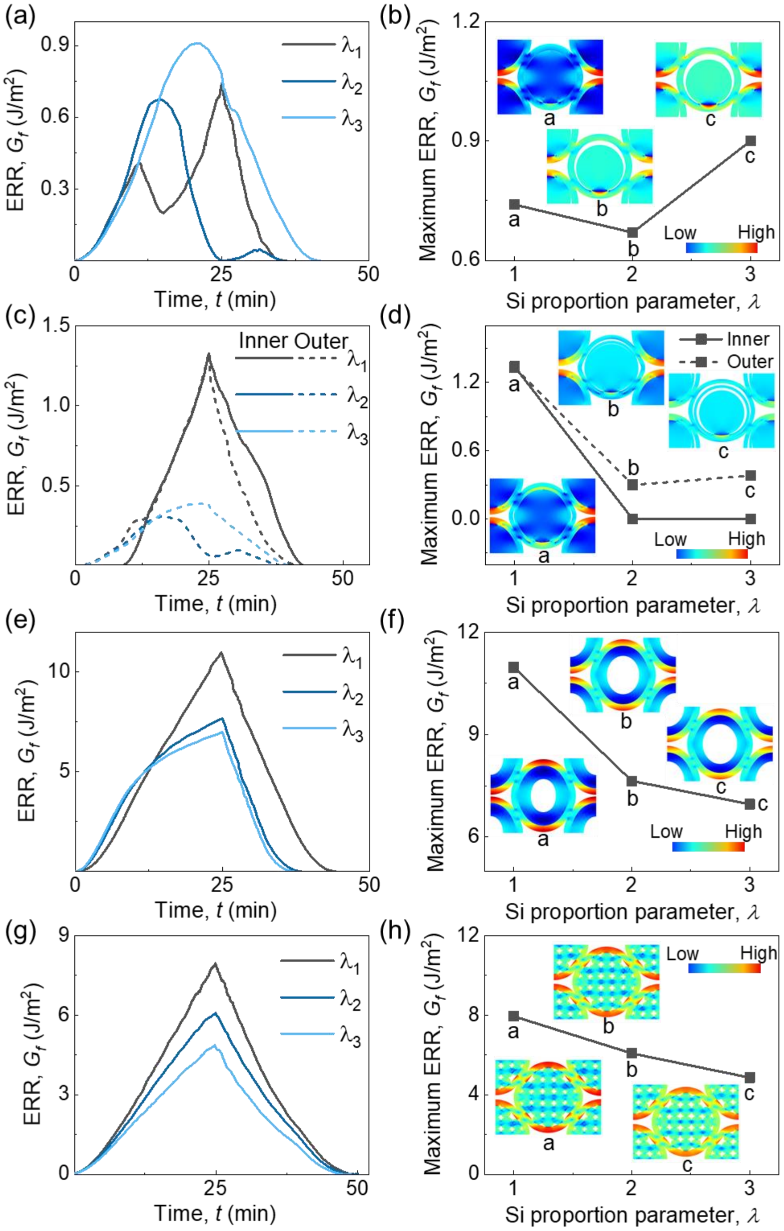

Figure 49 Different fracture FERR evolutions for (a) yolk-shell (Structure 2); (c) dual-shell (Structure 3); (e) hollow core-shell (Structure 4); and (g) multicore-shell (Structure 5) structure. Each structure has three different Si proportions represented by three λs. The corresponding peak values for each λ of four structures are plotted in panels (b), (d), (f), and (h) with insets of hoop stress distribution.

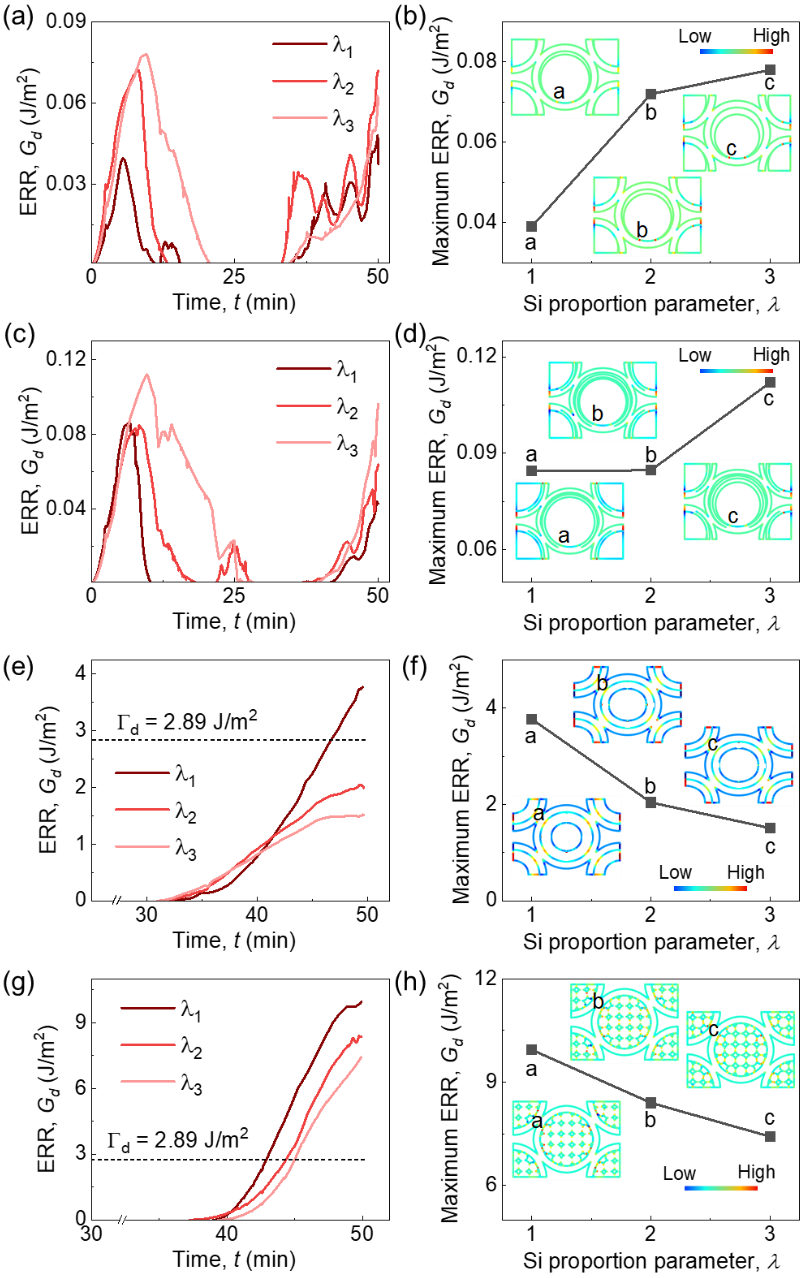

Figure 50 Different debonding ERR evolutions for (a) yolk-shell (Structure 2); (c) dual-shell (Structure 3); (e) hollow core-shell (Structure 4); and (g) multicore-shell (Structure 5) structures. Each structure has three different Si proportions represented by three λs. The corresponding peak values for each λ of four structures are illustrated in panels (b), (d), (f), and (h), with insets of normal stress distribution at the Si/C interface.

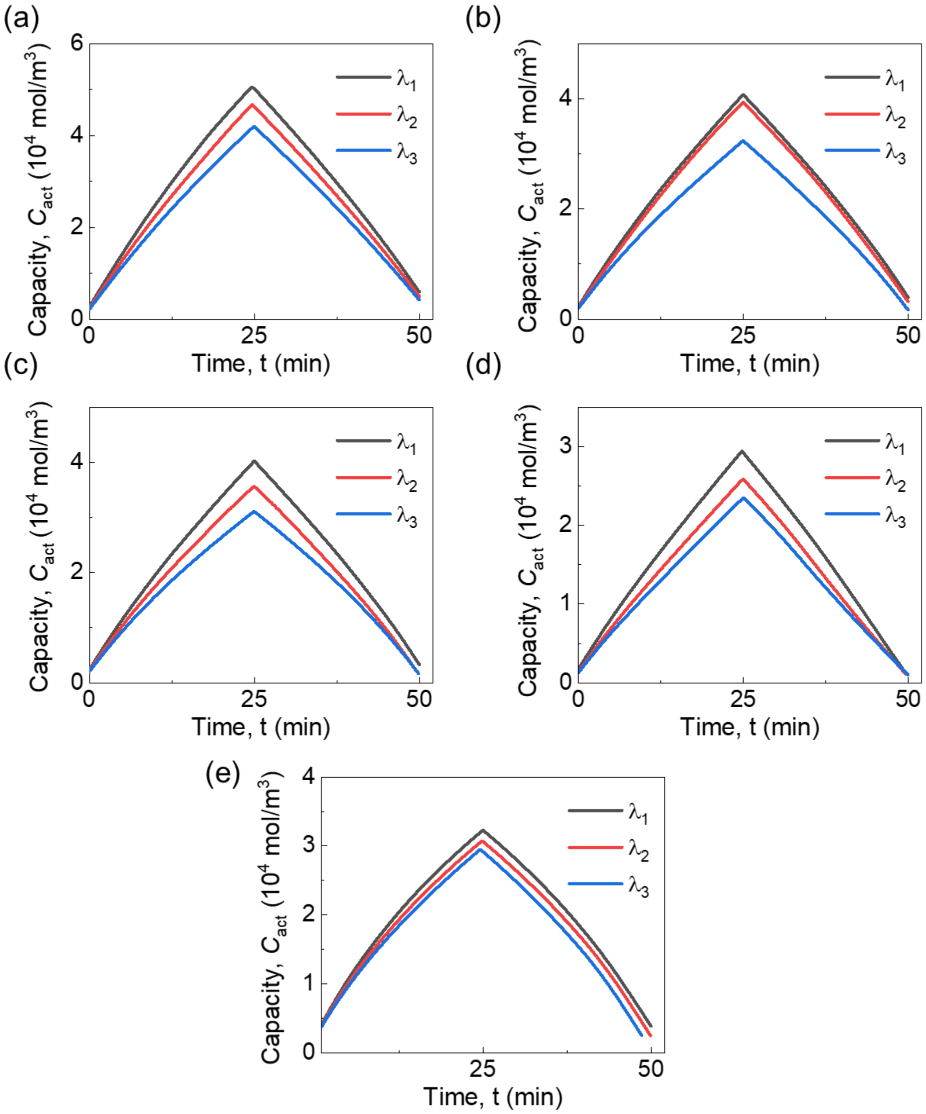

Figure 51 Li^+ concentration profile in charging/discharging processes of different structures: (a) core-shell (Structure 1); (b) yolk-shell (Structure 2); (c) dual-shell (Structure 3); (d) hollow core-shell (Structure 4); and (e) multicore-shell (Structure 5) structures.

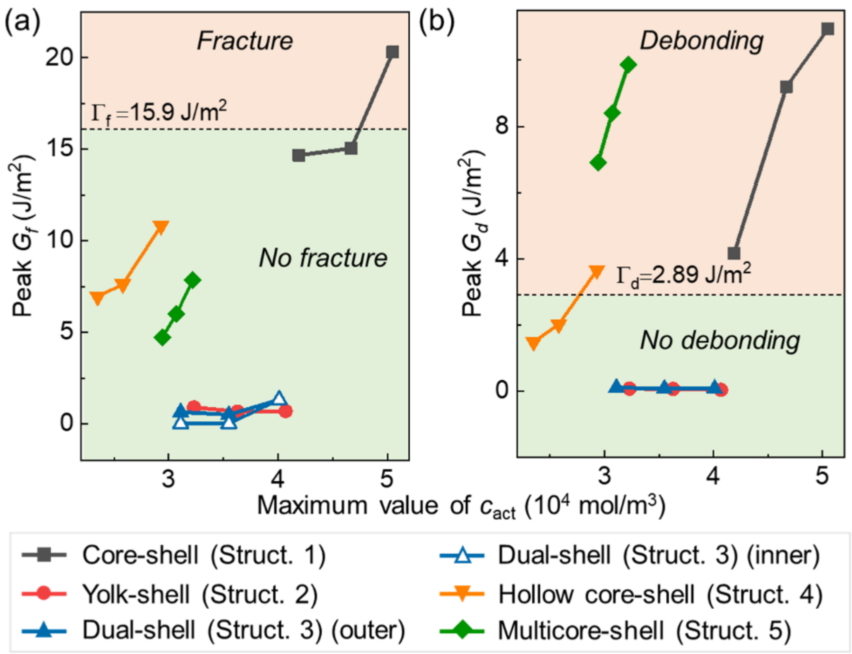

Figure 52 Relationship between the peak value of ERRs and maximum actual Li$^+$ concentration of all the five structures in terms of (a) shell fracture and (b) core-shell debonding

Shell fracture failure analysis

For Structures 1, 4, and 5, the peak G_f increases with increasing c_{act} (Fig. 52a), because a larger Si core proportion may directly lead to a more substantial swelling effect on the C shell, which further causes larger hoop stress. Among these three structures, the core-shell structure (Structure 1) with peak G_f ranging from 15~21 J/m^2 is the most vulnerable one for shell fracture, while the multicore-shell structure (Structure 5) with peak G_f ranging from 4.5~8 J/m^2 shows the lowest risk of shell fracture. Note that the inner void of the hollow core-shell structure (Structure 4) cannot provide the desired buffering effect (Fig. 46). This can be attributed to the low stiffness of C shell, which cannot limit the core expansion inward as much as expected. Thus, the mechanical property of shell material is also an essential factor for designing the structure.

For Structures 2 and 3, peak G_f is relatively small, since the voids in these two structures can allow the Si core to expand without producing high tensile hoop stresses in C shell until the core and shell are contacted. In addition, the peak G_f tendency was relatively flat among different λ values within the same structure, which is different from those in Structures 1, 4, and 5. This is mainly caused by the void in the yolk-shell structure, which tolerates the Si core expansion, and further ensures that the stress generated in the shell is relatively small. Thus, the hoop stress in the C shell shows little difference among three different configurations until the Si core fully contacts the C shell. Specifically, for Structure 2, the structure with a smaller Si core (smaller c_{act}) causes relatively larger hoop stress (Fig. 52a). Hoop tensile stress at the beginning is mainly caused by the expansion of the initial connection area (Fig. 53). Then it decreases when the free outer surface of the Si core and inner surface of C shell begin to contact, producing counter stress. For a smaller core, which obviously has a larger curvature, it takes a longer time to contact the inner surface of the C shell, which leads to larger hoop stress. This tendency will change after the Si core contacts the C shell completely if the void is minimal. For Structure 3, we observe that the inner and outer structures of the C shell with the largest c_{act} have similar peak G_f of ~1.4 J/m^2, while the other two structures have no crack in the inner shell and relatively small G_f in the outer shell (Fig. 52a). The reason for this is that the larger Si core of configuration with λ_1 causes the contact between the inner shell and Si core, which produces the larger G_f and will further lead to the early fracture of the inner shell. In conclusion, no shell fracture would occur in Structures 2, 3, 4, and 5, among which Structures 2 and 3 are the most robust.

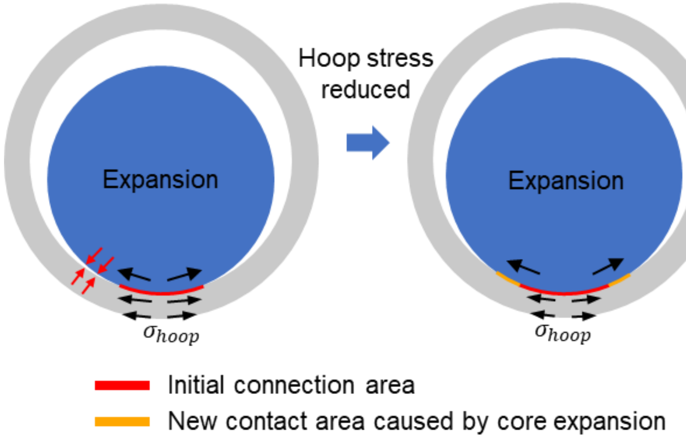

Figure 53 Hoop stress evolution coupled with the variation in contact area in yolk-shell structure.

Core-shell debonding failure analysis

Structures 1, 4, and 5 share similar evolution tendencies with larger peak G_d while Structures 2 and 3 have similar peak G_d evolution tendency with smaller values (Fig. 52b). For Structures 1, 4 and 5, peak G_d becomes larger due to the severe Si core expansion, which further leads to the permanent plastic shape change of the core. As mentioned before, the most dangerous position for debonding is the contact area of two particles where the permanent shape change is severe (Fig. 47). Similar to the shell fracture, the peak G_d increases with c_{act} in these three structures due to the increase of the volume expansion of the Si core. Again, the most vulnerable structure in terms of debonding is the core-shell structure. However, unlike for shell fracture, the hollow core-shell rather than the multicore-shell structure exhibits the lowest risk of debonding among the three structures.

For Structures 2 and 3, debonding mainly occurs along the border of the initial connection area of Si core and C shell (Figs. 47 and 50). The border of the interface is usually weak and serves as an initial crack. When it couples with the stress concentration, debonding may be triggered. The peak G_d values are minimal for these two structures (i.e., 0.04 J/m^2~0.12 J/m^2), and the tendency is flat for the same reason the void is able to mitigate the stress caused by Si core expansion until the Si core contacts the C shell. Note that there are two peaks in G_d; in other words, one is at the beginning of lithiation, and the other one is at the end of delithiation, (Figs. 50a and 50c). The first peak value caused by the initial expansion of the Si core decreases with Si proportion increasing, similar to the mechanism illustrated in Fig. 53. After reaching the peak value, it decreases when large areas of the Si core surface and the C shell inner surface begin to contact. This peak is trivial and far below the critical value of 2.89 J/m^2, which means the first peak can be ignored for debonding. Similar to Structures 1, 4, and 5, the second peak is caused by the permanent shape change of the Si core due to expansion and contraction. The second peak increases with the Si core proportion or the charging time (SOC), which may exceed the cracking threshold criteria to cause the debonding of these two structures. In conclusion, Structures 1, 4, and 5 all show core-shell debonding failure and Structures 2 and 3 are the most robust at resisting debonding.

4.2.5.2 Electrochemical analysis

The following analysis is based on the scenario that the C shell structure and the Si/C interface are in good condition without any cracks/fractures, and all the structures are cycled under the same loading conditions. As mentioned before, the Li^+ concentration can be used to discuss the volumetric specific capability since the volumes of all five structures are identical. It is clear that the c_{act} positively correlates with the Si proportion (Fig. 54a). Structure 1 possesses the largest c_{act} (4.19~5.05 × 10^4 mol/m^3), and Structure 4 has the smallest c_{act} (2.35~2.93 × 10^4 mol/m^3), while the other three structures show similar c_{act} values ranging from 3 to 4 × 10^4 mol/m^3 between Structures 1 and 4 due to the reason that the voids in the structures reduce the proportion of Si. Thus, increasing the Si core proportion can directly increase the volumetric specific capacity of the proposed structures.

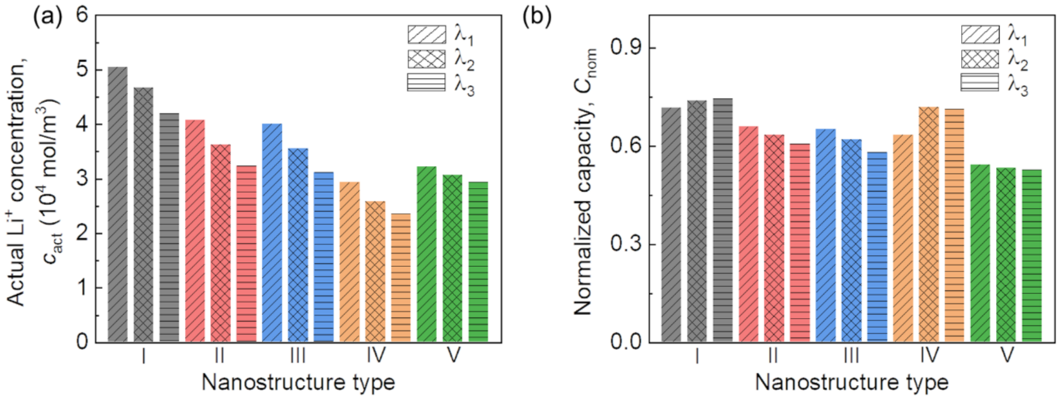

Figure 54 Electrochemical performance of five proposed structures in terms of (a) actual Li^+ concentration, which may represent the volumetric specific capacity; and (b) active material utilization rate, which represents the Li^+ diffusion capability**.**

However, relying solely on increasing the Si core proportion is not enough because the Li^+ diffusion is restricted by the structure. Thus, the normalized capacity, C_{nom}, should also be considered here. Structure 1 has the largest C_{nom}. Therefore, it can reach ~70% capacity since the core-shell structure has the largest Si/C interface, which allows more Li^+ to diffuse into the Si core simultaneously (Fig. 54b). In addition, Structure 1's smaller Si proportion demonstrates a better capacity performance. Structures 2 and 3 possess a similar C_{nom} of about 65%, which is relatively low compared to Structure 1. This small value of C_{nom} is mainly due to the relatively small area of the Si/C interface of these two structures compared to the core-shell structure. However, for Structures 2 and 3, when the Si proportion decreases, the ratio decreases as well, such that a larger Si proportion is more beneficial for the capacity performance of these two structures under the assumption of enough voids for Si core to expand. Structure 4 has the same Si/C interface area with Structure 1, but a relatively small C_{nom} value (~68%). Note that the Si core shapes of these two structures are different, although they share the same Si/C interface area. Here, the Si core of Structure 4 does not exhibit an inward expansion behavior, as expected, because its soft shell means that it cannot take advantage of the inner void to guarantee a better stress status. Thus, a solid core is better than a hollow core in terms of capacity performance if the hollow core cannot expand inward. Structure 5 possesses the smallest C_{nom} value of about 53%. This is not only due to the small area of Si/C interface, but also to the porous structure, which causes a relatively long path for Li^+ to diffuse into the Si cores. Thus, a more significant Si proportion can reduce the porosity, which further leads to a slightly higher C_{nom} value here for Structure 5.

In summary, Structure 1 behaves best in terms of both volumetric specific capacity and normalized capacity performance. Structures 2 and 3, with an appropriately high Si proportion, can provide relatively satisfactory capacity performance. However, Structures 4 and 5 are not as competitive as the other three structures in terms of electrochemical properties.

4.2.6 Design map of Si/C nano-structure selection for battery anode

When the Si/C composite is further lithiated, shell fracture and core-shell debonding will occur, and its effect on the electrochemical performance of Si/C composite worth investigating. Because the radius-thickness ratio is $r/t > 5$, we look at the shell fracture without consideration of the crack length (in other words, the shell is thin enough to neglect the thickness). However, the circumferential length of the C shell is non-trivial, and we need to consider the crack length for its debonding scenarios. The degree of debonding also interacts with the Li$^+$ diffusion behavior and further impacts the volumetric capacity. Therefore, we couple G_d and C_{nom} into a new factor as Equation (49):

$$C_{\mathrm{nom}}^{d} = C_{\mathrm{nom}} \cdot (1-\chi), \tag{49}$$

where $\chi = A_{\mathrm{debonding}} / A_{\mathrm{initial}}$ is the debonding ratio defined as the debonding area $A_{\mathrm{debonding}}$ divided by the initial interface area A_{initial} (see Fig. 55). This factor can describe the capacity performance with consideration of core-shell debonding failure and Li$^+$ diffusion. Then, we propose a design map with the two governing factors, G_f and C_{nom}^{d}, beyond which the maximum c_{act} is also indicated on the map as the third design factor (Fig. 56). All the structures located in the zone with *x*-axis values smaller than 15.9 are theoretically crack-proof for shell fracture. A larger *y*-axis value would improve performance on Li^+ diffusion. Thus, the structure located in the top left corner should be the target. Intuitively, such structures with a larger c_{act} should be considered preferentially, which may ensure a larger volumetric specific capacity for the anode.

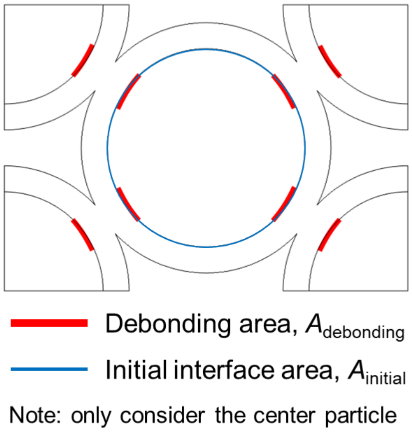

Figure 55 Debonding area and initial interface area of the core-shell structure.

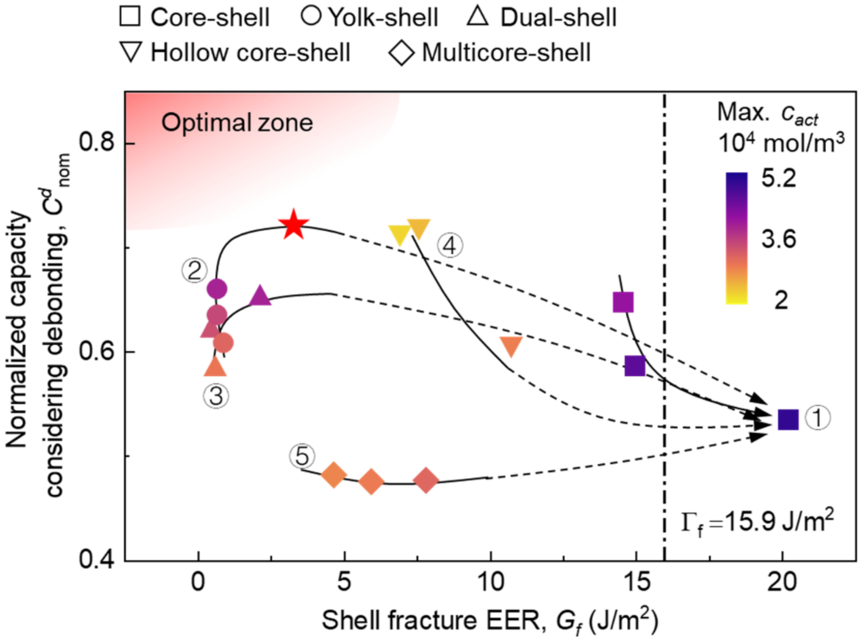

Figure 56 Si/C composite nanostructure design map considering shell fracture resistance

properties, core-shell debonding related to capacity performance. Note that arrows refer to the predictive design paths of different structures targeting the optimal one by increasing the Si core proportion (for Structures 2, 3, 4 and 5, the shell thickness is assumed to remain unchanged). The red star denotes the optimal design based on five basic structures. Inset numbers represent the structure number as well as the predictive design path number. By tuning the geometric parameters, all structures can be finally degraded back the basic core-shell structure.

In particular, the multicore-shell structure (Structure 5) exhibits good robustness in terms of shell fracture, but inferior capacity performance, which is not the desired design. The other four structures show excellent performance in terms of C_{nom}^{d}, which are optimal design in terms of the capacity fade of anode due to the particle crack. Among them, the yolk-shell structure (Structure 2) shows the smallest G_f and largest C_{nom}^{d} when possessing the same maximum c_{act} with the other three structures, such that yolk-shell is an optimal choice. Therefore, the yolk-shell structure is the most feasible structure among these five representative nanostructures.

We can observe the proposed five predictive design paths to gain better performance by consideration of mechanical robustness and capacity performance (Fig. 56). The design guidance can be summarized as: 1) all the structures should locate in the left zone to the critical line G_f = 15.9 J/m^2; 2) based on 1), the structure with larger C_{nom}^{d} should be selected; and 3) c_{act} should be as large as possible. The design map implies that Path 2 is the optimal one, which ensures a structure with better performance of capacity (both the volumetric specific capacity and the Li$^+$ diffusion), meanwhile showing the lowest risk for shell fracture. Thus, the yolk-shell structure still performs best when seeking for the optimal configuration.

4.2.7 Conclusions

An electrochemical-mechanical coupling theoretical model was established and further developed and implemented to describe the multiphysics behaviors of Si/C composite nanostructures. Five representative Si/C composite nanostructures (i.e., core-shell, yolk-shell, dual-shell, hollow core-shell, and multicore-shell) were selected and studied using the proposed generalized model. Different Si proportions for each nanostructure were considered here. Two major mechanical failure modes for Si/C composite particles (i.e., shell fracture and core-shell debonding) and the capacity performance were discussed. The following conclusions can be drawn:

- The yolk-shell and dual-shell structures are more crack-resistant than the other three structures for both failure modes. In addition, the high Si proportion for these two structures is beneficial for improving the mechanical performance under the assumption that the void is enough for Si core to expand.
- In terms of electrochemical properties, yolk-shell and dual-shell exhibit good performance compared to the others.
- A design map was established to systematically reveal the structure-properties relations and comparisons for core-shell-related nanostructure designs.

Results provide a generalized modeling framework to describe various Si/C composite nanostructures and fundamental guidelines for fabrication and engineering next-generation Si/C composite particles for anode with high energy density and crack-proof design.

CHAPTER 5 MULTISCALE-MULTIPHYSICS MODELING FROM PARTICLES TO ANODE

In this chapter, we established a modeling framework aiming at Si-C composite anode. Half-cell tests were conducted to capture the electrochemical property of the target material. An *in-situ* full-cell charging/discharging test was conducted to provide the voltage and deformation profiles. A multiphysics-multiscale model for composite anode was then established based on the classical mechanical and pseudo electrochemical model and was validated by the testing data. Based on this model, two cases with different geometrical configurations to achieve different Si ratios were studied, as well as the constraint effect and charging rate effect. Electrochemical properties such as voltage profile and Li-ion concentration, together with mechanical behaviors such as stress and deformation, will be discussed for all cases to determine a better configuration for high capacity LIB.

5.1 Method

5.1.1 Si/C composite anode multiscale characterization

Without loss of generality, two types of Si-C compound particles with different Si proportions, i.e.20 wt%, and 40 wt%, were selected in this study for Case I and Case II, and the physical properties are listed in Table 7. The Si-C compound particles were used to fabricate the composite anode (Fig. 57(a)). The active particle, binder, and conductive agent were mixed with a ratio of 95:1:4 (see Table 7). Then, a classic slurry cast (coating – drying – rolling – assembly) technique was used to get the composite anode. The multiscale structure of Si-C composite anode can be seen in the scanning electron microscope (SEM) images (Figs. 57 (a)-(d)). The active materials of the composite anode (Fig. 57 (a)) is composed of graphite particles (dark part) and Si-C compound particles (bright part), which is fabricated using nano Si particles, graphite particles and amorphous carbon (Fig. 57 (b)). The nano Si particles, graphite particles and amorphous carbon are purchased from BTR New Energy Materials Inc. The cross-sectional SEM images (Fig. 57 (c) and (d)) show that graphite particles (~2 um) serve as the skeleton on which the nano Si particles (~100 nm) are attached by adhesive amorphous C in Si-C compound particles. The capacity could achieve around 800 mAh/g and 1200 mAh/g, i.e., more than 2 and 3 times of the theoretical capacity of pure graphite particles, respectively.

Then, the composite anode with 15wt% Si-C compound particles in Case I (the baseline) was used to fabricate half-cell and full-cell for the following tests; the details can be found in Table 8. The cathode used for half-cell is Li metal (purchased from Tianjin Zhongneng), while the $LiCoO_2$ (LCO, purchased from Hunnan Shanshan with the loading of 23.4 mg/cm^2) was selected for full-cell. The electrolyte used here was LiPF6 with EC: DMC = 1:1 which was excess, and the excess was squeezed out during the package. The final quantity of the electrolyte used in this study was 1.6-1.7g/Ah.

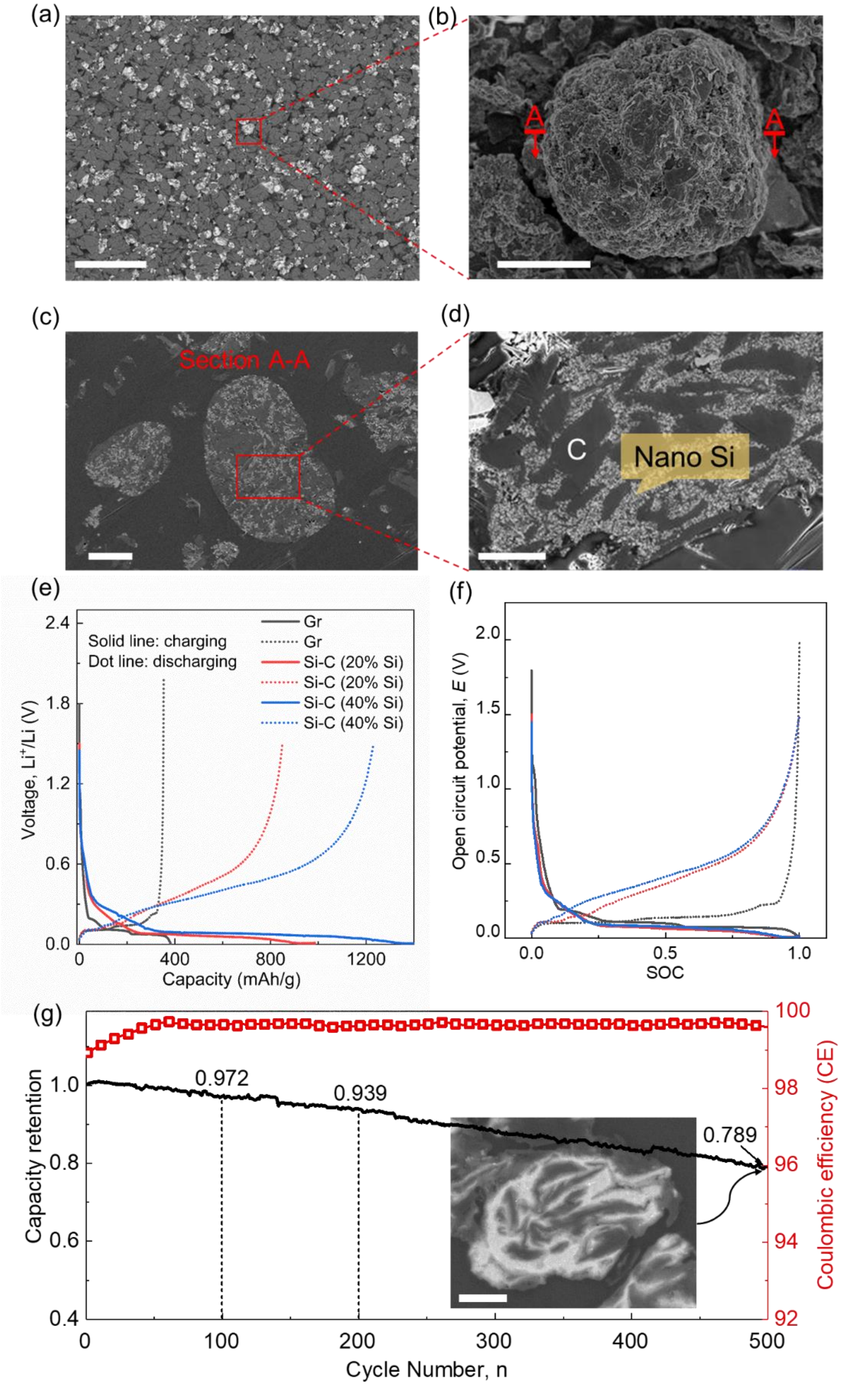

Figure 57 SEM pictures of Si-C composite anode material and the electrochemical

characterization. SEM images of (a) Si-C composite anode (dark zone is C particles and bright particle is Si-C compound particle); (b) Si-C compound particle; (c) cross-section (section A-A) view of Si-C compound particle; (d) nano Si and C particle distribution within Si-C compound particle; (e) half-cell testing for pure graphite anode material and Si-C compound particle material with different Si proportions (20 wt% and 40 wt%); (f) the OCP curves used for modeling corresponding to (e) by change the x-axis to SOC (SOC equals to capacity divided by the corresponding maximum value); (g) Full cell capacity retention at each cycle for 500th cycle. The CE is plotted on the secondary y-axis. Inset: SEM images of Si-C compound particle after 500 cycles. Scale bars shown in (a)-(d) and (g) are 5 μm .

Table 7 Physical properties of two types of Si-C composite anode

	Si-C comp, wt.%	Si wt.% in Si-C comp	Si wt. %	Graphite, wt.%	Carbon Black, wt.%	Binder, wt.%	Loading, mg/cm^2
Case I	11.25	20%	2.25%	92.75%	1%	4%	\
	15	20%	3%	92%	1%	4%	8
	18.75	20%	3.75%	91.25%	1%	4%	\
Case II	15	20%	3%	92%	1%	4%	8
	15	40%	6%	89%	1%	4%	\

Table 8 parameters of half-cell and full-cell used for testing

	type	Size, mm	Anode thickness, um	Cathode thickness, um	Energy density, Wh/kg
Half-cell	Coin cell	13 (radius)	90-110	500	/
Full-cell	One layer	83*61*0.1	44	47	
Full-cell	Pouch cell	73*60*3.88	90-110	100-120	750

5.1.2 Electrochemical characterization of compound particles

A half-cell test was constructed on the Si-C composite anode material on the testing system LAND CT2001H. The voltage profiles as a function of the reversible capacities of two types of Si-C compound particles and the pure graphite particles were measured by the constant current and constant voltage techniques with a rate of 0.1C, from 0.005 V to 1.5V (for Si-C compound particles) and 1.8V (for graphite particles). Only the results of the first cycle were measured here. The compound particles with 20% wt Si and 40 wt% Si and the graphite particles exhibited first-cycle gravimetric reversible capacities of 850 mAh/g, 1230 mAh/g, and 353 mAh/g, respectively, with initial Coulombic efficiencies (CEs) of 86.3%, 86.3%, and 92.4%, respectively (Fig. 57 (e)). The curves obtained from the half-cell test are adopted to be the input open circuit potential (OCP) data since the applied current in this test is very tiny. It can be applied as the anode material properties in the following modeling works (Fig. 57(f))

Also, a one-layer full-cell containing one layer of Si-C composite anode, one layer of the separator, and one layer of LCO cathode were tested *in situ*. The full-cell configuration was placed in an optical high-power microscope to obtain the real-time deformation video during charging/discharging. At the same time, it was connected to the charging machine and was charged/discharged by the following strategy: CC charging with a rate of 0.5 C to 4.4V and then convert into CV charging until rate gets down to 0.025C; rest 15 minutes; CC discharging with a rate of 0.5 C to 2.75V; stop. The voltage profiles were recorded. Then the images at different time points were extracted and analyzed to get the deformation values. So, the voltage and deformation were obtained simultaneously in the test and used to validate the computational model.

Cycling tests after the first cycle of the full cell shown in Table 8 were also performed in the voltage range between 2.5V and 4.4 V at 1C on testing system LAND CT2001H. As shown in Fig. 57 (g), the composite anode can keep 97.2% reversible capacity after 100 cycles, 93.9% after 200 cycles and 78.9% after 500 cycles, which is comparable to the current commercial ones. For the CE, it can reach 99.5% after about 37 cycles. This may be explained by the SEM image of Si-C compound particle after 500 cycles that the nano Si exhibited irreversible swelling which may cause severe stress conditions and further lead to fracture and capacity degradation. Thus, the simulation work in the following parts may provide an excellent way to elaborate on the mechanism. Further studies will be conducted in the future besides the multiscale modeling in the current study.

5.1.3 Multiphysics-multiscale computational methodology

The left part of Fig. 58 shows a 3D multiscale structure of the Si-C composite anode (one unit layer with a structure of anode active material-anode current collector-anode active material-separator-cathode active material-cathode current collector-cathode active material). The binder and additives are not considered here, and the Si-C compound particles are simplified as a homogenous particle (Fig. 59). The detailed method of homogenization can be seen in Appendix D. To further simplify the modeling process, 2D representative volume element (RVE) model in macroscale (both for mechanical and electrochemical sections) considering only one layer of anode active material, separator and one layer of cathode active material were established where the anode active material was divided into two parts, i.e. C zone and Si-C zone (mid part of Fig. 58). C zone represented the graphite particles which were in dominant quantity, while Si-C zone represented the converged Si-C compound particles. Considering the proper simplification (1D simplification in the right part of Fig. 58) of the particle shape, several trial simulation works (Appendix E) indicate us to choose four grey circles in 2D model to represent the dispersed Si-C particles by setting the overall weight percentage same as baseline. Then in microscale, single-particle for pure graphite and Si-C particle were simplified into 1D problem and considered by extra dimension node method.

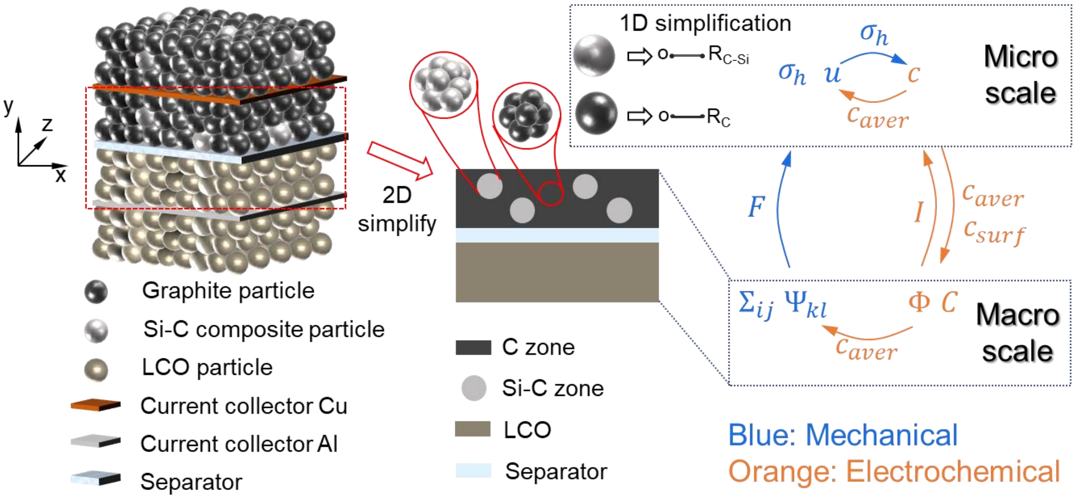

Figure 58 Multiphysics-multiscale modeling methodology with the coupling strategy

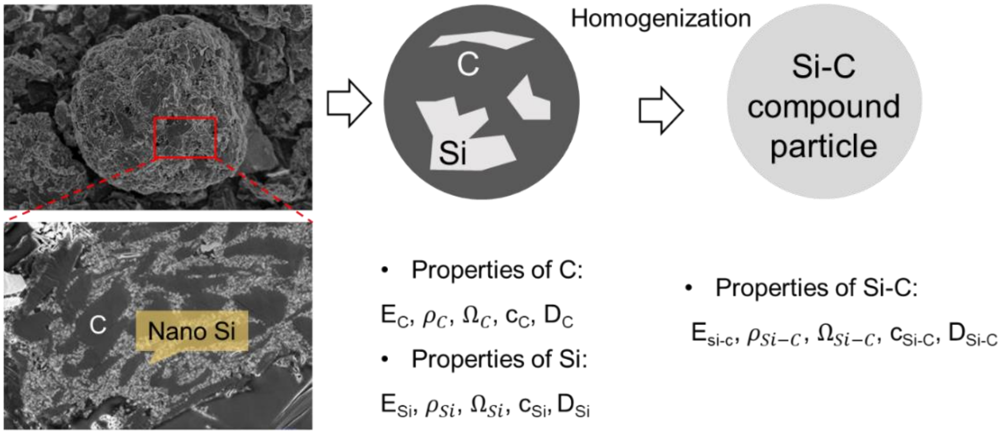

Figure 59 Schematic of the homogenization of Si-C compound particles

The coupling strategy of field variables is also illustrated in Fig. 58. There are two types of couplings: multiphysics and multiscale. In multiphysics coupling at the microscale level, the average Li-ion concentration (c_{aver}) in C particle and Si-C particle increases with the charging process (governed by electrochemical model), leading to the swelling behavior of C and Si-C particles (governed by mechanical model). In return, hydrostatic stress (σ_h) derived from the swelling of two kinds of particles (mechanical model) affects the Li-ion diffusion (electrochemical model). Similarly, the multiphysics coupling at macroscale happens between the average Li-ion concentration (c_{aver}) change within C zone and Si-C zone (electrochemical model) and its induced eigen strain (Ψ_{ij}) change (mechanical model).

In the multiscale coupling of the electrochemical model, the intercalation reaction current density (*I*) in macroscale for C zone and Si-C zone that dominates the Li flux on corresponding particle surfaces in microscale would be passed from macroscale to microscale while on the contrary, the surface Li-ion concentration ($c_{s,surf}$) in micro C and Si-C particles that determine the potential of C zone and Si-C zone in macro scale, respectively, would be passed from microscale to macroscale. While in the multiscale coupling of the mechanical model, only the deformation gradient (*F*) would be passed from macroscale to microscale to determine the local deformation. This coupling strategy showed in Fig. 58 can simultaneously achieve multiphysics-multiscale modeling of the composite anode in single-layer Li-ion cells. The principal governing equations are shown in the following sections, while the detailed descriptions can be found in Appendix F.

a) Mechanical model in microscale

For spherical particle, the typical equilibrium equation can be described as

$$\frac{\mathrm{d}\sigma_{rr}}{\mathrm{d}r}+\frac{2}{r}\left(\sigma_{rr}-\sigma_{\theta\theta}\right)=0 \tag{50}$$

In the current study, hydrostatic stress was considered on the surface of particles to represent the effects of surrounding particles, under which the particle would not turn into a plastic stage. Thus, only elastic behaviors are considered here, and the constitutive equation could be derived as

$$\sigma_{ij}=2G\varepsilon_{ij}+\xi\varepsilon_{kk}\delta_{ij}-\Omega_{eff}\Delta c_s\frac{E}{1-2\upsilon}\delta_{ij} \tag{51}$$

where $\Delta c_s=c_s-c_s^0$. Different material properties would be applied for C particle and Si-C particle (subscript or superscript "C" and "Si-C" to represent parameters for C particle and Si-C particle, respectively). The boundary conditions could be

$$\begin{aligned} u_{r,\mathrm{C}}&=0 \text{ at } r_{\mathrm{C}}=0\\ u_{r,\text{Si-C}}&=0 \text{ at } r_{\text{Si-C}}=0 \end{aligned} \tag{52}$$

$$\begin{aligned} u_{r,\mathrm{C}}&=\left(\sqrt[3]{\det\mathbf{F}}-1\right)r_{p,\mathrm{C}} \text{ at } r_{\mathrm{C}}=r_{p,\mathrm{C}}\\ u_{r,\mathrm{Si-C}}&=\left(\sqrt[3]{\det\mathbf{F}}-1\right)r_{p,\mathrm{Si-C}} \text{ at } r_{\mathrm{C}}=r_{p,\mathrm{Si-C}} \end{aligned} \tag{53}$$

b) Electrochemical model in microscale

The composite anode contains two kinds of particles in the microscale. Similar to the mechanical model, variables like Li-ion concentration, c_s, should have two substances that are $c_{s,\mathrm{C}}$ and $c_{s,\mathrm{Si-C}}$. To make the description concise, specific substances are not shown here.

Governing equation of Li-ion diffusion within a particle is described by Fick's law as Eq. (16) shows [145-146]

The microscale behaviors are achieved by the extra dimension nodes method here. The basic principle is: extra dimension nodes are defined by each macroscale node which can carry all the variables from the macro electrochemical and mechanical model and is governed by Eq. (16). This method is implemented in COMSOL Multiphysics by weak form equations. Then the weak form of Eq. (16) can be expressed as follows by introducing a test function $\hat{c}_s$:

$$\int_r \left(\frac{\partial c_s}{\partial t} + \frac{1}{r^2} \frac{\partial r^2 J_s}{\partial r} \right) \hat{c}_s \mathrm{d}r = 0 \tag{54}$$

The boundary conditions and initial conditions are

$$\frac{\partial c_s}{\partial r} = 0 \text{ at } r = 0 \tag{55}$$

$$J_s = \frac{I}{F} \text{ at } r = r_p \tag{56}$$

$$c_s(r) = c_s^0 \text{ at } t = 0 \text{ s} \tag{57}$$

As described before, intercalation reaction current density, *I*, is passed from the macroscale electrochemical model.

c) Mechanical model in macroscale

The macroscale stress in the composite anode for either C zone or Si-C zone is given by (similarly, substances are not showed here)

$$\Sigma_{ij} = C_{ijkl}(\Psi_{kl} - \Psi_{eigen}\delta_{kl}) \tag{58}$$

The eigen strain of the macroscale materials here, $\Psi_{eigen}\delta_{kl}$, is determined by the volumetric change caused by the Li-ion intercalation/deintercalation of its microscale particles. Ψ_{eigen} is determined by the average Li-ion concentration within the materials, giving

$$\Psi_{eigen} = \frac{\Omega_{eff}}{3} \Delta c_s \tag{59}$$

The equilibrium of macroscale stress gives

$$\nabla \cdot \mathbf{\Sigma} = 0 \tag{60}$$

d) Electrochemical model in macroscale

Porous electrode theory[147] is used to describe the electrochemical behavior of the macroscale, as shown in Eqs. (9)-(14) in *Section 3.1.2*.

To make this model more functional and suitable for future aging studies, the formation of the SEI layer is also involved in this computational framework, as Eq. (15) shows. However, the SEI behavior is mainly dominant in cycling conditions so it is not discussed in the present work.

The computational framework mentioned above was then implemented into COMSOL Multiphysics 5.3a platform. A Dell Precision 7820 Tower workstation with 16 CUPs and 3.49 GHz was used.

5.1.4 Model settings and validation

To demonstrate the multiphysics-multiscale methodology described in *Section 5.1.3*, as mentioned above, a baseline configuration of Case I was established with four circles of Si-C zones of which the Si proportion in corresponding micro Si-C particle is 20 wt% (Fig. 60 (a)). For mechanical boundary conditions, the bottom surface of cathode was fixed while the top surface of the anode was set to be free. Given that the in-plane deformation in anode could be ignored compared with deformation in the thickness direction, symmetrical boundary conditions were applied on both side edges of the RVE model. For electrical boundary conditions, the cathode surface was connected to the ground while a constant current density was applied on the anode surface. The OCP curves used to define the potential of electrodes were from the half-cell test (Fig. 58(e)). All the other parameter values both for the electrochemical model and mechanical model can be found in Table 9. Considering the deformation of the cathode (material $LiCoO_2$ (LCO) was used in this study) during cycling are not evident compared to the Si-C composite anode, no multiphysics and multiscale coupling were applied on the cathode. The deformation of the cathode will cause mechanical loading on the anode which may lead to a condition similar to the mechanical constraint boundary. Thus, an analogy can be drawn between the effect of cathode deformation and the effects of mechanical constraint. This model was validated by comparing the results with full-test data.

Table 9 Input parameters in multiphysics-multiscale model

Parameter	Symbol	Value
Microscale		
Partial molar volume of Si[121]	Ω_{Si}	9×10^{-6} m^3/mol
Partial molar volume of C[134]	Ω_C	3.17×10^{-6} m^3/mol
Modulus of Si[122]	E_{Si}	$E_{Si}(c_{s,Si})$
Modulus of C[134]	E_C	$19.25+82.23x$ GPa
Maximum Li concentration in Si[119]	$c_{s,\max}^{Si}$	278000 mol/m^3
Maximum Li concentration in C[135]	$c_{s,\max}^{C}$	31507 mol/m^3

The diffusion coefficient in Si[121]	D_{Si}	$1.67\times10^{-14}\ \text{m}^2/\text{s}$
The diffusion coefficient in C[136]	D_C	$1\times10^{-9}\ \text{m}^2/\text{s}$
The radius of Si-C and C	r_p	5 μm (estimated)
Macroscale		
Anode thickness	H_{anode}	44 μm (measured)
Cathode thickness	$H_{cathode}$	47 μm (measured)
Separator thickness	$H_{separator}$	9 μm (measured)
RVE width of the cell	W	200 μm (estimated)
The volume fraction of solid in electrode	ε_s	0.4 (estimated)
Volume fraction of electrolyte in electrode	ε_e	0.4 (estimated)
The electrical conductivity of cathode [118]	$\kappa_s^{cathode}$	100 S/m
The electrical conductivity of anode [119]	κ_s^{anode}	1 S/m
Initial Li-ion concentration in electrolyte [120]	C_e^0	1000 mol/m^3
Diffusion coefficient in electrolyte [51]	D_e	$7.5\times10^{-11}\ \text{m}^2/\text{s}$
Transference number [120]	t_+	0.363
Transfer coefficient	$\alpha_a \quad \alpha_c$	0.5 (estimated)

As shown by the comparison of normalized capacity profiles (Fig. 60 (b)), simulation results well predict the test data within a voltage range of 2.8-4.44V. Average deformations during the charging process for both test and simulation are also compared (Fig. 60 (c)), giving that they are well consistent with each other despite a small deviation of 3%. It also indicates that the volume increase of a Si-C composite anode during charging can reach about 17% which is acceptable for commercial application compared to several reported Si-involved anode materials[10], although it is still a main defect of this kind of materials. The results shown in Fig. 60 (b) and (c) indicate that the computational model established in this study can accurately predict the electrochemical-mechanical coupling behavior of

Li-ion battery cell containing Si-C composite anode and can be used for parametric studies.

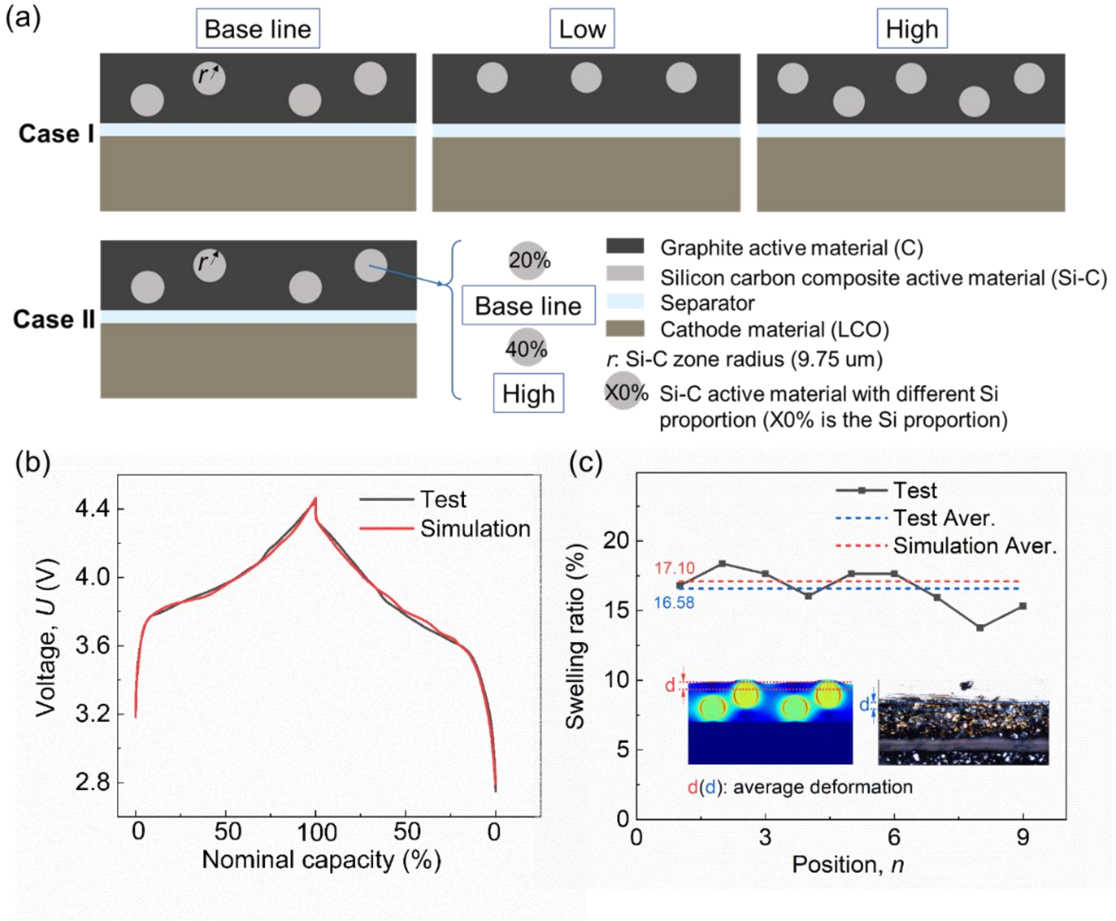

Figure 60 Model configuration and validation. (a) parametric study outline for Case I (different wt% of Si-C compound particle with same Si proportion) and Case II (same wt% of Si-C compound particles with different Si proportions); (b) and (c) model validation (Case I baseline) in respect to voltage and mechanical deformation, respectively.

5.2 Parametric studies

To further understand the composite anode multiphysics-multiscale mechanism and explore a better configuration aiming for application, a series of parametric studies using this validated model was carried out and analyzed in the following sections.

Basically, there are two types of Cases (Fig. 60(a) and Table 7). Case I and II consider different Si percentages in two different ways: Case I-- different amounts of Si-C zones with same Si proportion in micro particles (20 wt%) are set in anode which gives around 3 wt%, 2.25 wt% and 3.75 wt% overall Si percentages for baseline, Low and High case, respectively; Case II-- same amount of Si-C zones with different Si proportions in microparticles of 20 wt% and 40 wt% are set in anode which give around 3 wt% and 6 wt% overall Si percentages for Baseline and High case, respectively. Besides the Si percentage, constraint effect and charging rate effect are also considered in this study. Except for the parameters described above, all the other settings are the same, including initial conditions and boundary conditions.

5.2.1 Electrochemical behavior for Case I and Case II with and without constraint

Although the Si proportion was changed for different cases, the thickness of anode and cathode are kept unchanged and the same current density value (10 A/m^2 which leads to 0.5C for baseline) was applied for all cases in this part. As shown by the charging and discharging profiles of all cases (Fig. 61 (a) and Fig. 62), a very small difference can be seen in the charging process both for Case I and Case II. However, an obvious difference can be seen from the discharging process for Case II where cell with 40 wt% Si shows a faster voltage drop. This lower voltage profile of the full cell with 40 wt.% Si is due to the higher discharge voltage (delithiation) of the Si-C electrode as shown in Fig. 58 (f). Also, the Li-ion concentration profiles (Fig. 61 (b)) can provide a better understanding of this. A similar tendency can be seen in Fig. 61 (b) among different cases that Li-ion concentration in C zone increases smoothly until reaches its maximum value, while Li-ion concentration in Si-C zones increase faster initially and slow down to a platform, then sharply increase towards its maximum value at the end of charging process. During the discharging process, Li-ion concentration in C zone decreases continuously till it reaches zero at 4000 seconds (about 2/3rd of discharge). On the other hand, Li-ion concentration in the Si-C zone keeps almost unchanged at the beginning and starts to decrease when Li-ion concentration in the C zone is almost zero. Such computational results have good qualitative consistency with the experimental results[60], which can be explained by the different behaviors of C and Si under different potential windows (Fig. 58 (e) and (f)).

Then, by comparing three cases in Case I, one may find that composite anode with a lower percentage of Si-C particles has a higher increasing rate of concentration in the Si-C zone near the end of the charging process. It should be attributed to the fact that the same applied current density would generate the same total amount of transferring Li-ion between anode and cathode. At the beginning of the charging process, the majority of Li-ions are stored mainly within the C zone, little difference is observed in the Si-C zone. However, when the C zone is almost fully filled, the Si-C zone becomes the dominating material. To store the same total amount of Li-ion, the one with a small number of Si-C zones need to store more Li-ion in Si-C zones at the same time. This can also explain the discharging behavior among these three cases in Case I that Li-ion concentration in the Si-C zone with less number of Si-C particles would decrease later. However, for Case II, the mechanism is different due to the various OCP properties of different Si-C compound particles. It is indicated from Fig. 58 (f) that a higher Si proportion in Si-C compound particles would make the potential higher at the same SOC value, especially for discharging. Fig. 61 (b) shows that more Si addition in Si-C particles significantly increases the Li-ion concentration in the Si-C zone and slightly decreases it in C zone. This can be explained by Fig. 61 (c) which is the overall equilibrium potential of C zone and Si-C zone. It indicates that the equilibrium potential in different materials should keep almost the same at the same time, which means C and Si-C materials should be in the same SOC at the same time in the charging process since the charging OCPs are almost the same. Consequently, the Li-ion concentration in the Si-C zone with a higher Si proportion increases faster to reach the same SOC since its maximum Li-ion concentration is higher.

On the contrary, Li-ion concentration in C zone would increase slower compared to the baseline to ensure the total Li-ion amount keeps the same simultaneously. These two factors are coupled together to determine the Li-ion concentration evolution. For the discharging process, although Si-C zone with a lower Si proportion should reach a low SOC faster (Fig. 58 (f)), Li-ion concentration in the one with higher Si proportion decrease faster instead due to its higher maximum Li-ion concentration value.

The constraint effect is also studied here. A fixed boundary condition was applied on the top surface of the anode, considering that different layers would cause constrain effect on each other in the real-world applications of batteries. Fig. 61 (a) and (b) show that constraints on the anode surface do little effect on voltage and Li-ion concentration. The way that mechanical constraint would affect the electrochemical properties is that the constrain can influence the mechanical stress which conversely affects the Li-ion diffusion in the active particles. The results show that stress plays a minor role in Li-ion diffusion compared to concentration gradient and electrochemical conditions. So the mechanical constraint effect on electrochemical can be ignored. Note that this study only focuses on the first cycle of the battery, when it comes to cycling properties in which the mechanical failure and fatigue behaviors dominate the battery performance degradation, the stress effect would be more significant.

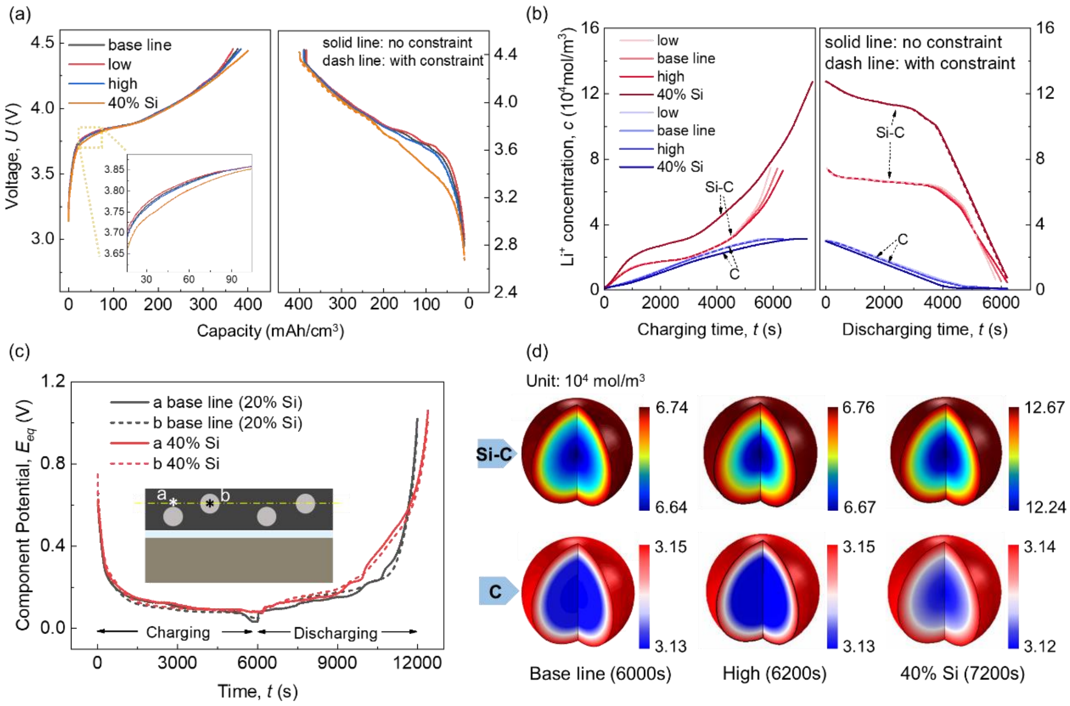

Figure 61 Electrochemical properties for different configurations of Case I and Case II, with and without constraint. (a) voltage comparison; (b) Li concentration comparison in Si-C zone and C zone, respectively, in macro-scale; (c) equilibrium potential in Si-C zone and C zone in macro-scale; (d) Li concentration in Si-C compound particle and C particle in microscale

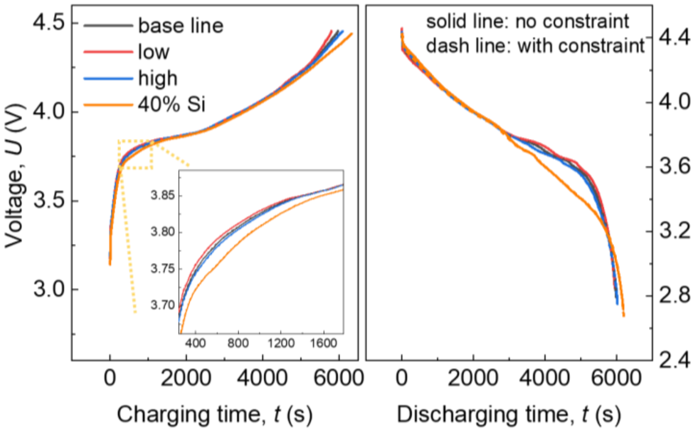

Figure 62 Voltage vs. Time profile of different Cases in Case I and Case II with and without mechanical constraint.

Furthermore, the Li-ion concentration distributions within microparticle (Si-C compound particle for Si-C zone and C particle from C zone) are analyzed, as shown in Fig. 61 (d). It indicates that the Li-ion concentration gradient along the particle radius is small for all cases since the low charging rate usually leads to a quasi-equilibrium status. The mean value of Li-ion concentration in microscale matches the one in macroscale (Fig. 61 (b)) which indicates that the multiscale model works well.

5.2.2 Mechanical behavior for Case I and Case II with and without constraint

The deformation of the anode is mainly generated by the Si-C zones, which contain nano Si particles (exhibition a maximum of 400% volume change during cycling). From an overall view of Fig. 63 (a), the shapes of curves are very similar to the Li-ion concentration curve (Fig. 61 (b)), which agrees to the conclusion that the deformation of Si-C zone is mainly dominated by the Li-ion concentration (electrochemical behavior) and the swelling coefficient (a material property).

For Case I, Si-C zones are made of Si-C particles with the same Si proportion in microscale which means they have the same swelling coefficient. From Fig. 61 (b) we know that the Li-ion concentration in Si-C zones has little difference till the end of charging. However, we observe that both the maximum deformation and the average deformation of the anode would be larger with more Si-C zones. It is reasonable that even the deformation of every single Si-C zone is almost the same, more amount of Si-C could generate more deformation in total. Note that the maximum deformation mostly depends on one single Si-C zone, especially the one closed to the surface, but when the amount of Si-C zone increases, they would affect each other that in-plane deformation is restricted and leading to a larger deformation in the thickness direction. The increase of Si-C zones influences more on average deformation that the overall deformed areas would increase (more green and yellow zones show in the one with more Si-C zones (Fig. 63 (b)).

For Case II, the maximum deformation of the one with 40 wt% Si in Si-C particles shows an extremely huge increase compared with the baseline (20 wt% Si in Si-C particles). This is due to the increased swelling coefficient of the Si-C zone caused by the increased percentage of Si. However, the increase in average deformation is not as huge as that of the maximum deformation. This can be attributed to the fact that the average deformation is a coordinate result from the deformation of the Si-C zone and the constraint of C zone. Thus, to reduce the deformation, deformable zones (or particles in reality) should be embedded as deep as possible into the matrix so that the matrix may help to constrain the deformation. Note that when a fixed boundary condition is applied on the top surface, there will be no deformation of the anode such that the constraint effect on the overall anode deformation is not discussed here.

To analyze the stress within composite anode in macroscale during the charging/discharging behavior, two stress components are considered here, i.e. σ_x and σ_y, in the in-plane and thickness direction, respectively. Two specific points, *a* and *b*, in two directions were analyzed in this study (Fig. 63 (c)). For both directions, stress component at Point *a* is usually tensile stress while stress at Point *b* is compressive stress. From an overall view, we can see that the stress evolution in both directions behave very similarly as the Li-ion concentration does (Fig. 63 (d) and (e)). This is because the stress here is mainly caused by the deformation of Si-C zones which is directly related to the Li-ion concentration. Due to the Li-ion concentration evolution behavior, the stress in the discharging process would keep the value at the beginning for a while until the Li-ion concentration in the Si-C zone starts to decrease. The tensile stress at Point *a* is the driving force of fracture which may cause cracks in C zone. Compressive stress at Point *b* is one of the responsible reasons for interface crack or debonding between C zone and Si-C zone. This is because if we consider the plastic behavior of C zone which may cause irreversible deformation, the compressive stress here may change into tensile stress which is the driving force of debonding. That means a long platform of stress in discharging would be very harmful. Therefore, a tradeoff between the high capacity (high Si proportion) and mechanical robustness needs to be considered. When considering the constraint effects, the stress evolution changing can be seen in Figs. 63(d) and (e). A general change for all cases is that the constraint may contribute to more compressive stress. Thus, stress at Point *b* exhibiting an obvious increase of magnitude while stress at Point *a* decrease. That means the constraint may mitigate the risk of the tensile crack in C zone but increase the possibility of debonding and crack at the interface of C zone and Si-C zone.

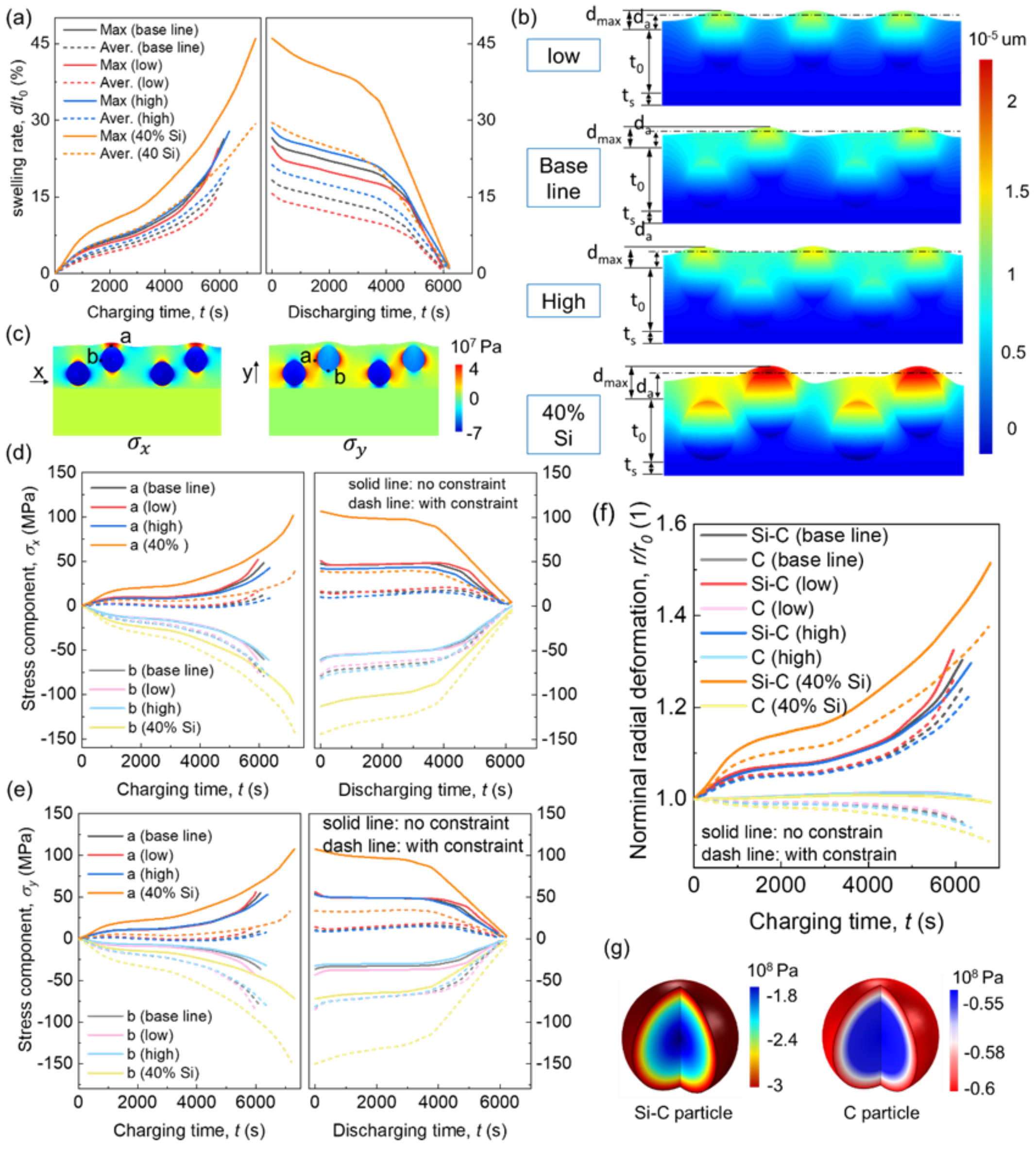

Figure 63 Mechanical properties comparison for different configurations of Case I and

Case II, with and without constraint. (a)deformation comparison in macro-scale for Case I and Case II without constraint; (b) deformation distribution in macro-scale for Case I and Case II without constraint; (c) stress extract point and stress component distribution illustration; (d) and (e) stress component along thickness and in-plane direction at two specific points of Si-C zone and C zone in macro-scale; (f) particle radius changes in microscale during charging process for Case I and Case II, with and without constraint; (g) stress distribution in microparticles of baseline.

In microscale, particle radius change shows a similar trend to the macro deformation (Fig. 63 (f)). Si-C particle shows a bigger radius change with a lower amount of Si-C zone for Case I. This is because the Li-ion concentration increase faster in the Si-C zone when the amount of Si-C zone is lower (Fig. 61 (b)). However, when the Si-C particle contains more Si (Case II), the radius shows an obvious increase compared with the baseline. As for the C particles, the radius almost keeps unchanged since the swelling of C can be ignored compared with Si. When considering the constraints, the radius increase of Si-C particles is reduced for all cases. And the radius of C particle shows a decreasing behavior, which is attributed to the extruding caused by the expanding Si-C particles. That means the macroscale constraint boundary condition would have effects on the microscale particle deformation. The deformation behavior of the Si-C and C particles is not only dominated by the Li-ion concentration but also affected by the mechanical boundaries. For the stress in microscale, the baseline case is selected to be representative (Fig. 63 (g)). The hydrostatic stress at the end of charging in the Si-C particle is larger than that in C particle, and both are in the compressive status. The stress magnitude in microscale particles is slightly larger than that in macroscale due to the porous structure of the anode.

5.2.3 Better strategy to achieve a high capability

In this chapter, we proposed two ways to achieve the high capacity of the composite anode, i.e., Case I and Case II mentioned above. Electromechanical and mechanical properties of all cases from Case I and Case II are discussed in *Sections 5.2.1* and *5.2.2*. To point out which one is a better way to achieve high capacity aiming at commercial application, a new configuration of Case I called “ultrahigh” with eight Si-C zones was established to achieve the same overall cell capacity with the high-case of Case II (the one with 40 wt% Si in Si-C zone). Considering that the constraint condition is closer to the real working circumstance of batteries, only the models with constraints are studied in this section.

Both electrochemical and mechanical performances are shown in Fig. 64. The voltage profile shows that the voltage of a cell is greatly related to the overall capacity (or Si proportion) rather than the specific structure (Figs. 64 (a) and 65). The Li-ion concentration in Si-C zones of high-case of Case II is much higher than the ultrahigh-case of Case I, while the Li-ion concentration in C zones shows little difference (Fig. 64 (b)). The higher Li-ion concentration in the Si-C zone of the high-case of Case II results in a larger deformation of Si-C zones which then leads to larger stress components both in in-plane or thickness direction (Fig. 64 (c) and (d)). As shown in Fig. 64 (e), the Mises stress distribution in macroscale for these two cases further agrees that the overall stress magnitude of the high-case of Case II is larger than that in ultrahigh case of Case I and the large stress usually occurs at the boundary of Si-C zones. The stress in microscale Si-C particles shows that the stress magnitude in Si-C particles from high-case of Case II is almost double to that of the ultrahigh case of Case I. However, the stress in microscale C particles shows an opposite result, which implies that the increase of Si-C zones would play a more important role in C zones.

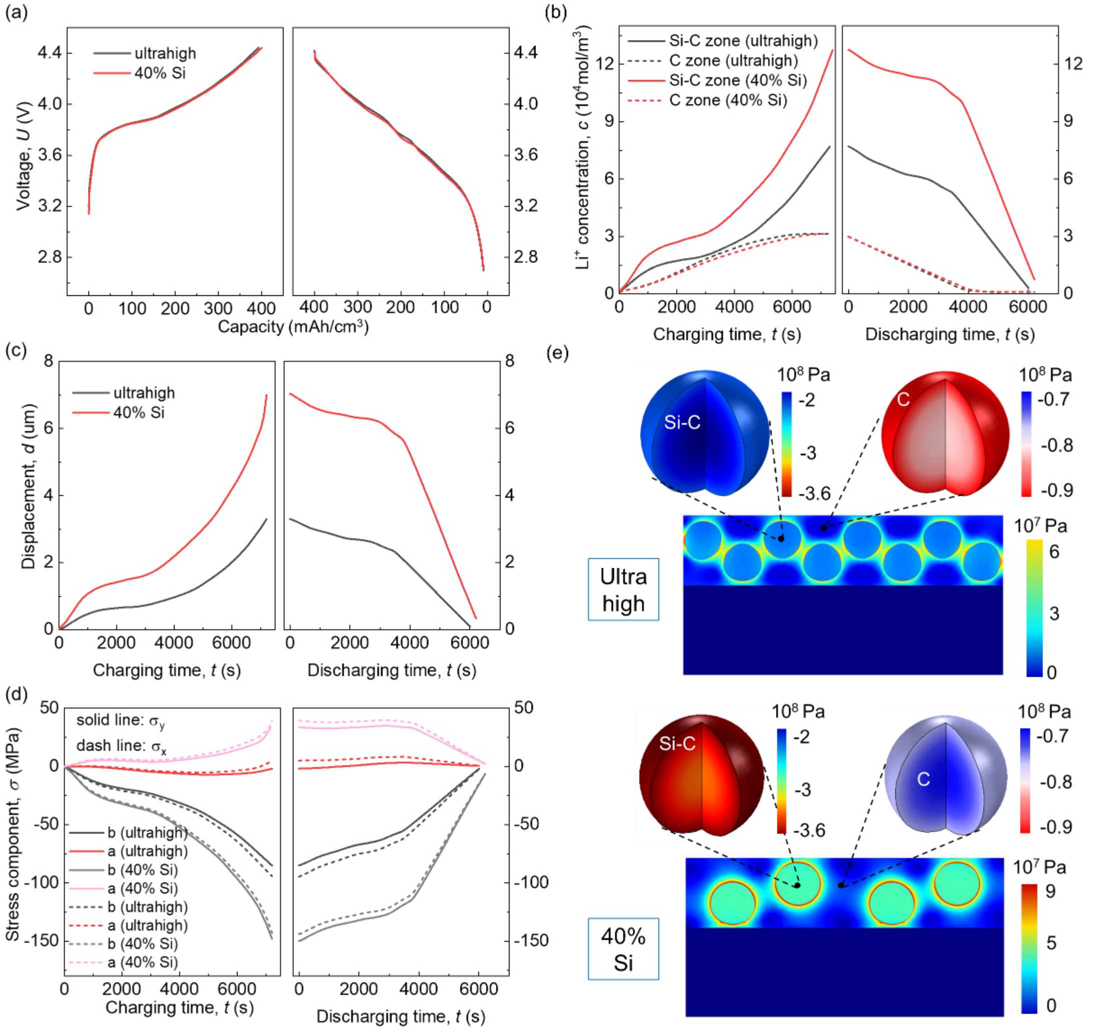

Figure 64 Electrochemical and mechanical properties for ultrahigh case of Case I and the high case of Case II which have the same overall Si ratio in the composite anode. (a) voltage comparison; (b) Li concentration comparison in macro-scale; (c) comparison of deformation of Si-C zone; (d) stress component comparison in micro-scale extracted from the same position defined by Fig. 5 (c); (e) stress distribution in different particles in microscale for both cases.

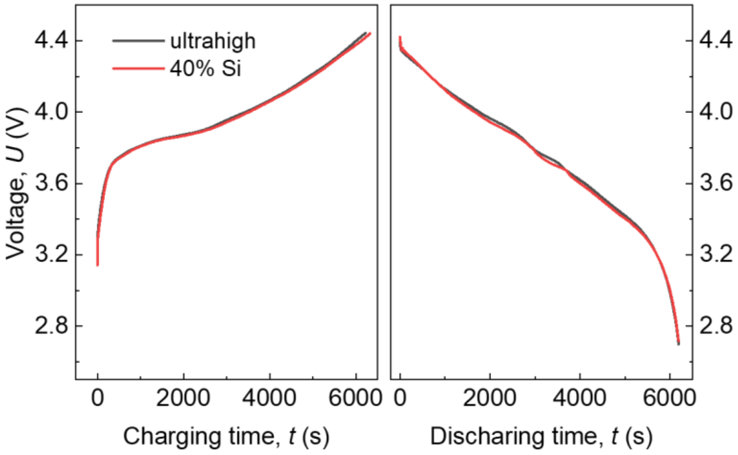

Figure 65 Voltage vs. Time profile of ultrahigh in Case I and 40% Si in Case II with mechanical constraint.

When achieving the same overall cell capacity, the structure construction as in Case I would generate less deformation and stress in the Si-C zones but the increasing amounts of Si-C zones would bring more effects on C zone. Considering that the mechanical damage of this kind of composite anode mainly occur within the vicinity of Si-C zones, Case I is a better way to achieve high capacity. Further study needs to be done to obtain the optimal configuration.

5.2.4 Charging rate effects

To analyze the charging rate effects on this battery cell with the composite anode, two more cases with different current densities of 50 A/m^2 and 80 A/m^2 are studied based on the baseline case. All the other settings are the same to the baseline discussed in previous sections with constraint. The charging profiles show that a higher charging rate would generate a higher voltage at same SOC so that it would reach the limit voltage at an early

SOC (Fig. 66 (a)). It indicates that when the battery cell is charged at a high charging rate, the usable capacity would be reduced. In the meantime, the discharging profiles indicate that a larger voltage drop would occur at the beginning for a higher discharging rate case which may cause a lower discharging platform as well as a lower discharging capacity. This observation agrees well with the Ref.[148]. As shown in Fig. 66 (b), the average Li-ion concentration profiles indicate that the Li-ion concentration increases faster at a higher charging rate in Si-C zones in the charging process while it decreases faster as well in the discharging process.

On the contrary, the Li-ion concentration increases slower at a higher charging rate in C zones in charging process and decrease slower as well in discharging process. The low average Li-ion concentration at the charging end of a high charging rate also implies a low capacity. The Li-ion concentration behavior almost directly dominates the deformation and stress evolution of the Si-C zone (Fig. 66 (c) and (d)). Here, we only discussed the charging process that a higher charging rate would generate a larger deformation of Si-C zone as well as larger stresses during the process. But the final deformation and stresses of the higher charging rate at the charging end are smaller instead. Then at the discharging process, the initial residual deformation and stresses would be lower for a higher charging rate. Thus, from the mechanical point of view, fast charging is beneficial for the mechanical integrity under the promise of the same nominal voltage at the cost of less utilized capacity though. This can be further explained by the Li-ion concentration profile in microscale particles

(Fig. 66 (e)). It indicates that the concentration difference between the particle surface and center would be larger of the higher charging rate, especially for the C particles. Thus, the Li-ion concentration on particle surface which dominates the cell voltage would reach the limit value faster at higher charging rate. Then the average Li-ion concentration would be lower correspondingly, which further causes the lower deformation and stress. It also indicates that the charging rate mainly influences the C materials. Note that the charging rates here are primarily high rates; the slow rates are not considered here. Systematic work describing the slow rates (like C/5, C/10, C/25) will be discussed in the future.

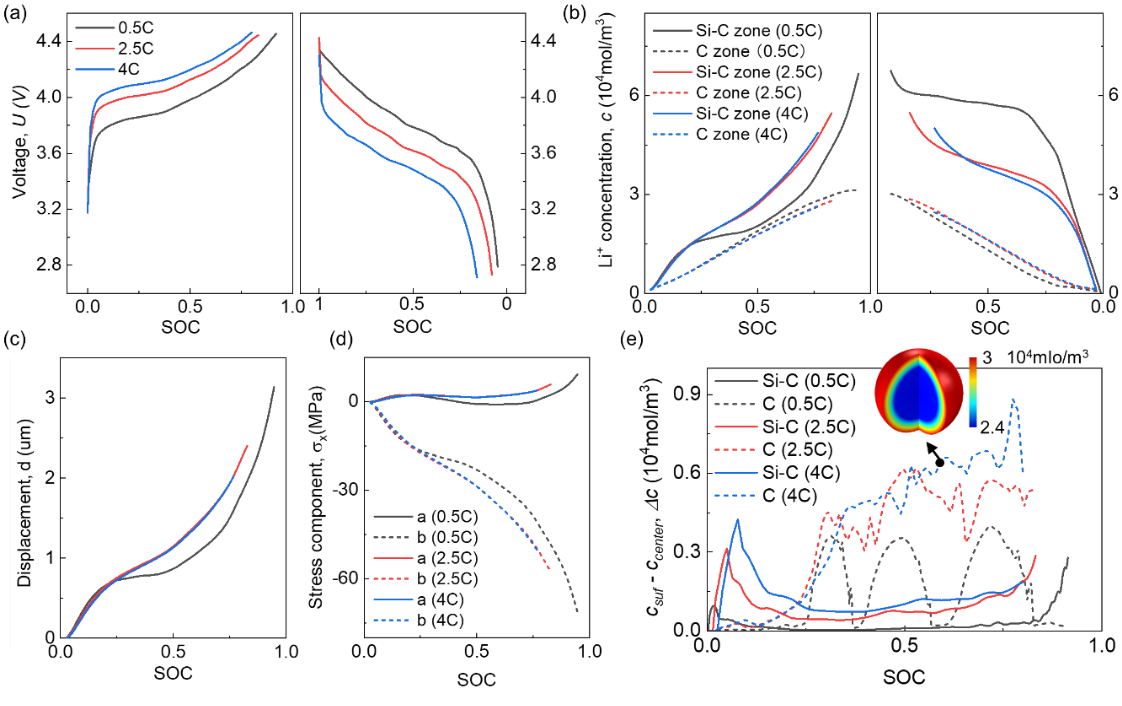

Figure 66 Electrochemical and mechanical properties comparison for different charging rate based on baseline of Case I (a) voltage comparison; (b) Li concentration comparison in macro-scale; (c) comparison of deformation of Si-C zone; (d) stress component comparison in macro-scale extracted from point a of σ_x defined by Fig. 5 (c); (e) Li-ion concentration gradient in different particles of microscale

5.3 Conclusions

A type of Si-C composite anode material was characterized by SEM method. The electromechanical properties of this material were then measured by half-cell and the voltage and mechanical deformation profiles were obtained via *in-situ* full-cell test. In addition, a cycling test was also performed on a pouch cell based on this anode. To further study the electrochemical-mechanical coupling mechanism in battery cell level and microscale particle level, a simultaneous multiphysics-multiscale model was developed and validated.

This model was then used to study the effects of Si ratio, mechanical constraint, and charging rate on electrochemical and mechanical performance. Two cases to achieve different Si ratios were considered, and Case I (different amounts of Si-C zones in macroscale anode with same Si proportion in microscale Si-C particles) was demonstrated to be a better solution to achieve high capacity. Mechanical constraint showed more effects on mechanical behaviors which may cause electrochemical degradation when considering the cycling behavior. A high charging rate would reduce the capacity but generate low deformation and stress of Si-C zones when the battery is fully charged.

This study provides a versatile modeling framework to numerically describe the multiphysics and multiscale behaviors of Si-C composite anode. Results pave the path for next-generation anodes design, aiming at high-energy and commercially feasible Si-C composite anodes.

CHAPTER 6 CONCLUDING REMARKS

In this thesis work, we developed a systematic study of the mutliphysics behavior of LIB anode materials from the atomic scale to the cell level. First, the fundamental mechanism of Li diffusion behaviors in various Si/C composite materials (mixture mode and core-shell mode) was studied using the DFT modeling method, and we found that the Li diffusivity in Si is enhanced by the addition of C material and the effects are related to the atomic structure of C in core-shell mode. The quantitative description of the diffusivities of various Si/C composite structures was obtained which can be used in the continuum scale modeling as the inputs. Then, a multiphysics modeling framework considering the Li diffusion and mechanical deformation at the particle level was then established. The relationship between mechanical failure and electrochemical performance in Si/C core-shell particles is revealed using this model. Next, based on this multiphysics model, the contact behavior of two Si/C core-shell particles was studied, and both the electrochemical and mechanical performance were analyzed of the contact particles with various C shell thicknesses and moduli, which gives the guidance on Si/C core-shell particle design. Then, five representative Si/C composite nanostructures were compared using the weak form method of the multiphysics framework, providing further design guidance on Si/C core-shell and related structures. Finally, the model was extended into a multi-scale one, which describes the multiphysics behavior both at the particle level and cell level. This study reveals the fundamental mechanism of the Si/C composite anode with various Si proportions and demonstrates a better way to achieve higher Si contents with acceptable performance.

This study systematically investigates the multiphysics behavior of Si/C composite anodes material from the atomic level to cell level using DFT modeling and FEA methodology, revealing the underlying mechanism of the fundamental physical process and the coupling mechanism among various physical fields, as well as providing efficient and powerful tools in the design, development, and evaluation of high energy density lithium-ion batteries.

REFERENCES

1. Hwang, T. H.; Lee, Y. M.; Kong, B.-S.; Seo, J.-S.; Choi, J. W., Electrospun Core–Shell Fibers for Robust Silicon Nanoparticle-Based Lithium Ion Battery Anodes. *Nano Letters* **2012,** *12* (2), 802-807.
2. Li, X.; Yan, P.; Xiao, X.; Woo, J. H.; Wang, C.; Liu, J.; Zhang, J.-G., Design of porous Si/C–graphite electrodes with long cycle stability and controlled swelling. *Energy & Environmental Science* **2017,** *10* (6), 1427-1434.
3. Lv, P.; Zhao, H.; Gao, C.; Zhang, T.; Liu, X., Highly efficient and scalable synthesis of SiOx/C composite with core-shell nanostructure as high-performance anode material for lithium ion batteries. *Electrochimica Acta* **2015,** *152*, 345-351.
4. Huang, S.; Fan, F.; Li, J.; Zhang, S.; Zhu, T., Stress generation during lithiation of high-capacity electrode particles in lithium ion batteries. *Acta Materialia* **2013,** *61* (12), 4354-4364.
5. Xu, R.; Yang, Y.; Yin, F.; Liu, P.; Cloetens, P.; Liu, Y.; Lin, F.; Zhao, K., Heterogeneous damage in Li-ion batteries: Experimental analysis and theoretical modeling. *Journal of the Mechanics and Physics of Solids* **2019,** *129*, 160-183.
6. Dimov, N.; Kugino, S.; Yoshio, M., Mixed silicon–graphite composites as anode material for lithium ion batteries: Influence of preparation conditions on the properties of the material. *Journal of Power Sources* **2004,** *136* (1), 108-114.
7. Obrovac, M. N.; Chevrier, V. L., Alloy Negative Electrodes for Li-Ion Batteries. *Chemical reviews* **2014,** *114* (23), 11444-11502.
8. Hochgatterer, N. S.; Schweiger, M. R.; Koller, S.; Raimann, P. R.; Wöhrle, T.; Wurm, C.; Winter, M., Silicon/Graphite Composite Electrodes for High-Capacity Anodes: Influence of Binder Chemistry on Cycling Stability. *Electrochemical and Solid-State Letters* **2008,** *11* (5), A76.
9. Fuchsbichler, B.; Stangl, C.; Kren, H.; Uhlig, F.; Koller, S., High capacity graphite–silicon composite anode material for lithium-ion batteries. *Journal of Power Sources* **2011,** *196* (5), 2889-2892.
10. Ma, J.; Sung, J.; Hong, J.; Chae, S.; Kim, N.; Choi, S.-H.; Nam, G.; Son, Y.; Kim, S. Y.; Ko, M.; Cho, J., Towards maximized volumetric capacity via pore-coordinated design for large-volume-change lithium-ion battery anodes. *Nature Communications* **2019,** *10* (1), 475.
11. Wu, H.; Yu, G.; Pan, L.; Liu, N.; McDowell, M. T.; Bao, Z.; Cui, Y., Stable Li-ion battery anodes by in-situ polymerization of conducting hydrogel to conformally coat silicon nanoparticles. *Nature Communications* **2013,** *4* (1), 1943.
12. Zhou, X.; Cao, A.-M.; Wan, L.-J.; Guo, Y.-G., Spin-coated silicon nanoparticle/graphene electrode as a binder-free anode for high-performance lithium-ion batteries. *Nano Research* **2012,** *5* (12), 845-853.
13. Zhu, B.; Jin, Y.; Tan, Y.; Zong, L.; Hu, Y.; Chen, L.; Chen, Y.; Zhang, Q.; Zhu, J., Scalable Production of Si Nanoparticles Directly from Low Grade Sources for

Lithium-Ion Battery Anode. *Nano Letters* **2015,** *15* (9), 5750-5754.

14. Xue, L.; Xu, G.; Li, Y.; Li, S.; Fu, K.; Shi, Q.; Zhang, X., Carbon-Coated Si Nanoparticles Dispersed in Carbon Nanotube Networks As Anode Material for Lithium-Ion Batteries. *ACS Applied Materials & Interfaces* **2013,** *5* (1), 21-25.
15. Ha, J.; Paik, U., Hydrogen treated, cap-opened Si nanotubes array anode for high power lithium ion battery. *Journal of Power Sources* **2013,** *244*, 463-468.
16. Wen, Z.; Lu, G.; Mao, S.; Kim, H.; Cui, S.; Yu, K.; Huang, X.; Hurley, P. T.; Mao, O.; Chen, J., Silicon nanotube anode for lithium-ion batteries. *Electrochemistry Communications* **2013,** *29*, 67-70.
17. Wu, H.; Chan, G.; Choi, J. W.; Ryu, I.; Yao, Y.; McDowell, M. T.; Lee, S. W.; Jackson, A.; Yang, Y.; Hu, L.; Cui, Y., Stable cycling of double-walled silicon nanotube battery anodes through solid–electrolyte interphase control. *Nature Nanotechnology* **2012,** *7* (5), 310-315.
18. Chan, C. K.; Patel, R. N.; O'Connell, M. J.; Korgel, B. A.; Cui, Y., Solution-Grown Silicon Nanowires for Lithium-Ion Battery Anodes. *ACS Nano* **2010,** *4* (3), 1443-1450.
19. Cho, J.-H.; Picraux, S. T., Enhanced Lithium Ion Battery Cycling of Silicon Nanowire Anodes by Template Growth to Eliminate Silicon Underlayer Islands. *Nano Letters* **2013,** *13* (11), 5740-5747.
20. Jing, S.; Jiang, H.; Hu, Y.; Li, C., Directly grown Si nanowire arrays on Cu foam with a coral-like surface for lithium-ion batteries. *Nanoscale* **2014,** *6* (23), 14441-14445.
21. Cui, L.-F.; Hu, L.; Choi, J. W.; Cui, Y., Light-Weight Free-Standing Carbon Nanotube-Silicon Films for Anodes of Lithium Ion Batteries. *ACS Nano* **2010,** *4* (7), 3671-3678.
22. Abel, P. R.; Lin, Y.-M.; Celio, H.; Heller, A.; Mullins, C. B., Improving the Stability of Nanostructured Silicon Thin Film Lithium-Ion Battery Anodes through Their Controlled Oxidation. *ACS Nano* **2012,** *6* (3), 2506-2516.
23. Li, P.; Zhao, G.; Zheng, X.; Xu, X.; Yao, C.; Sun, W.; Dou, S. X., Recent progress on silicon-based anode materials for practical lithium-ion battery applications. *Energy Storage Materials* **2018,** *15*, 422-446.
24. Andersen, H. F.; Foss, C. E. L.; Voje, J.; Tronstad, R.; Mokkelbost, T.; Vullum, P. E.; Ulvestad, A.; Kirkengen, M.; Mæhlen, J. P., Silicon-Carbon composite anodes from industrial battery grade silicon. *Scientific Reports* **2019,** *9* (1), 14814.
25. Gu, P.; Cai, R.; Zhou, Y.; Shao, Z., Si/C composite lithium-ion battery anodes synthesized from coarse silicon and citric acid through combined ball milling and thermal pyrolysis. *Electrochimica Acta* **2010,** *55* (12), 3876-3883.
26. Yi, R.; Zai, J.; Dai, F.; Gordin, M. L.; Wang, D., Dual conductive network-enabled graphene/Si–C composite anode with high areal capacity for lithium-ion batteries. *Nano Energy* **2014,** *6*, 211-218.
27. Zhang, X.; Zhou, L.; Zhang, Y.; Yan, S.; Huang, J.; Fang, Z., A facile method to fabricate a porous Si/C composite with excellent cycling stability for use as the anode in a lithium ion battery. *Chemical Communications* **2019,** *55* (89), 13438-13441.
28. **!!! INVALID CITATION !!! [24, 25]**.

29. Du, C.; Chen, M.; Wang, L.; Yin, G., Covalently-functionalizing synthesis of Si@C core–shell nanocomposites as high-capacity anode materials for lithium-ion batteries. *Journal of Materials Chemistry* **2011,** *21* (39), 15692-15697.
30. Ghosh Chaudhuri, R.; Paria, S., Core/shell nanoparticles: classes, properties, synthesis mechanisms, characterization, and applications. *Chemical reviews* **2012,** *112* (4), 2373-433.
31. Chen, Q.; Sun, S.; Zhai, T.; Yang, M.; Zhao, X.; Xia, H., Yolk–Shell NiS2 Nanoparticle-Embedded Carbon Fibers for Flexible Fiber-Shaped Sodium Battery. *Advanced Energy Materials* **2018,** *8* (19), 1800054.
32. Purbia, R.; Paria, S., Yolk/shell nanoparticles: classifications, synthesis, properties, and applications. *Nanoscale* **2015,** *7* (47), 19789-19873.
33. Li, X.; Xing, Y.; Xu, J.; Deng, Q.; Shao, L.-H., Uniform yolk–shell structured Si–C nanoparticles as a high performance anode material for the Li-ion battery. *Chemical Communications* **2020,** *56* (3), 364-367.
34. Chen, X.; Chen, C.; Zhang, Y.; Zhang, X.; Yang, D.; Dong, A., Exploiting oleic acid to prepare two-dimensional assembly of Si@graphitic carbon yolk-shell nanoparticles for lithium-ion battery anodes. *Nano Research* **2019,** *12* (3), 631-636.
35. Yang, L. Y.; Li, H. Z.; Liu, J.; Sun, Z. Q.; Tang, S. S.; Lei, M., Dual yolk-shell structure of carbon and silica-coated silicon for high-performance lithium-ion batteries. *Scientific Reports* **2015,** *5* (1), 10908.
36. Wu, P.; Guo, C.; Han, J.; Yu, K.; Dong, X.; Yue, G.; Yue, H.; Guan, Y.; Liu, A., Fabrication of double core–shell Si-based anode materials with nanostructure for lithium-ion battery. *RSC Advances* **2018,** *8* (17), 9094-9102.
37. Hu, L.; Luo, B.; Wu, C.; Hu, P.; Wang, L.; Zhang, H., Yolk-shell Si/C composites with multiple Si nanoparticles encapsulated into double carbon shells as lithium-ion battery anodes. *Journal of Energy Chemistry* **2019,** *32*, 124-130.
38. Liu, N.; Liu, J.; Jia, D.; Huang, Y.; Luo, J.; Mamat, X.; Yu, Y.; Dong, Y.; Hu, G., Multi-core yolk-shell like mesoporous double carbon-coated silicon nanoparticles as anode materials for lithium-ion batteries. *Energy Storage Materials* **2019,** *18*, 165-173.
39. Jiao, M.; Liu, K.; Shi, Z.; Wang, C., SiO2/Carbon Composite Microspheres with Hollow Core–Shell Structure as a High-Stability Electrode for Lithium-Ion Batteries. *ChemElectroChem* **2017,** *4* (3), 542-549.
40. Ashuri, M.; He, Q.; Liu, Y.; Zhang, K.; Emani, S.; Sawicki, M. S.; Shamie, J. S.; Shaw, L. L., Hollow Silicon Nanospheres Encapsulated with a Thin Carbon Shell: An Electrochemical Study. *Electrochimica Acta* **2016,** *215*, 126-141.
41. Ashuri, M.; He, Q.; Zhang, K.; Emani, S.; Shaw, L. L., Synthesis of hollow silicon nanospheres encapsulated with a carbon shell through sol–gel coating of polystyrene nanoparticles. *Journal of Sol-Gel Science and Technology* **2017,** *82* (1), 201-213.
42. Zuo, P.; Yin, G.; Ma, Y., Electrochemical stability of silicon/carbon composite anode for lithium ion batteries. *Electrochimica Acta* **2007,** *52* (15), 4878-4883.
43. Luo, Z.; Fan, D.; Liu, X.; Mao, H.; Yao, C.; Deng, Z., High performance silicon carbon

composite anode materials for lithium ion batteries. *Journal of Power Sources* **2009,** *189* (1), 16-21.

44. Park, J.-B.; Lee, K.-H.; Jeon, Y.-J.; Lim, S.-H.; Lee, S.-M., Si/C composite lithium-ion battery anodes synthesized using silicon nanoparticles from porous silicon. *Electrochimica Acta* **2014,** *133*, 73-81.
45. Gao, X.; Lu, W.; Xu, J., Modeling framework for multiphysics-multiscale behavior of Si–C composite anode. *Journal of Power Sources* **2020,** *449*, 227501.
46. Chang, S.; Moon, J.; Cho, M., Stress-diffusion coupled multiscale analysis of Si anode for Li-ion battery†. *Journal of Mechanical Science and Technology* **2015,** *29* (11), 4807-4816.
47. Tritsaris, G. A.; Zhao, K.; Okeke, O. U.; Kaxiras, E., Diffusion of Lithium in Bulk Amorphous Silicon: A Theoretical Study. *The Journal of Physical Chemistry C* **2012,** *116* (42), 22212-22216.
48. Ding, N.; Xu, J.; Yao, Y. X.; Wegner, G.; Fang, X.; Chen, C. H.; Lieberwirth, I., Determination of the diffusion coefficient of lithium ions in nano-Si. *Solid State Ionics* **2009,** *180* (2), 222-225.
49. Deshpande, R.; Cheng, Y.-T.; Verbrugge, M. W., Modeling diffusion-induced stress in nanowire electrode structures. *Journal of Power Sources* **2010,** *195* (15), 5081-5088.
50. Zhang, X.-y.; Chen, H.-s.; Fang, D.-n., Diffusion-induced stress of electrode particles with spherically isotropic elastic properties in lithium-ion batteries. *Journal of Solid State Electrochemistry* **2016,** *20* (10), 2835-2845.
51. Huang, J. Y.; Zhong, L.; Wang, C. M.; Sullivan, J. P.; Xu, W.; Zhang, L. Q.; Mao, S. X.; Hudak, N. S.; Liu, X. H.; Subramanian, A.; Fan, H.; Qi, L.; Kushima, A.; Li, J., In Situ Observation of the Electrochemical Lithiation of a Single SnO<sub>2</sub> Nanowire Electrode. *Science* **2010,** *330* (6010), 1515.
52. Liu, X. H.; Huang, J. Y., In situ TEM electrochemistry of anode materials in lithium ion batteries. *Energy & Environmental Science* **2011,** *4* (10), 3844-3860.
53. Wang, C.-M.; Li, X.; Wang, Z.; Xu, W.; Liu, J.; Gao, F.; Kovarik, L.; Zhang, J.-G.; Howe, J.; Burton, D. J.; Liu, Z.; Xiao, X.; Thevuthasan, S.; Baer, D. R., In Situ TEM Investigation of Congruent Phase Transition and Structural Evolution of Nanostructured Silicon/Carbon Anode for Lithium Ion Batteries. *Nano Letters* **2012,** *12* (3), 1624-1632.
54. Liu, Q.; Cui, Z.; Zou, R.; Zhang, J.; Xu, K.; Hu, J., Surface Coating Constraint Induced Anisotropic Swelling of Silicon in Si–Void@SiO x Nanowire Anode for Lithium-Ion Batteries. *Small* **2017,** *13* (13), 1603754.
55. Liu, X. H.; Wang, J. W.; Huang, S.; Fan, F.; Huang, X.; Liu, Y.; Krylyuk, S.; Yoo, J.; Dayeh, S. A.; Davydov, A. V.; Mao, S. X.; Picraux, S. T.; Zhang, S.; Li, J.; Zhu, T.; Huang, J. Y., In situ atomic-scale imaging of electrochemical lithiation in silicon. *Nature Nanotechnology* **2012,** *7* (11), 749-756.
56. Nishikawa, K.; Munakata, H.; Kanamura, K., In-situ observation of one silicon particle during the first charging. *Journal of Power Sources* **2013,** *243*, 630-634.

57. Shao, M., In situ microscopic studies on the structural and chemical behaviors of lithium-ion battery materials. *Journal of Power Sources* **2014,** *270*, 475-486.
58. Kasavajjula, U.; Wang, C.; Appleby, A. J., Nano- and bulk-silicon-based insertion anodes for lithium-ion secondary cells. *Journal of Power Sources* **2007,** *163* (2), 1003-1039.
59. Nishikawa, K.; Moon, J.; Kanamura, K., In-situ observation of volume expansion behavior of a silicon particle in various electrolytes. *Journal of Power Sources* **2016,** *302*, 46-52.
60. Yao, K. P. C.; Okasinski, J. S.; Kalaga, K.; Almer, J. D.; Abraham, D. P., Operando Quantification of (De)Lithiation Behavior of Silicon–Graphite Blended Electrodes for Lithium-Ion Batteries. *Advanced Energy Materials* **2019,** *9* (8), 1803380.
61. Sethuraman, V. A.; Chon, M. J.; Shimshak, M.; Srinivasan, V.; Guduru, P. R., In situ measurements of stress evolution in silicon thin films during electrochemical lithiation and delithiation. *Journal of Power Sources* **2010,** *195* (15), 5062-5066.
62. Chason, E.; Sheldon, B. W., Monitoring Stress in Thin Films During Processing. *Surface Engineering* **2003,** *19* (5), 387-391.
63. Sethuraman, V. A.; Chon, M. J.; Shimshak, M.; Van Winkle, N.; Guduru, P. R., In situ measurement of biaxial modulus of Si anode for Li-ion batteries. *Electrochemistry Communications* **2010,** *12* (11), 1614-1617.
64. Zeng, Z.; Liu, N.; Zeng, Q.; Lee, S. W.; Mao, W. L.; Cui, Y., In situ measurement of lithiation-induced stress in silicon nanoparticles using micro-Raman spectroscopy. *Nano Energy* **2016,** *22*, 105-110.
65. Christensen, J.; Newman, J., Stress generation and fracture in lithium insertion materials. *Journal of Solid State Electrochemistry* **2006,** *10* (5), 293-319.
66. Cui, Z.; Gao, F.; Qu, J., A finite deformation stress-dependent chemical potential and its applications to lithium ion batteries. *Journal of the Mechanics and Physics of Solids* **2012,** *60* (7), 1280-1295.
67. Bower, A. F.; Guduru, P. R., A simple finite element model of diffusion, finite deformation, plasticity and fracture in lithium ion insertion electrode materials. *Modelling and Simulation in Materials Science and Engineering* **2012,** *20* (4), 045004.
68. Bower, A. F.; Guduru, P. R.; Sethuraman, V. A., A finite strain model of stress, diffusion, plastic flow, and electrochemical reactions in a lithium-ion half-cell. *Journal of the Mechanics and Physics of Solids* **2011,** *59* (4), 804-828.
69. Golmon, S.; Maute, K.; Lee, S.-H.; Dunn, M. L., Stress generation in silicon particles during lithium insertion. *Applied Physics Letters* **2010,** *97* (3), 033111.
70. Cheng, Y.-T.; Verbrugge, M. W., Evolution of stress within a spherical insertion electrode particle under potentiostatic and galvanostatic operation. *Journal of Power Sources* **2009,** *190* (2), 453-460.
71. Zhao, K.; Pharr, M.; Cai, S.; Vlassak, J. J.; Suo, Z., Large Plastic Deformation in High-Capacity Lithium-Ion Batteries Caused by Charge and Discharge. *Journal of the American Ceramic Society* **2011,** *94* (s1), s226-s235.

72. Di Leo, C. V.; Rejovitzky, E.; Anand, L., Diffusion–deformation theory for amorphous silicon anodes: The role of plastic deformation on electrochemical performance. *International Journal of Solids and Structures* **2015,** *67-68*, 283-296.
73. Gao, X.; He, P.; Ren, J.; Xu, J., Modeling of contact stress among compound particles in high energy lithium-ion battery. *Energy Storage Materials* **2019,** *18*, 23-33.
74. Sethuraman, V. A.; Nguyen, A.; Chon, M. J.; Nadimpalli, S. P. V.; Wang, H.; Abraham, D. P.; Bower, A. F.; Shenoy, V. B.; Guduru, P. R., Stress Evolution in Composite Silicon Electrodes during Lithiation/Delithiation. *Journal of The Electrochemical Society* **2013,** *160* (4), A739-A746.
75. Xu, R.; Scalco de Vasconcelos, L.; Zhao, K., Computational analysis of chemomechanical behaviors of composite electrodes in Li-ion batteries. *Journal of Materials Research* **2016,** *31* (18), 2715-2727.
76. Xu, R.; Zhao, K., Mechanical interactions regulated kinetics and morphology of composite electrodes in Li-ion batteries. *Extreme Mechanics Letters* **2016,** *8*, 13-21.
77. Kashkooli, A. G.; Farhad, S.; Lee, D. U.; Feng, K.; Litster, S.; Babu, S. K.; Zhu, L.; Chen, Z., Multiscale modeling of lithium-ion battery electrodes based on nano-scale X-ray computed tomography. *Journal of Power Sources* **2016,** *307*, 496-509.
78. Stournara, M. E.; Qi, Y.; Shenoy, V. B., From Ab Initio Calculations to Multiscale Design of Si/C Core–Shell Particles for Li-Ion Anodes. *Nano Letters* **2014,** *14* (4), 2140-2149.
79. Gwak, Y.; Moon, J.; Cho, M., Multi-scale analysis of an electrochemical model including coupled diffusion, stress, and nonideal solution in a silicon thin film anode. *Journal of Power Sources* **2016,** *307*, 856-865.
80. Zhang, X.; Shyy, W.; Marie Sastry, A., Numerical Simulation of Intercalation-Induced Stress in Li-Ion Battery Electrode Particles. *Journal of The Electrochemical Society* **2007,** *154* (10), A910.
81. Brassart, L.; Zhao, K.; Suo, Z., Cyclic plasticity and shakedown in high-capacity electrodes of lithium-ion batteries. *International Journal of Solids and Structures* **2013,** *50* (7), 1120-1129.
82. Li, Y.; Yan, K.; Lee, H.-W.; Lu, Z.; Liu, N.; Cui, Y., Growth of conformal graphene cages on micrometre-sized silicon particles as stable battery anodes. *Nature Energy* **2016,** *1* (2), 15029.
83. Shi, F.; Song, Z.; Ross, P. N.; Somorjai, G. A.; Ritchie, R. O.; Komvopoulos, K., Failure mechanisms of single-crystal silicon electrodes in lithium-ion batteries. *Nature Communications* **2016,** *7* (1), 11886.
84. Radvanyi, E.; Porcher, W.; De Vito, E.; Montani, A.; Franger, S.; Jouanneau Si Larbi, S., Failure mechanisms of nano-silicon anodes upon cycling: an electrode porosity evolution model. *Physical chemistry chemical physics : PCCP* **2014,** *16* (32), 17142-53.
85. Oumellal, Y.; Delpuech, N.; Mazouzi, D.; Dupré, N.; Gaubicher, J.; Moreau, P.; Soudan, P.; Lestriez, B.; Guyomard, D., The failure mechanism of nano-sized Si-

based negative electrodes for lithium ion batteries. *Journal of Materials Chemistry* **2011,** *21* (17), 6201-6208.

86. Kalnaus, S.; Rhodes, K.; Daniel, C., A study of lithium ion intercalation induced fracture of silicon particles used as anode material in Li-ion battery. *Journal of Power Sources* **2011,** *196* (19), 8116-8124.
87. Liu, X. H.; Zhong, L.; Huang, S.; Mao, S. X.; Zhu, T.; Huang, J. Y., Size-Dependent Fracture of Silicon Nanoparticles During Lithiation. *ACS Nano* **2012,** *6* (2), 1522-1531.
88. Ma, Z.; Li, T.; Huang, Y. L.; Liu, J.; Zhou, Y.; Xue, D., Critical silicon-anode size for averting lithiation-induced mechanical failure of lithium-ion batteries. *RSC Advances* **2013,** *3* (20), 7398-7402.
89. Ryu, I.; Choi, J. W.; Cui, Y.; Nix, W. D., Size-dependent fracture of Si nanowire battery anodes. *Journal of the Mechanics and Physics of Solids* **2011,** *59* (9), 1717-1730.
90. Ye, J. C.; An, Y. H.; Heo, T. W.; Biener, M. M.; Nikolic, R. J.; Tang, M.; Jiang, H.; Wang, Y. M., Enhanced lithiation and fracture behavior of silicon mesoscale pillars via atomic layer coatings and geometry design. *Journal of Power Sources* **2014,** *248*, 447-456.
91. Jia, Z.; Liu, W. K., Analytical Model on Stress-Regulated Lithiation Kinetics and Fracture of Si-C Yolk-Shell Anodes for Lithium-Ion Batteries. *Journal of The Electrochemical Society* **2016,** *163* (6), A940-A946.
92. Zhao, K.; Pharr, M.; Hartle, L.; Vlassak, J. J.; Suo, Z., Fracture and debonding in lithium-ion batteries with electrodes of hollow core–shell nanostructures. *Journal of Power Sources* **2012,** *218*, 6-14.
93. Zhao, K.; Pharr, M.; Vlassak, J. J.; Suo, Z., Fracture of electrodes in lithium-ion batteries caused by fast charging. *Journal of Applied Physics* **2010,** *108* (7), 073517.
94. Wu, B.; Lu, W., Mechanical Modeling of Particles with Active Core–Shell Structures for Lithium-Ion Battery Electrodes. *The Journal of Physical Chemistry C* **2017,** *121* (35), 19022-19030.
95. Bhandakkar, T. K.; Gao, H., Cohesive modeling of crack nucleation under diffusion induced stresses in a thin strip: Implications on the critical size for flaw tolerant battery electrodes. *International Journal of Solids and Structures* **2010,** *47* (10), 1424-1434.
96. Zuo, P.; Zhao, Y.-P., Phase field modeling of lithium diffusion, finite deformation, stress evolution and crack propagation in lithium ion battery. *Extreme Mechanics Letters* **2016,** *9*, 467-479.
97. McDowell, M. T.; Ryu, I.; Lee, S. W.; Wang, C.; Nix, W. D.; Cui, Y., Studying the Kinetics of Crystalline Silicon Nanoparticle Lithiation with In Situ Transmission Electron Microscopy. *Advanced Materials* **2012,** *24* (45), 6034-6041.
98. Zhao, C.; Wada, T.; De Andrade, V.; Gürsoy, D.; Kato, H.; Chen-Wiegart, Y.-c. K., Imaging of 3D morphological evolution of nanoporous silicon anode in lithium ion

battery by X-ray nano-tomography. *Nano Energy* **2018,** *52*, 381-390.

99. Cho, J.-H.; Picraux, S. T., Silicon Nanowire Degradation and Stabilization during Lithium Cycling by SEI Layer Formation. *Nano Letters* **2014,** *14* (6), 3088-3095.
100. Shobukawa, H.; Alvarado, J.; Yang, Y.; Meng, Y. S., Electrochemical performance and interfacial investigation on Si composite anode for lithium ion batteries in full cell. *Journal of Power Sources* **2017,** *359*, 173-181.
101. Sun, G.; Sui, T.; Song, B.; Zheng, H.; Lu, L.; Korsunsky, A. M., On the fragmentation of active material secondary particles in lithium ion battery cathodes induced by charge cycling. *Extreme Mechanics Letters* **2016,** *9*, 449-458.
102. Pinson, M. B.; Bazant, M. Z., Theory of SEI Formation in Rechargeable Batteries: Capacity Fade, Accelerated Aging and Lifetime Prediction. *Journal of The Electrochemical Society* **2012,** *160* (2), A243-A250.
103. Chan, C. K.; Ruffo, R.; Hong, S. S.; Cui, Y., Surface chemistry and morphology of the solid electrolyte interphase on silicon nanowire lithium-ion battery anodes. *Journal of Power Sources* **2009,** *189* (2), 1132-1140.
104. Müller, S.; Pietsch, P.; Brandt, B.-E.; Baade, P.; De Andrade, V.; De Carlo, F.; Wood, V., Quantification and modeling of mechanical degradation in lithium-ion batteries based on nanoscale imaging. *Nature Communications* **2018,** *9* (1), 2340.
105. Kresse, G.; Furthmüller, J., Efficiency of ab-initio total energy calculations for metals and semiconductors using a plane-wave basis set. *Computational Materials Science* **1996,** *6* (1), 15-50.
106. Kresse, G.; Joubert, D., From ultrasoft pseudopotentials to the projector augmented-wave method. *Physical Review B* **1999,** *59* (3), 1758-1775.
107. Perdew, J. P.; Burke, K.; Ernzerhof, M., Generalized Gradient Approximation Made Simple. *Physical Review Letters* **1996,** *77* (18), 3865-3868.
108. Perdew, J. P.; Chevary, J. A.; Vosko, S. H.; Jackson, K. A.; Pederson, M. R.; Singh, D. J.; Fiolhais, C., Erratum: Atoms, molecules, solids, and surfaces: Applications of the generalized gradient approximation for exchange and correlation. *Physical Review B* **1993,** *48* (7), 4978-4978.
109. Johari, P.; Qi, Y.; Shenoy, V. B., The Mixing Mechanism during Lithiation of Si Negative Electrode in Li-Ion Batteries: An Ab Initio Molecular Dynamics Study. *Nano Letters* **2011,** *11* (12), 5494-5500.
110. Persson, K.; Sethuraman, V. A.; Hardwick, L. J.; Hinuma, Y.; Meng, Y. S.; van der Ven, A.; Srinivasan, V.; Kostecki, R.; Ceder, G., Lithium Diffusion in Graphitic Carbon. *The Journal of Physical Chemistry Letters* **2010,** *1* (8), 1176-1180.
111. Feng, H.-p.; Tang, L.; Zeng, G.-m.; Tang, J.; Deng, Y.-c.; Yan, M.; Liu, Y.-n.; Zhou, Y.-y.; Ren, X.-y.; Chen, S., Carbon-based core–shell nanostructured materials for electrochemical energy storage. *Journal of Materials Chemistry A* **2018,** *6* (17), 7310-7337.
112. Shenoy, V. B.; Johari, P.; Qi, Y., Elastic softening of amorphous and crystalline Li–Si Phases with increasing Li concentration: A first-principles study. *Journal of Power*

Sources **2010,** *195* (19), 6825-6830.

113. Wei, W.; Xu, K.; Liao, N.; Xue, W., Insight into Si/SiCO thin films anodes for lithium-ion batteries with high capacity and cycling stability. *Applied Materials Today* **2020,** *20*, 100773.
114. Concurrent Reaction and Plasticity During Initial Lithiation of Crystalline Silicon in Lithium-Ion Batteries. *ECS Meeting Abstracts* **2012**.
115. Bucci, G.; Swamy, T.; Chiang, Y.-M.; Carter, W. C., Modeling of internal mechanical failure of all-solid-state batteries during electrochemical cycling, and implications for battery design. *Journal of Materials Chemistry A* **2017,** *5* (36), 19422-19430.
116. Cui, W. C.; Wisnom, M. R.; Jones, M., A comparison of failure criteria to predict delamination of unidirectional glass/epoxy specimens waisted through the thickness. *Composites* **1992,** *23* (3), 158-166.
117. Benzeggagh, M. L.; Kenane, M., Measurement of mixed-mode delamination fracture toughness of unidirectional glass/epoxy composites with mixed-mode bending apparatus. *Composites Science and Technology* **1996,** *56* (4), 439-449.
118. Cho, I.; Choi, J.; Kim, K.; Ryou, M.-H.; Lee, Y. M., A comparative investigation of carbon black (Super-P) and vapor-grown carbon fibers (VGCFs) as conductive additives for lithium-ion battery cathodes. *RSC Advances* **2015,** *5* (115), 95073-95078.
119. Sethuraman, V. A.; Srinivasan, V.; Newman, J., Analysis of Electrochemical Lithiation and Delithiation Kinetics in Silicon. *J. Electrochem. Soc.* **2013,** *160* (2), A394-A403.
120. Doyle, M.; Newman, J.; Gozdz, A. S.; Schmutz, C. N.; Tarascon, J. M., Comparison of Modeling Predictions with Experimental Data from Plastic Lithium Ion Cells. *J. Electrochem. Soc.* **1996,** *143* (6), 1890-1903.
121. Wang, M.; Xiao, X.; Huang, X., Study of lithium diffusivity in amorphous silicon via finite element analysis. *J. Power Sources* **2016,** *307*, 77-85.
122. Wang, X.; Singh, S. S.; Ma, T.; Lv, C.; Chawla, N.; Jiang, H., Quantifying Electrochemical Reactions and Properties of Amorphous Silicon in a Conventional Lithium-Ion Battery Configuration. *Chem. Mater.* **2017,** *29* (14), 5831-5840.
123. Nyman, A.; Zavalis, T. G.; Elger, R.; Behm, M. r.; Lindbergh, G. r., Analysis of the Polarization in a Li-Ion Battery Cell by Numerical Simulations. *Journal of The Electrochemical Society* **2010,** *157* (11), A1236.
124. Tan, G.; Wu, F.; Yuan, Y.; Chen, R.; Zhao, T.; Yao, Y.; Qian, J.; Liu, J.; Ye, Y.; Shahbazian-Yassar, R.; Lu, J.; Amine, K., Freestanding three-dimensional core–shell nanoarrays for lithium-ion battery anodes. *Nature Communications* **2016,** *7* (1), 11774.
125. Wei Seh, Z.; Li, W.; Cha, J. J.; Zheng, G.; Yang, Y.; McDowell, M. T.; Hsu, P.-C.; Cui, Y., Sulphur–TiO2 yolk–shell nanoarchitecture with internal void space for long-cycle lithium–sulphur batteries. *Nature Communications* **2013,** *4* (1), 1331.
126. Li, J.; Liu, W.; Wan, Q.; Liu, F.; Li, X.; Qiao, Y.; Qu, M.; Peng, G., Facile Spray-Drying Synthesis of Dual-Shell Structure Si@SiOx@Graphite/Graphene as Stable Anode for Li-Ion Batteries. *Energy Technology* **2019,** *7* (9), 1900464.
127. Roy, P.; Srivastava, S. K., Nanostructured anode materials for lithium ion batteries.

Journal of Materials Chemistry A **2015,** *3* (6), 2454-2484.

128. Zhu, G.; Wang, L.; Lin, H.; Ma, L.; Zhao, P.; Hu, Y.; Chen, T.; Chen, R.; Wang, Y.; Tie, Z.; Liu, J.; Jin, Z., Walnut-Like Multicore–Shell MnO Encapsulated Nitrogen-Rich Carbon Nanocapsules as Anode Material for Long-Cycling and Soft-Packed Lithium-Ion Batteries. *Advanced Functional Materials* **2018,** *28* (18), 1800003.
129. Zhang, Y.; Guo, G.; Chen, C.; Jiao, Y.; Li, T.; Chen, X.; Yang, Y.; Yang, D.; Dong, A., An affordable manufacturing method to boost the initial Coulombic efficiency of disproportionated SiO lithium-ion battery anodes. *Journal of Power Sources* **2019,** *426*, 116-123.
130. Bucci, G.; Nadimpalli, S. P. V.; Sethuraman, V. A.; Bower, A. F.; Guduru, P. R., Measurement and modeling of the mechanical and electrochemical response of amorphous Si thin film electrodes during cyclic lithiation. *Journal of the Mechanics & Physics of Solids* **2014,** *62* (1), 276-294.
131. Lee, S. W.; McDowell, M. T.; Choi, J. W.; Cui, Y., Anomalous Shape Changes of Silicon Nanopillars by Electrochemical Lithiation. *Nano Letters* **2011,** *11* (7), 3034-3039.
132. Wang, H.; Nadimpalli, S. P. V.; Shenoy, V. B., Inelastic shape changes of silicon particles and stress evolution at binder/particle interface in a composite electrode during lithiation/delithiation cycling. *Extreme Mechanics Letters* **2016,** *9*.
133. McDowell, M. T.; Xia, S.; Zhu, T., The mechanics of large-volume-change transformations in high-capacity battery materials. *Extreme Mechanics Letters* **2016,** *9*, 480-494.
134. Qi, Y.; Guo, H.; Hector, L. G.; Timmons, A., Threefold Increase in the Young's Modulus of Graphite Negative Electrode during Lithium Intercalation. *J. Electrochem. Soc.* **2010,** *157* (5), A558-A566.
135. Srinivasan, V.; Newman, J., Design and Optimization of a Natural Graphite/Iron Phosphate Lithium-Ion Cell. *J. Electrochem. Soc.* **2004,** *151* (10), A1530-A1538.
136. Park, M.; Zhang, X.; Chung, M.; Less, G. B.; Sastry, A. M., A review of conduction phenomena in Li-ion batteries. *J. Power Sources* **2010,** *195* (24), 7904-7929.
137. Wang, H.; Nadimpalli, S. P. V.; Shenoy, V. B., Inelastic shape changes of silicon particles and stress evolution at binder/particle interface in a composite electrode during lithiation/delithiation cycling. *Extreme Mechanics Letters* **2016,** *9*, 430-438.
138. Louli, A. J.; Li, J.; Trussler, S.; Fell, C. R.; Dahn, J. R., Volume, Pressure and Thickness Evolution of Li-Ion Pouch Cells with Silicon-Composite Negative Electrodes. *Journal of The Electrochemical Society* **2017,** *164* (12), A2689-A2696.
139. Buiel, E., On the Reduction of Lithium Insertion Capacity in Hard-Carbon Anode Materials with Increasing Heat-Treatment Temperature. *Journal of The Electrochemical Society* **1998,** *145* (7), 2252.
140. Sethuraman, V. A.; Srinivasan, V.; Newman, J., Analysis of Electrochemical Lithiation and Delithiation Kinetics in Silicon. *Journal of The Electrochemical Society* **2012,** *160* (2), A394-A403.

141. Pan, K.; Zou, F.; Canova, M.; Zhu, Y.; Kim, J.-H., Systematic electrochemical characterizations of Si and SiO anodes for high-capacity Li-Ion batteries. *Journal of Power Sources* **2019,** *413*, 20-28.
142. Baggetto, L.; Oudenhoven, J. F. M.; van Dongen, T.; Klootwijk, J. H.; Mulder, M.; Niessen, R. A. H.; de Croon, M. H. J. M.; Notten, P. H. L., On the electrochemistry of an anode stack for all-solid-state 3D-integrated batteries. *Journal of Power Sources* **2009,** *189* (1), 402-410.
143. Yin, H.; Qi, H. J.; Fan, F.; Zhu, T.; Wang, B.; Wei, Y., Griffith Criterion for Brittle Fracture in Graphene. *Nano Letters* **2015,** *15* (3), 1918-1924.
144. Cui, Q.; Zhong, Y.; Pan, L.; Zhang, H.; Yang, Y.; Liu, D.; Teng, F.; Bando, Y.; Yao, J.; Wang, X., Recent Advances in Designing High-Capacity Anode Nanomaterials for Li-Ion Batteries and Their Atomic-Scale Storage Mechanism Studies. *Advanced Science* **2018,** *5* (7), 1700902.
145. Bohn, E.; Eckl, T.; Kamlah, M.; McMeeking, R., *A Model for Lithium Diffusion and Stress Generation in an Intercalation Storage Particle with Phase Change*. 2013; Vol. 160, p A1638-A1652.
146. Wan, T. H.; Ciucci, F., Continuum Level Transport and Electro-Chemo-Mechanics Coupling—Solid Oxide Fuel Cells and Lithium Ion Batteries. In *Electro-Chemo-Mechanics of Solids*, Bishop, S. R.; Perry, N. H.; Marrocchelli, D.; Sheldon, B. W., Eds. Springer International Publishing: Cham, 2017; pp 161-189.
147. Doyle, M.; Fuller, T. F.; Newman, J., Modeling of Galvanostatic Charge and Discharge of the Lithium/Polymer/Insertion Cell. *J. Electrochem. Soc.* **1993,** *140* (6), 1526-1533.
148. Kang, B.; Ceder, G., Battery materials for ultrafast charging and discharging. *Nature* **2009,** *458*, 190.
149. Wu, B.; Lu, W., Mechanical Modeling of Particles with Active Core-Shell Structures for Lithium-Ion Battery Electrodes. *J. Phys. Chem. C* **2017,** *121* (35).
150. Briscoe, B. J., Contact mechanics. *Tribology International* **1985,** *19* (2), 109-110.
151. Hardy, C.; Baronet, C. N.; Tordion, G. V., *The elasto-plastic indentation of a half-space by a rigid sphere*. p 451–462.
152. Vu-Quoc, L.; Zhang, X., An Elastoplastic Contact Force-Displacement Model in the Normal Direction: Displacement-Driven Version. *Proceedings Mathematical Physical & Engineering Sciences* **1999,** *455* (1991), 4013-4044.
153. Lin, L. P.; Lin, J. F., A New Method for Elastic-Plastic Contact Analysis of a Deformable Sphere and a Rigid Flat. *Journal of Tribology* **2006,** *128* (2), 221-229.
154. Yu, W.; Blanchard, J. P., An elastic-plastic indentation model and its solutions. *J. Mater. Res.* **1996,** *11* (9), 2358-2367.
155. Swadener, J. G.; George, E. P.; Pharr, G. M., The correlation of the indentation size effect measured with indenters of various shapes. *Journal of the Mechanics & Physics of Solids* **2002,** *50* (4), 681-694.
156. Alcal; #225; Giannakopoulos, A. E.; Suresh, S., Continuous measurements of load-

penetration curves with spherical microindenters and the estimation of mechanical properties. *J. Mater. Res.* **1998,** *13* (5), 1390-1400.

APPENDIX A: Governing Equations for Computational Model

The volume change (V/V_0) is related to the normalized Li concentration ($\bar{c}_s = c_s / c_{\mathrm{s,max}}$, where c is the concentration at any time point), $V/V_0 = 1 + \alpha\bar{c}$, where α is a coefficient related to the state of Li_xSi_y ($\alpha = 2.7$ when the Si is fully alloyed with Li, i.e. $Li_{15}Si_4$). The true strain induced by lithiation can be also expressed by the normalized Li concentration, $\bar{c}$, that is

$$\varepsilon_{ij}^{l} = \delta_{ij}\ln(1+\alpha\bar{c}_s)/3. \tag{A1}$$

The elastic strain is based on Hook's law, which can be written as

$$\varepsilon_{ij}^{e} = \left[(1+\nu)\sigma_{ij} - \nu\sigma_{kk}\delta_{ij}\right]/E, \tag{A2}$$

where the Young's modulus, *E* is related to the Li concentration. A linear relation based on the theory of Shenoy et al. [28] was applied in the present study,

$$E(\bar{c}) = E_0 + \bar{c}_s(E_1 - E_0) \tag{A3}$$

where $E_0 = 150\ \mathrm{GPa}$ corresponding to pure Si (i.e. $\bar{c} = 0$) and $E_0 = 50\ \mathrm{GPa}$ corresponding to fully lithiated Si (i.e. $\bar{c} = 1$). The increment plastic strain is a generalized form that

$$\mathrm{d}\varepsilon_{ij}^{p} = \lambda S_{ij}^{p}. \tag{A4}$$

The yield strength is also related to the Li-ion concentration and is assumed to be as a linear form, which can be expressed as

$$\sigma_y(\bar{c}_s) = \sigma_y^0 + \bar{c}_s(\sigma_y^1 - \sigma_y^0), \tag{A5}$$

where $\sigma_y^0 = 1.5\ \mathrm{GPa}$ and $\sigma_y^1 = 0.6\ \mathrm{GPa}$ for $\bar{c}_s = 0$ and $\bar{c}_s = 1$, respectively.

APPENDIX B: Theoretical Model Derivation

Single core-shell particle with large deformation

Use subscript 1 and 2 to denote the field of Si core and C shell, respectively (see Fig. 67(a)), and the stresses and displacement can be solved as the following expressions based on the derivation described in Eqs. (B2-B4) [149]

$$\sigma_{rr}^{cs}=\frac{2E_1E_2}{a^3}\frac{-\left[(\frac{b}{a})^3-1\right]\Omega_1\int_0^a cr^2\mathrm{d}r}{(\frac{b}{a})^3\left[E_1(1+\upsilon_2)+2E_2(1-2\upsilon_1)\right]+2\left[E_1(1-2\upsilon_2)-E_2(1-2\upsilon_1)\right]} \tag{B1}$$

where the radius of Si, $a=R$ and radius of core-shell particle, $b=R+t$. Then we can get the stress and displacement model shown in Eqs. (31)-(34).

In single core-shell particles, stress equilibriums in the Si core and C shell are given by

$$\frac{\partial\sigma_{rr}}{\partial r}+2\frac{\sigma_{rr}-\sigma_{\theta\theta}}{r}=0\,. \tag{B2}$$

The strain in the core-shell particle can be expressed as

$$\varepsilon_{rr}=\frac{du}{dr},\ \ \varepsilon_{\theta\theta}=\frac{u}{r}\,. \tag{B3}$$

Then the relations between stress and strain are

$$\begin{aligned}\sigma_{rr}&=\frac{E}{(1-\upsilon)(1-2\upsilon)}\left[(1-\upsilon)\varepsilon_{rr}+2\upsilon\varepsilon_{\theta\theta}-(1+\upsilon)\frac{\alpha c_s^*}{3}\right]\\ \sigma_{\theta\theta}&=\frac{E}{(1+\upsilon)(1-2\upsilon)}\left[\upsilon\varepsilon_{rr}+\varepsilon_{\theta\theta}-(1+\upsilon)\frac{\alpha c_s^*}{3}\right],\end{aligned} \tag{B4}$$

where the current concentration of Li-ion, $c_s^* = c_s - c_{s,0}$ is same to *c* with the assumption that the initial concentration is zero in the present study.

This model is based on the finite deformation assumption, but Si would produce relatively large deformation during lithiation as mentioned above. To take the large deformation into consideration, a finite difference method is used to calculate the specific values of stress and deformation at every time point. All functions are evolved with a time step Δt. At a given time *t*, Eqs. (31)-(34) and (B1) can be calculated and then the displacement results would be inserted back into these functions (displace *a* by $a + \Delta u_1$, *b* by $b + \Delta u_2$) to calculate the stress and deformation at time $t + \Delta t$.

Two contact core-shell particles

The core-shell particles are simplified as uniform particles (see Fig. 67(b)) and then the contact stress and stress within particles are calculated. For this contact model, there are three stages: elastic stage, plastic stage and the mixed elastic-plastic stage. The elastic stage is mainly described by Hertzian solution (Eqs. (B5-B9)) [150] and plastic stage is discussed based on several assumptions (Eqs. (B10-B14)) [151-155].

In elastic stage, it can be easily described by Hertzian solution, which points out that the maximum contact stress is

$$p_0 = \frac{3P}{2\pi w^2} = \frac{2wE^*}{\pi R^*}, \tag{B5}$$

where $E^* = \dfrac{E'}{2(1-\upsilon^2)}$ with $\dfrac{1}{E'} = \left(\dfrac{1}{E_1} + \dfrac{1}{E_2}\right)/2$, $R^* = \dfrac{b}{2}$, $P = \dfrac{4}{3}E^*\sqrt{b+u}\delta^{3/2}$ is the contact force, and $w = \sqrt{(b+u)\delta}$ is the radius of the contact area. The stress components induced by contact under the contact area within particles are

$$\begin{aligned} \frac{\sigma_{rr}}{p_0} = \frac{\sigma_{\theta\theta}}{p_0} &= -(1+\upsilon)\left[1-(z/w)\tan^{-1}(w/z)\right] + \frac{1}{2}(1+z^2/w^2)^{-1} \\ \frac{\sigma_{zz}}{p_0} &= -(1+z^2/a^2)^{-1} \end{aligned} \qquad \text{(B6)}$$

where *z* represents the depth from the contact point in particle. The range of elastic stage is defined to be from the initiation of contact to the initiation of yield ($\delta = \delta_y$). Since the plasticity of C shell is not considered, this yield initiation is mainly related to Si core. Define maximum proportion of stress field in particle,

$$f(\upsilon) = \max_{z \in b+u}\left\{-(1+\upsilon)\left[1-(z/w)\tan^{-1}(w/z)\right] + \frac{1}{2}(1+z^2/w^2)^{-1}\right\}, \qquad \text{(B7)}$$

then then maximum stress in the particle is

$$\sigma_{rr,\max} = \sigma_{\theta\theta,\max} = -f(\upsilon)p_0 = -\frac{3P}{2\pi w^2}f(\upsilon). \qquad \text{(B8)}$$

So, when then maximum stress within particles reaches the yield stress, we can get the end-point of elastic stage which is also the initiation of mixed elastic-plastic stage as

$$\delta_y = \frac{r}{f(\upsilon)}\left(\frac{\pi\sigma_y}{2E^*}\right)^2. \qquad \text{(B9)}$$

The corresponding contact radius is $w = \sqrt{(b+u)\delta_y}$.

Before discussing the mixed elastic-plastic stage, it is easier to describe the plastic behavior. There are several assumptions which have been demonstrated to be right when discussing plastic stage. One is that the stress p within the contact area is uniform. This leads to the contact force written as

$$P = p\pi w^2 . \tag{B10}$$

The upper and lower bounds of p are defined as σ_y and $2.8\sigma_y$ according to the previous studies [151, 152]. Another is that the contact force is linearly related to the displacement, δ. Therefore, the contact area can be expressed in terms of δ as

$$w^2 = 2r\delta + \hbar , \tag{B11}$$

where $\hbar$ is a constant and can be written as

$$\hbar = w_p^2 - 2r\delta_p . \tag{B12}$$

Then we can define the initiation of the plastic stage as

$$\delta_p = \left(p / \sigma_y \right)^2 \delta_y . \tag{B13}$$

And the radius of contact area in plastic stage is

$$w_p = r \frac{3\pi}{4} \frac{p_0}{E^*} . \tag{B14}$$

As for the mixed elastic-plastic stage, cubic Hermite polynomials are used to enforce the continuity between the end of elastic stage and the initiation of plastic stage.

Then coupling the stress and displacement models of single core-shell particle with the elastic-plastic contact model, the contact stress of two core-shell particles can be expressed theoretically. There are also three stages divided by two specific displacement, δ_y and δ_p (see Fig. 67(c)). The methodology to define these two values has been proposed in above discussions, i.e. Eqs. (B9) and (B13). In stage A (elastic stage), the contact stress on C shell surface can be expressed using Eq. (B4), then stresses induced by contact in Si core can be written out by Eq. (B6). The total stress at Si-C interface is composed of this contact induced stress and diffusion induced stress defined by Eq. (31). In stage C (plastic stage), first calculate the contact induced stress over the Si core surface by the definition that $\sigma_y \le p \le 2.8\sigma_y$. Here p is assumed to be $2.2\sigma_y$ according to the Meyer's hardness of elastic-perfectly plastic materials [156]. Then the stress at the Si-C interface can be express as the summation of interface stress of single core-shell particle, σ_r^{cs} and contact induced stress, p with the assumption that there's no coupling effect of these two components on each other. Finally, using Eq. (B6) to inversely calculate the contact stress at C-C contact area. Stage B (mixed elastic-plastic stage) can be computed by cubic Hermite polynomials mentioned above.

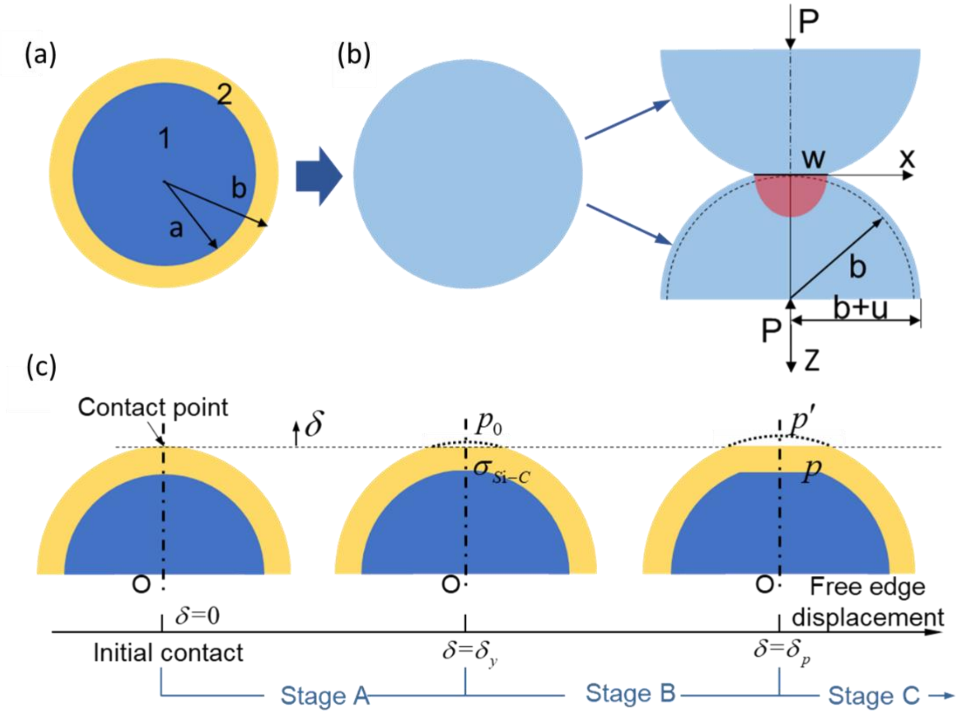

Figure 67 Schematic of theoretical model components**.** This core-shell particle contact

theoretical model contains (a) single core-shell particle free expansion model; (b) elastic-plastic contact model; (c) elastic-plastic contact model for swelling core-shell particle during first charging process. (only half particle is shown in the figure due to the symmetry of the contact model)

APPENDIX C: Model Validation Using Various OCP Inputs

We compared OCP curves from several different references [138, 140-142] and found that the OCP curves of Si show small difference due to the variety of material samples and the difference of testing methodologies. (Fig. 68 (a))

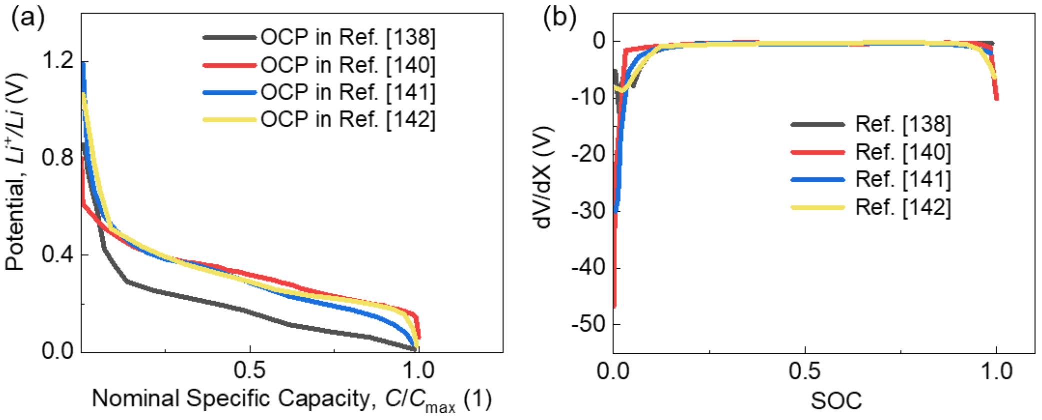

Figure 68 (a) OCP curves from different references [138, 140-142] and (b) the corresponding differential curve with respect to SOC

Thus, we performed a parametric study of various OCP curves based on Structure 1 (core-shell structure) as the representative, and the results of these four models are shown as follows. The difference of hoop stress in C shell and normal stress at the Si/C interface among four models is very small compared to the difference among different configurations (determined in the manuscript), which is neglectable (Fig 69 (a) and (c)). This is because the stress is induced by the deformation (Fig. 69 (e)) governed by the Δ SOC (Fig. 9 (f)), and both of them show high consistency among different models. Consequently, the fracture ERRs of C shell and debonding ERRs of the Si/C interface among the four models are also very close (Fig. 69 (b) and (d)). The ERR is mainly related to the stress and Young's modulus of materials, as described in Eqs. (45) and (46) in *Section 4.2.5*. Since the stress values of the four models are almost the same, thus, the difference of the ERR can be attributed to the difference of Young's modulus due to the Li^+ concentration discrepancy (Fig. 70). It indicates that the difference of Li^+ concentration in the Si core starts from the beginning of charging. This is because the initial OCP values of Si and C in all the models are set as the same (0.8 V) to meet the continuous condition at the Si/C interface for each model, which leads to the difference in initial distribution of Li^+ concentration in the Si core due to the difference of Si OCP curves. Due to this initial difference, the Li^+ concentration evolutions among four models keep the local difference in the whole charging/discharging process. However, the divergence of the concentration distribution does not affect the overall SOC change, which is trivial in the analysis of mechanical failure and general capacity.

According to the fact that the overall SOC change during the charging/discharging process is almost the same (Fig. 69 (f)), which further leads to a similar condition of stress and fracture, we finally conclude that the difference of Si OCP is not the dominant issue in our study. We further demonstrate this by calculating the derivative of OCP with respect to SOC, which is one of the dominant terms in the governing equations of Li flux (Eqs. (17)-(18) in the *Section 3.1.3*) (Fig. 68 (b)). We can see that the difference only occurs at the beginning values of SOC, considering that the process in our study is within SOC values of 0~0.5.

In conclusion, little difference can be found in terms of these variables concerned in our study using the four models shown above with various OCP curves of Si. Thus, we select one OCP curve from Ref. [138] as the input parameter for Si.

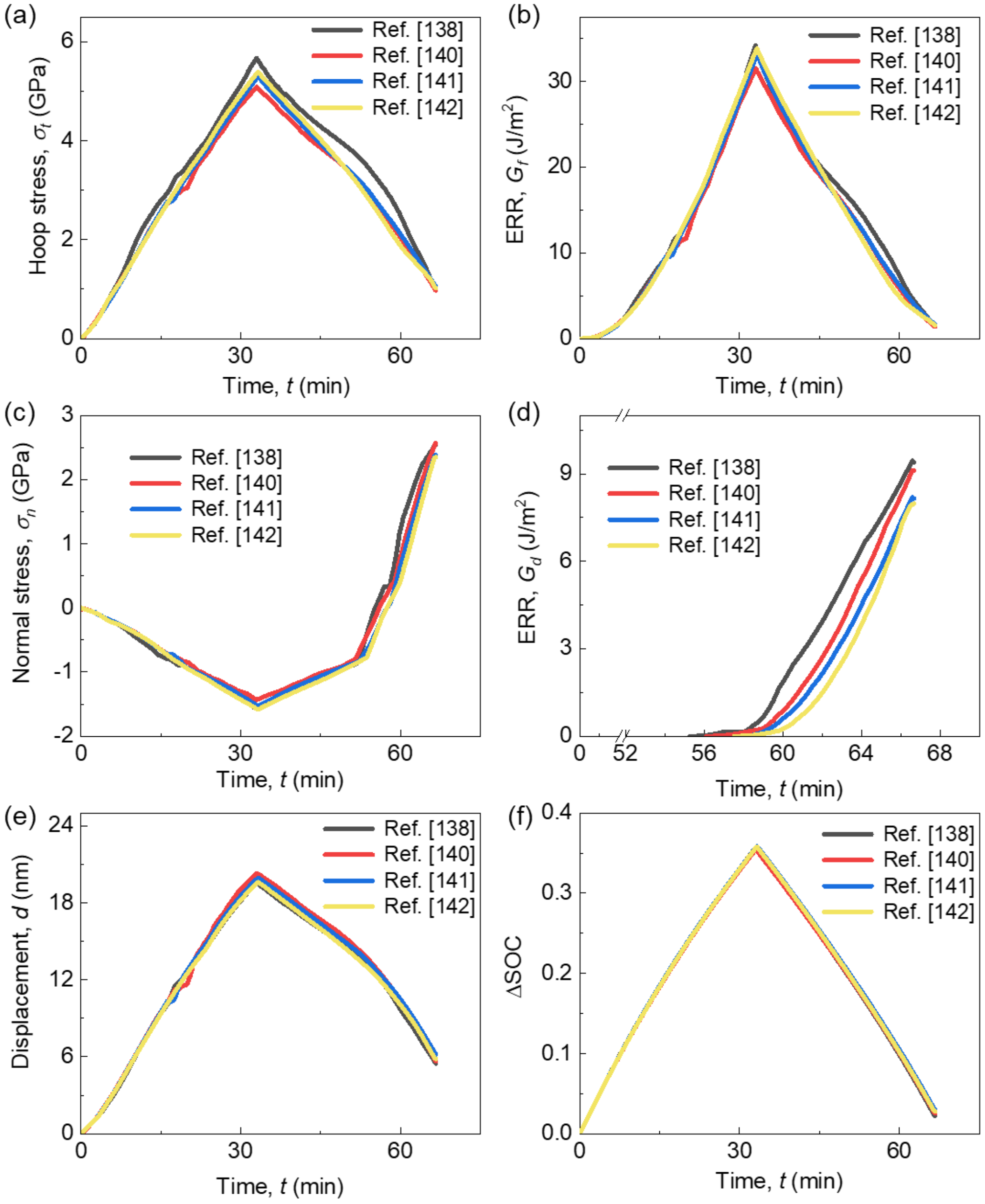

Figure 69 (a) Average hoop stress in the C shell, (b) C shell fracture ERR, (c) Maximum normal stress at the Si/C interface, (d) interface debonding ERR, (e) Maximum displacement, and (f) SOC change among four models during one charging/discharging cycle

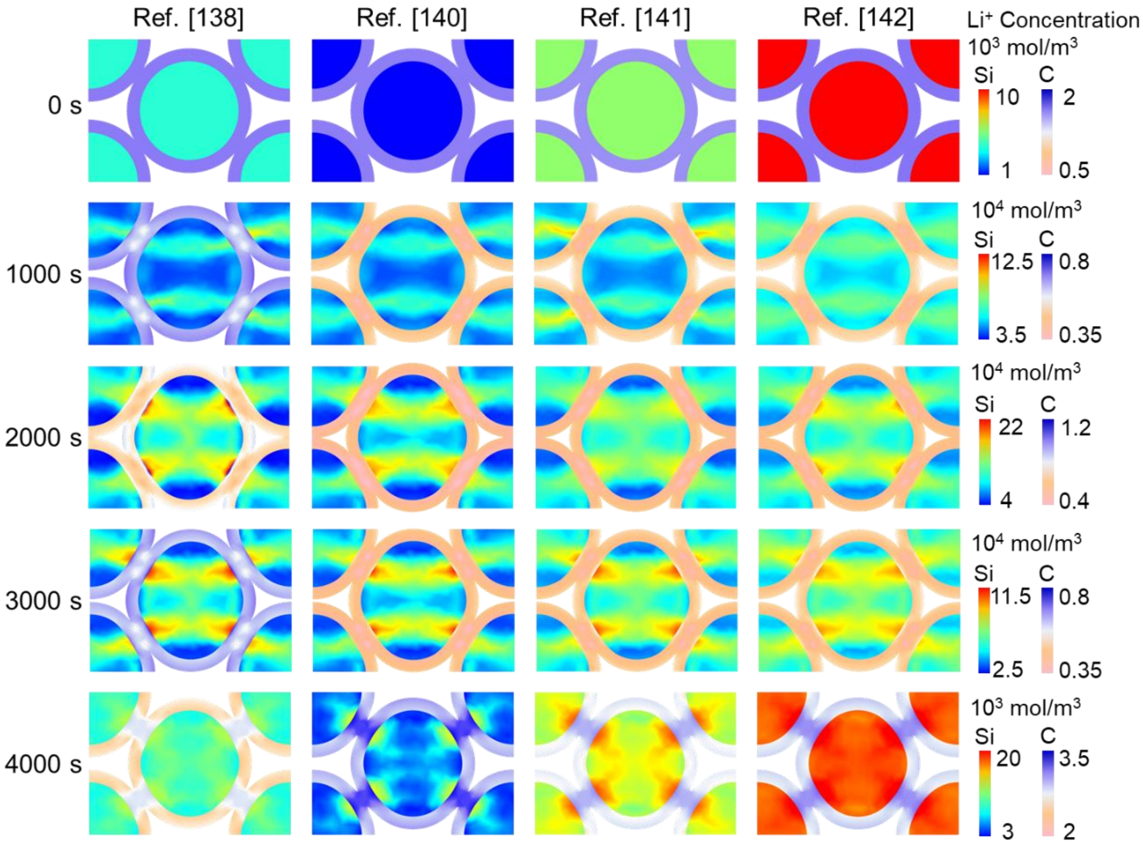

Figure 70 Li^+ concentration distribution in the four models at five specific time point (0 s: initial point, 1000 s: half of the charging stage, 2000 s: end of the charging (start of the discharging), 3000 s: half of the discharging stage, 4000 s: end of the discharging)

APPENDIX D: Homogenization of Si-C Compound Particle

The electrochemical and mechanical parameters of Si-C compound particle are homogenized in Chapter 5 to simplify the multiscale model, as shown in Figure 57.

The density, maximum Li-ion concentration, diffusivity and young's modulus here are homogenized simply as

$$E_{Si-C} = \lambda E_C + (1-\lambda) E_{Si} \tag{D1}$$

$$\rho_{Si-C} = \lambda \rho_C + (1-\lambda) \rho_{Si} \tag{D2}$$

$$D_{Si-C} = \lambda D_C + (1-\lambda) D_{Si} \tag{D3}$$

$$c_{Si-C}^{\max} = \lambda c_C^{\max} + (1-\lambda) c_{Si}^{\max} \tag{D4}$$

The partial molar volume of Si-C compound particles is given by

$$\Omega_{Si-C} = \frac{\left(\Omega_{Si} \lambda \Delta c_{s,Si} + \Omega_C \left(1-\lambda\right) \Delta c_{s,C}\right)}{\Delta c_s} \tag{D5}$$

When assuming it to be a linear constant value, Eq. (5) can be transferred into

$$\Omega_{Si-C} = \frac{\left(\Omega_C \lambda c_{s,C}^{\max} + \Omega_{Si} \left(1-\lambda\right) c_{s,Si}^{\max}\right)}{c_{s,Si-C}^{\max}} \tag{D6}$$

APPENDIX E: Effects Study of Si/C Zone Shape and Amounts

To investigate the effects of Si-C zone shape and amounts, a series of pre-simulation works have been done before the formal simulation work in Chapter 5. Firstly, the shape effect was studied, as shown in Figure 71. Three shapes, i.e. rectangle, circle, and ellipse, were considered. The area of these three shapes were the same so that the Si proportion in total would be the same. All the other parameters were set to be the same as well. The voltage and Li-ion concentration profiles show that the geometrical shape of the Si-C zone has little effect on electrochemical behaviors (Figures 71 (b) and (c)). The maximum deformation shows the difference among different shapes while the average deformation is the same. Von Mises stress in circle shape configuration is the lowest which may be attributed to less stress concentration. Based on all the above factors, the circle shape was finally selected.

Then, the effects of the amount of Si-C zones were studied with the circle shape, as shown in Figure 72. The total areas of different amounts of Si-C zones were the same to ensure the Si proportion same in total. All the other parameters were set to be the same as well. The voltage and Li-ion concentration profiles show that the amounts of Si-C zone have little effect on electrochemical behaviors (Figures 72 (b) and (c)). The maximum deformation would decrease with the increasing amount of Si-C zones and approach to the average deformation. Von Mises stress would also decrease with the amount of Si-C zones increasing. It implies that more amount of Si-C zones would generate a more accurate result and our convergent study shows that four circles would be confident enough to have an accurate result.

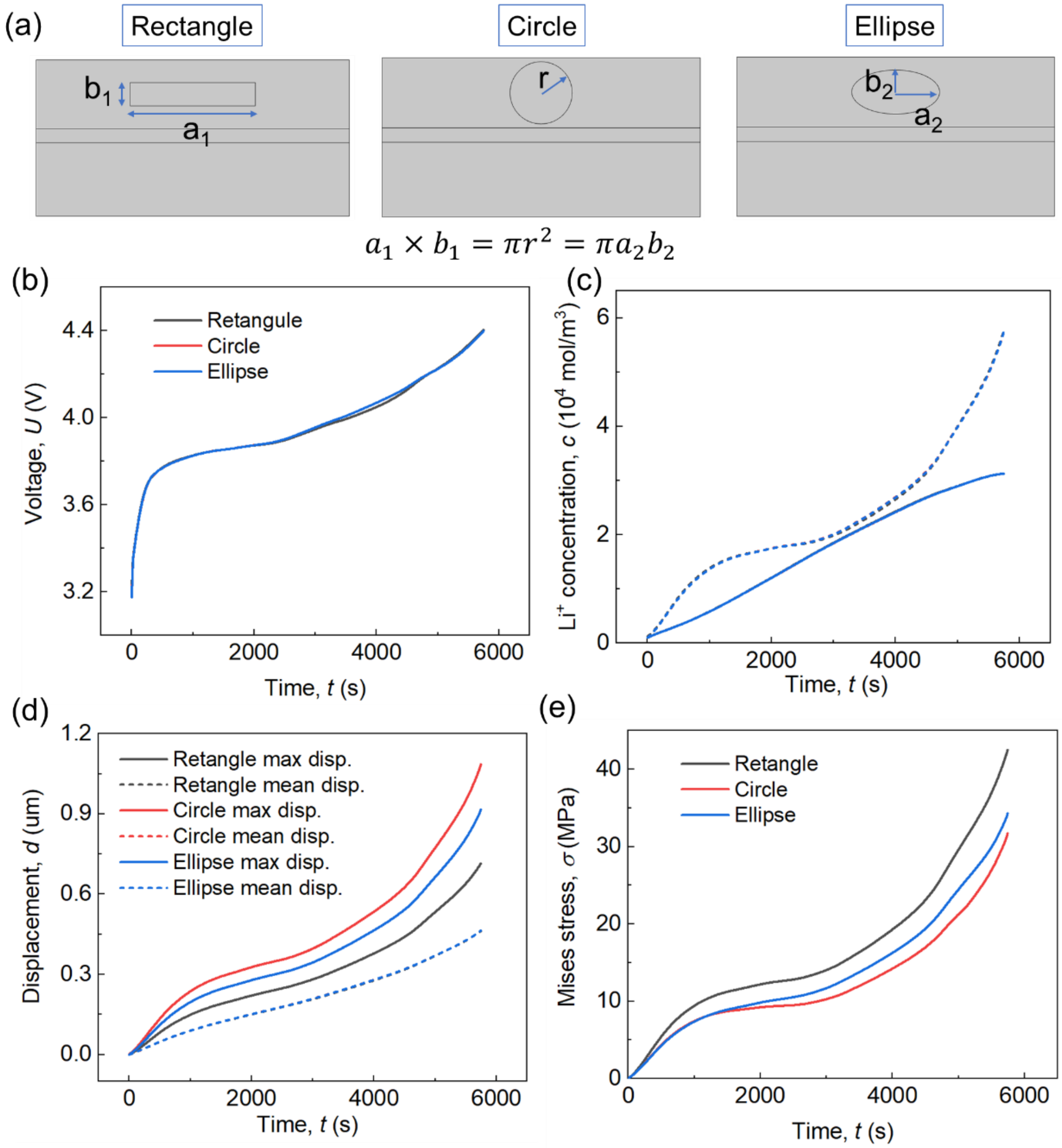

Figure 71 Pre-simulation about the geometrical shape effects. (a) different shape configurations; (b) voltage comparison; (c) Li-ion concentration comparison in Si-C zone (dash line) and C zone (solid line); (d) deformation comparison; (e) stress comparison

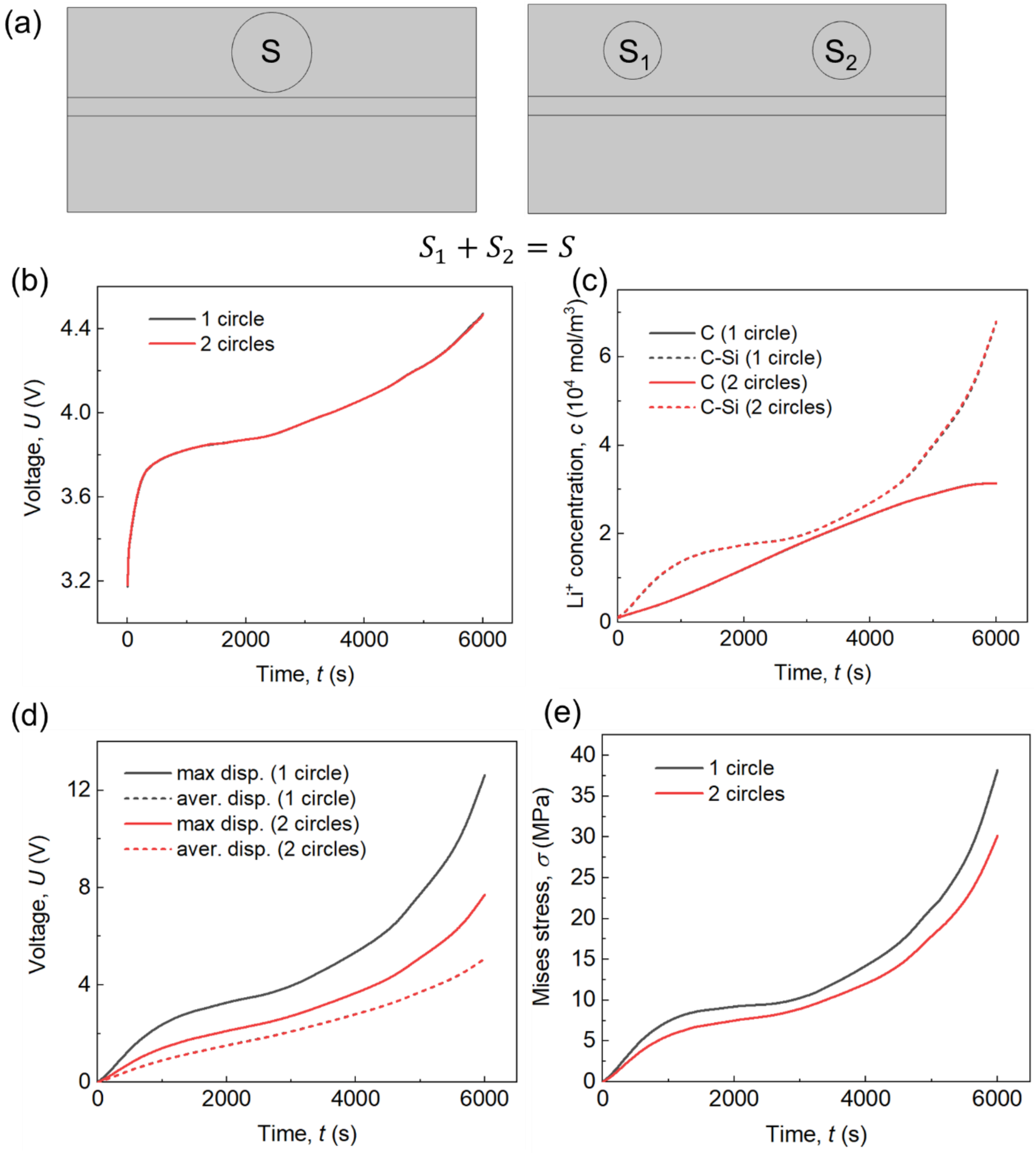

Figure 72 Pre-simulation about the effects of Si-C zone amounts. (a) different Si-C zone amounts; (b) voltage comparison; (c) Li-ion concentration comparison in Si-C zone and C zone; (d) deformation comparison; (e) stress comparison

APPENDIX F: Multiphysics-Multiscale Model Details

- Electrochemical model in microscale

As for the weak form of the diffusion model, a particle with radius of r_p, has the following expression:

$$\begin{aligned}&\int_0^{r_p}\left(-r^2\frac{\partial c_s}{\partial t}\hat{c}_s+r^2A\frac{\partial c_s}{\partial r}\frac{\partial \hat{c}_s}{\partial r}+r^2B\frac{\partial \sigma_h}{\partial r}\frac{\partial \hat{c}_s}{\partial r}\right)\mathrm{d}r\\&=r^2\hat{c}_s\left(A\frac{\partial c_s}{\partial r}+A\frac{\partial \sigma_h}{\partial r}\right)_0^{r_p}\end{aligned}\tag{F1}$$

where

$$A=\frac{D_0F}{RT}\left(\frac{c_s}{c_{s,\max}}\right)\left(c_{s,\max}-c_s\right)\frac{\partial E_{ref}}{\partial c_s}\tag{F2}$$

$$B=\frac{D_0}{RT}\left(\frac{c_s}{c_{s,\max}}\right)\left(c_{s,\max}-c_s\right)\Omega\tag{F3}$$

For C particles, the parameters needed in Eq (F1)-(F3) should be from C properties while for Si-C particles, they should be from the homogenized Si-C properties.

- Electrochemical model in macroscale

The effective electrical conductivity used in the governing equation of current density and Li-ion flux density can be written as:

$$\kappa_e^{eff}=\kappa_e\varepsilon_e^{1.5}\tag{F4}$$

$$\kappa_s^{eff}=\kappa_s\varepsilon_s^{1.5}\tag{F5}$$

And the effective Li-ion diffusion coefficient of the liquid phase is

$$D_e^{eff}=D_e\varepsilon_e^{1.5}\tag{F6}$$

The intercalation current density is described in *Chapter 3, Section 3.1.2*

APPENDIX G: PERMISSION LETTERS

Here are the permission letters for reuse the contents from my previous publications.

(See the following pages)

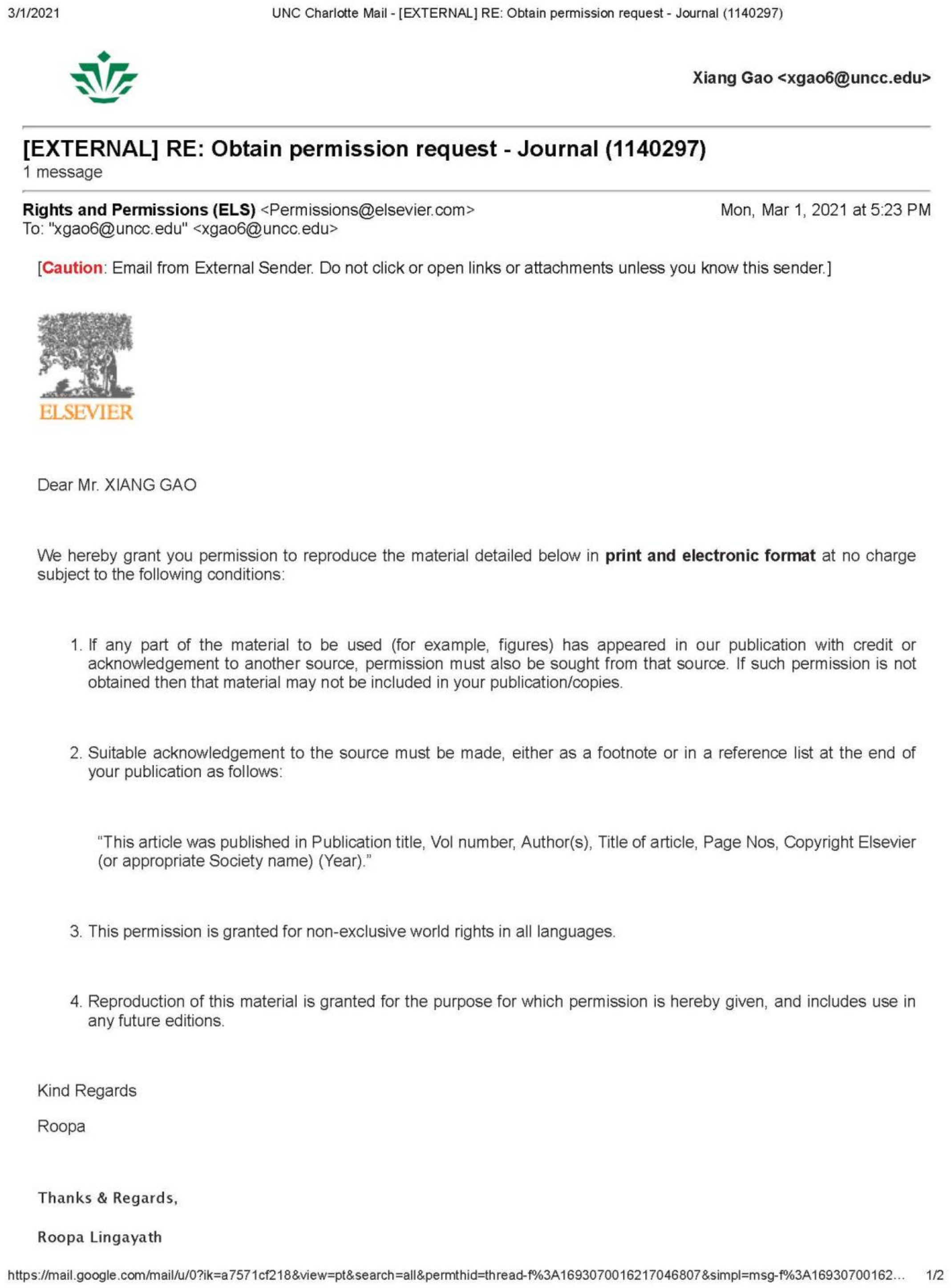

3/1/2021 UNC Charlotte Mail - [EXTERNAL] RE: Obtain permission request - Journal (1140297)

Xiang Gao <xgao6@uncc.edu>

[EXTERNAL] RE: Obtain permission request - Journal (1140297)

1 message

Rights and Permissions (ELS) <Permissions@elsevier.com> Mon, Mar 1, 2021 at 5:23 PM
To: "xgao6@uncc.edu" <xgao6@uncc.edu>

[**Caution**: Email from External Sender. Do not click or open links or attachments unless you know this sender.]

Dear Mr. XIANG GAO

We hereby grant you permission to reproduce the material detailed below in **print and electronic format** at no charge subject to the following conditions:

1. If any part of the material to be used (for example, figures) has appeared in our publication with credit or acknowledgement to another source, permission must also be sought from that source. If such permission is not obtained then that material may not be included in your publication/copies.

2. Suitable acknowledgement to the source must be made, either as a footnote or in a reference list at the end of your publication as follows:

   "This article was published in Publication title, Vol number, Author(s), Title of article, Page Nos, Copyright Elsevier (or appropriate Society name) (Year)."

3. This permission is granted for non-exclusive world rights in all languages.

4. Reproduction of this material is granted for the purpose for which permission is hereby given, and includes use in any future editions.

Kind Regards

Roopa

Thanks & Regards,

Roopa Lingayath

https://mail.google.com/mail/u/0?ik=a7571cf218&view=pt&search=all&permthid=thread-f%3A1693070016217046807&simpl=msg-f%3A16930700162… 1/2

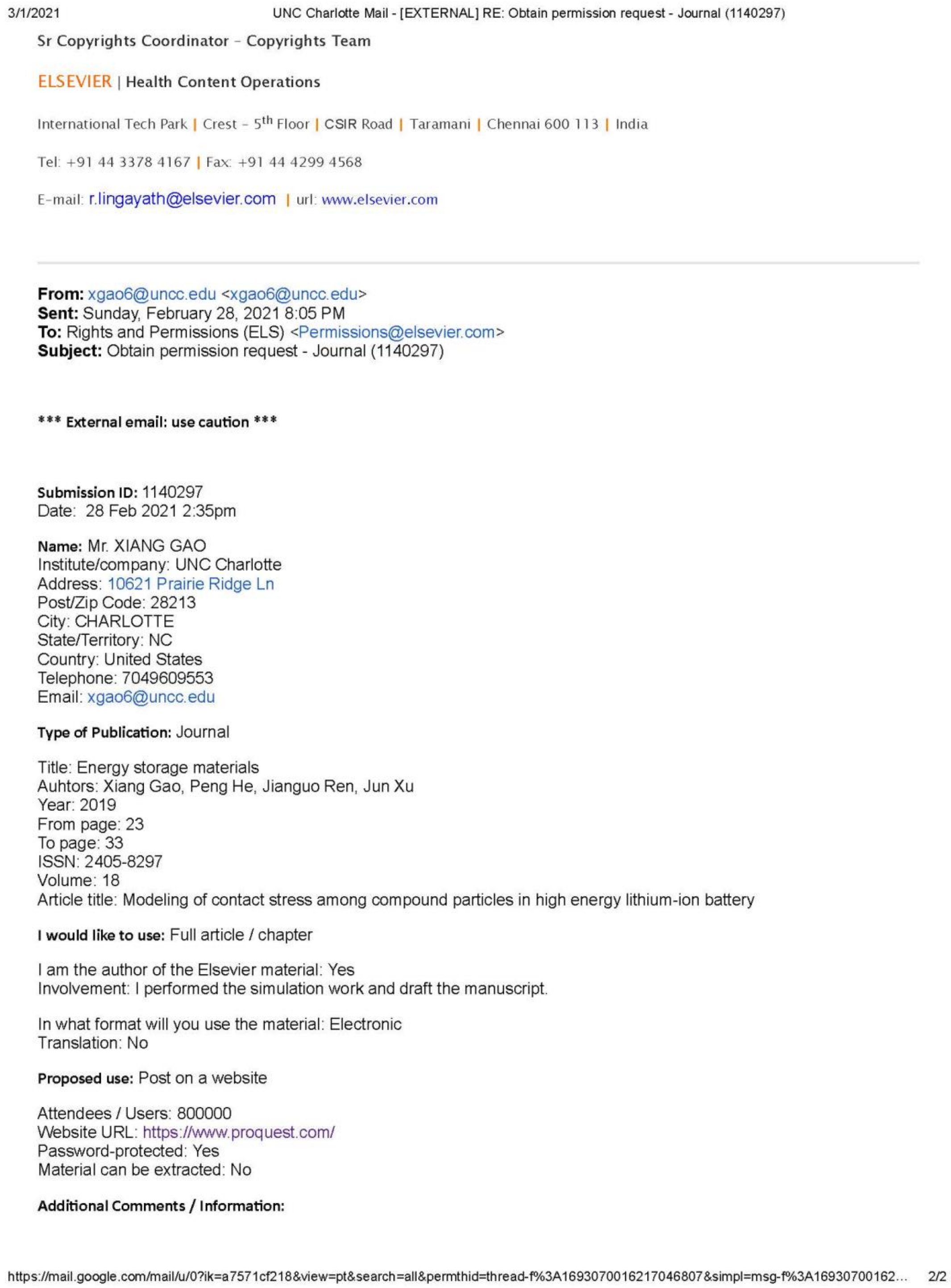

3/1/2021 UNC Charlotte Mail - [EXTERNAL] RE: Obtain permission request - Journal (1140297)

Sr Copyrights Coordinator – Copyrights Team

ELSEVIER | Health Content Operations

International Tech Park | Crest – 5th Floor | CSIR Road | Taramani | Chennai 600 113 | India

Tel: +91 44 3378 4167 | Fax: +91 44 4299 4568

E-mail: r.lingayath@elsevier.com | url: www.elsevier.com

From: xgao6@uncc.edu <xgao6@uncc.edu>
Sent: Sunday, February 28, 2021 8:05 PM
To: Rights and Permissions (ELS) <Permissions@elsevier.com>
Subject: Obtain permission request - Journal (1140297)

***** External email: use caution *****

Submission ID: 1140297
Date: 28 Feb 2021 2:35pm

Name: Mr. XIANG GAO
Institute/company: UNC Charlotte
Address: 10621 Prairie Ridge Ln
Post/Zip Code: 28213
City: CHARLOTTE
State/Territory: NC
Country: United States
Telephone: 7049609553
Email: xgao6@uncc.edu

Type of Publication: Journal

Title: Energy storage materials
Auhtors: Xiang Gao, Peng He, Jianguo Ren, Jun Xu
Year: 2019
From page: 23
To page: 33
ISSN: 2405-8297
Volume: 18
Article title: Modeling of contact stress among compound particles in high energy lithium-ion battery

I would like to use: Full article / chapter

I am the author of the Elsevier material: Yes
Involvement: I performed the simulation work and draft the manuscript.

In what format will you use the material: Electronic
Translation: No

Proposed use: Post on a website

Attendees / Users: 800000
Website URL: https://www.proquest.com/
Password-protected: Yes
Material can be extracted: No

Additional Comments / Information:

https://mail.google.com/mail/u/0?ik=a7571cf218&view=pt&search=all&permthid=thread-f%3A1693070016217046807&simpl=msg-f%3A16930700162… 2/2

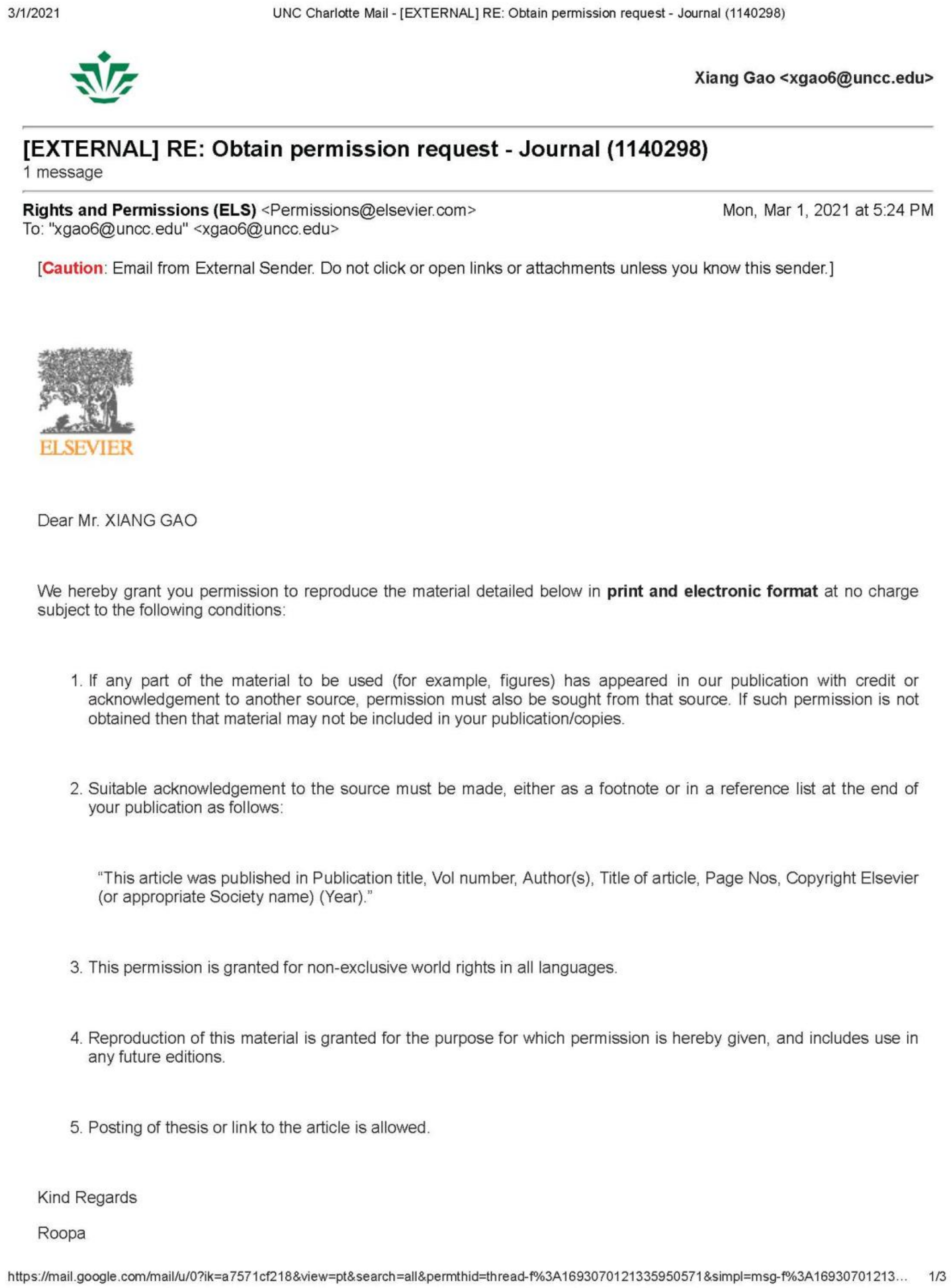

Xiang Gao <xgao6@uncc.edu>

[EXTERNAL] RE: Obtain permission request - Journal (1140298)

1 message

Rights and Permissions (ELS) <Permissions@elsevier.com> Mon, Mar 1, 2021 at 5:24 PM
To: "xgao6@uncc.edu" <xgao6@uncc.edu>

[**Caution**: Email from External Sender. Do not click or open links or attachments unless you know this sender.]

ELSEVIER

Dear Mr. XIANG GAO

We hereby grant you permission to reproduce the material detailed below in **print and electronic format** at no charge subject to the following conditions:

1. If any part of the material to be used (for example, figures) has appeared in our publication with credit or acknowledgement to another source, permission must also be sought from that source. If such permission is not obtained then that material may not be included in your publication/copies.

2. Suitable acknowledgement to the source must be made, either as a footnote or in a reference list at the end of your publication as follows:

   "This article was published in Publication title, Vol number, Author(s), Title of article, Page Nos, Copyright Elsevier (or appropriate Society name) (Year)."

3. This permission is granted for non-exclusive world rights in all languages.

4. Reproduction of this material is granted for the purpose for which permission is hereby given, and includes use in any future editions.

5. Posting of thesis or link to the article is allowed.

Kind Regards

Roopa

Thanks & Regards,

Roopa Lingayath

Sr Copyrights Coordinator – Copyrights Team

ELSEVIER | Health Content Operations

International Tech Park | Crest – 5th Floor | CSIR Road | Taramani | Chennai 600 113 | India

Tel: +91 44 3378 4167 | Fax: +91 44 4299 4568

E-mail: r.lingayath@elsevier.com | url: www.elsevier.com

From: xgao6@uncc.edu <xgao6@uncc.edu>
Sent: Sunday, February 28, 2021 8:09 PM
To: Rights and Permissions (ELS) <Permissions@elsevier.com>
Subject: Obtain permission request - Journal (1140298)

***** External email: use caution *****

Submission ID: 1140298
Date: 28 Feb 2021 2:39pm

Name: Mr. XIANG GAO
Institute/company: UNC Charlotte
Address: 10621 Prairie Ridge Ln
Post/Zip Code: 28213
City: CHARLOTTE
State/Territory: NC
Country: United States
Telephone: 7049609553
Email: xgao6@uncc.edu

Type of Publication: Journal

Title: Journal of Power Sources
Auhtors: Xiang Gao, Wenquan Liu, Jun Xu
Year: 2020
From page: 227501
To page: 227501
ISSN: 0378-7753
Volume: 449
Article title: Modeling framework for multiphysics-multiscale behavior of Si–C composite anode.

I would like to use: Full article / chapter

I am the author of the Elsevier material: Yes
Involvement: I performed the simulation work and draft the manuscript.

In what format will you use the material: Electronic
Translation: No

Proposed use: Post on a website

3/1/2021 UNC Charlotte Mail - [EXTERNAL] RE: Obtain permission request - Journal (1140298)

Attendees / Users: 800000
Website URL: https://www.proquest.com/
Password-protected: Yes
Material can be extracted: No

Additional Comments / Information:

https://mail.google.com/mail/u/0?ik=a7571cf218&view=pt&search=all&permthid=thread-f%3A1693070121335950571&simpl=msg-f%3A16930701213… 3/3

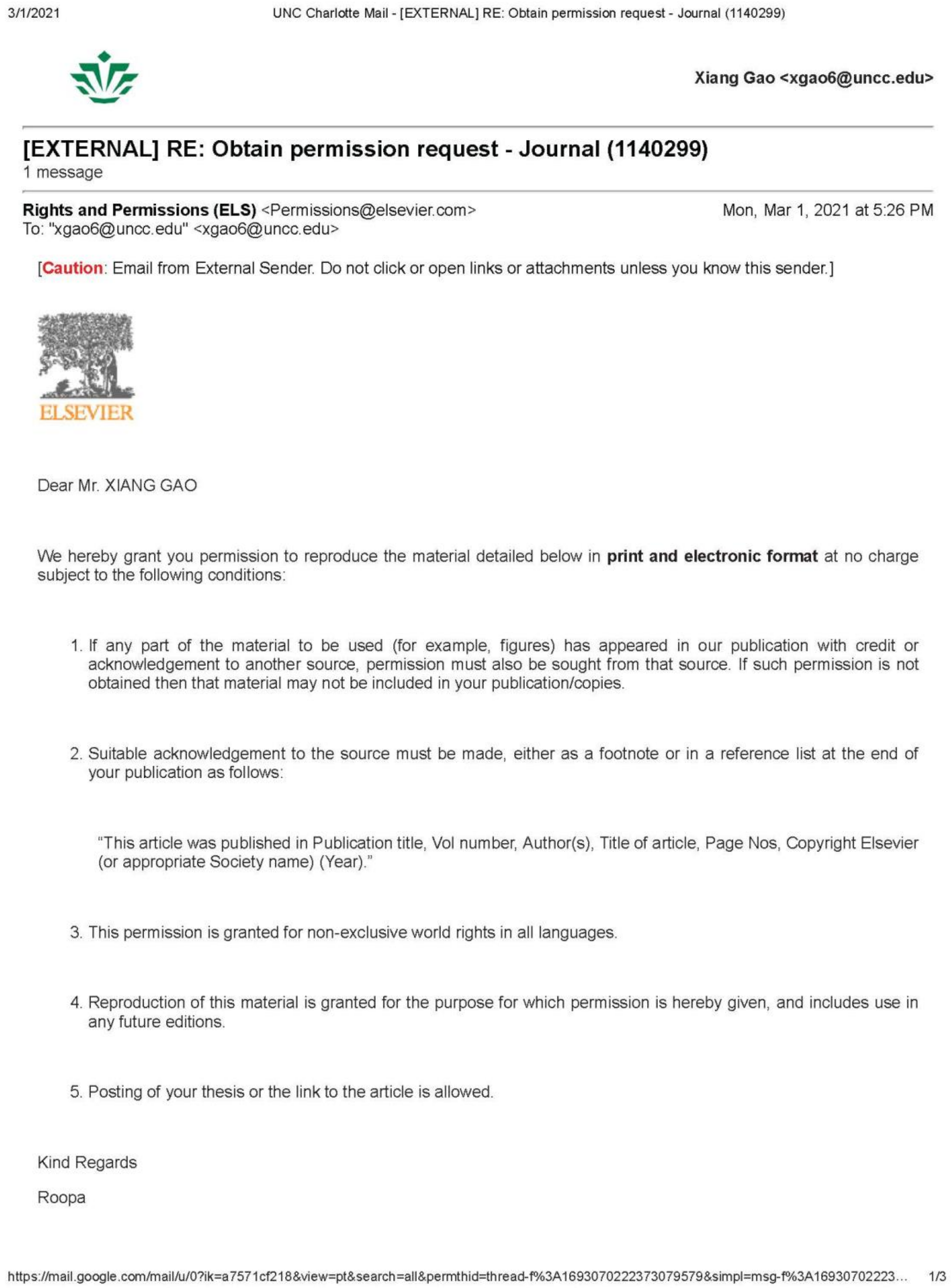

3/1/2021 UNC Charlotte Mail - [EXTERNAL] RE: Obtain permission request - Journal (1140299)

Xiang Gao <xgao6@uncc.edu>

[EXTERNAL] RE: Obtain permission request - Journal (1140299)

1 message

Rights and Permissions (ELS) <Permissions@elsevier.com> Mon, Mar 1, 2021 at 5:26 PM
To: "xgao6@uncc.edu" <xgao6@uncc.edu>

[**Caution**: Email from External Sender. Do not click or open links or attachments unless you know this sender.]

ELSEVIER

Dear Mr. XIANG GAO

We hereby grant you permission to reproduce the material detailed below in **print and electronic format** at no charge subject to the following conditions:

1. If any part of the material to be used (for example, figures) has appeared in our publication with credit or acknowledgement to another source, permission must also be sought from that source. If such permission is not obtained then that material may not be included in your publication/copies.
2. Suitable acknowledgement to the source must be made, either as a footnote or in a reference list at the end of your publication as follows:

   "This article was published in Publication title, Vol number, Author(s), Title of article, Page Nos, Copyright Elsevier (or appropriate Society name) (Year)."

3. This permission is granted for non-exclusive world rights in all languages.
4. Reproduction of this material is granted for the purpose for which permission is hereby given, and includes use in any future editions.
5. Posting of your thesis or the link to the article is allowed.

Kind Regards

Roopa

https://mail.google.com/mail/u/0?ik=a7571cf218&view=pt&search=all&permthid=thread-f%3A1693070222373079579&simpl=msg-f%3A16930702223… 1/3

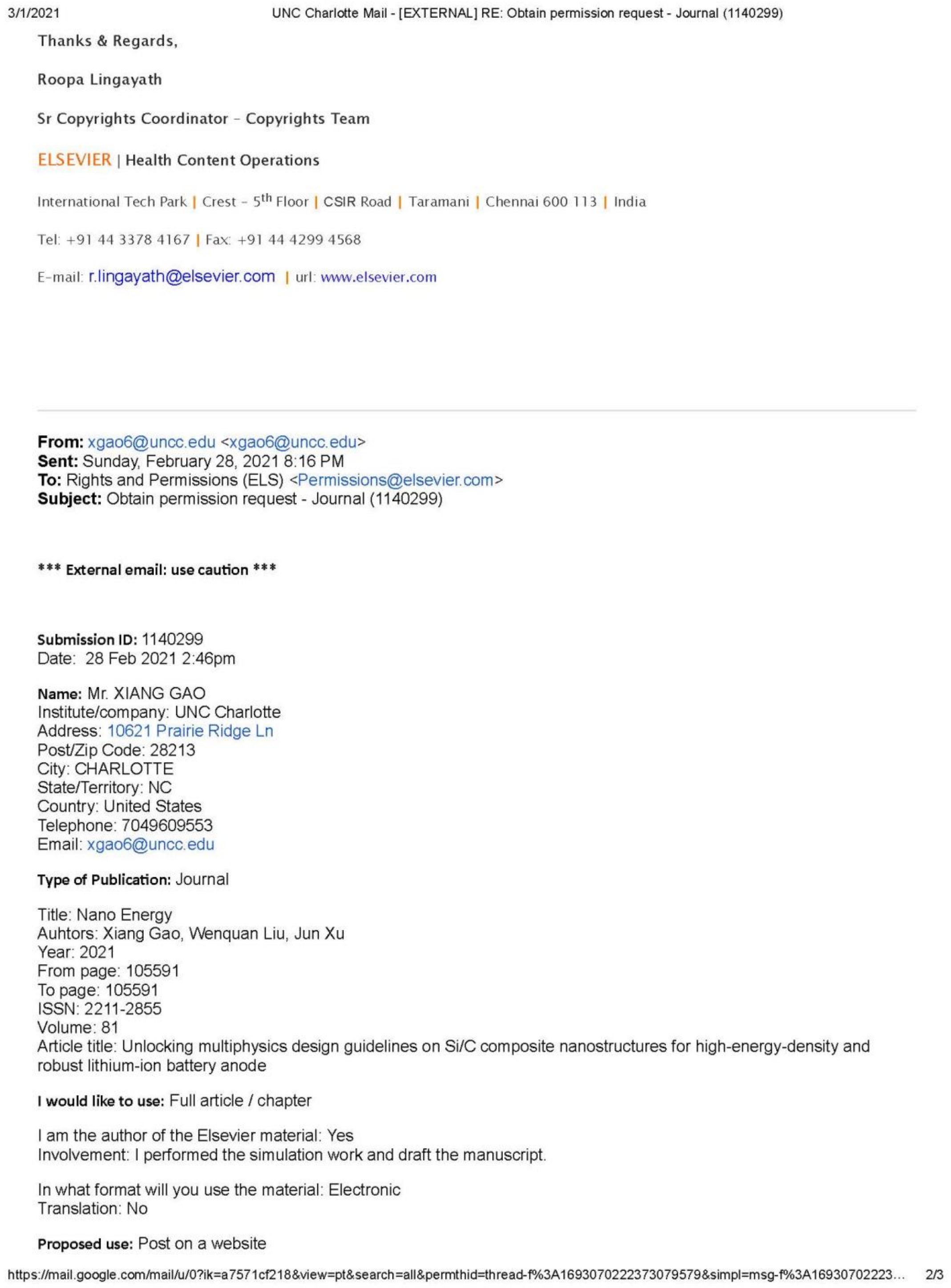

Thanks & Regards,

Roopa Lingayath

Sr Copyrights Coordinator – Copyrights Team

ELSEVIER | Health Content Operations

International Tech Park | Crest – 5th Floor | CSIR Road | Taramani | Chennai 600 113 | India

Tel: +91 44 3378 4167 | Fax: +91 44 4299 4568

E-mail: r.lingayath@elsevier.com | url: www.elsevier.com

From: xgao6@uncc.edu <xgao6@uncc.edu>
Sent: Sunday, February 28, 2021 8:16 PM
To: Rights and Permissions (ELS) <Permissions@elsevier.com>
Subject: Obtain permission request - Journal (1140299)

***** External email: use caution *****

Submission ID: 1140299
Date: 28 Feb 2021 2:46pm

Name: Mr. XIANG GAO
Institute/company: UNC Charlotte
Address: 10621 Prairie Ridge Ln
Post/Zip Code: 28213
City: CHARLOTTE
State/Territory: NC
Country: United States
Telephone: 7049609553
Email: xgao6@uncc.edu

Type of Publication: Journal

Title: Nano Energy
Auhtors: Xiang Gao, Wenquan Liu, Jun Xu
Year: 2021
From page: 105591
To page: 105591
ISSN: 2211-2855
Volume: 81
Article title: Unlocking multiphysics design guidelines on Si/C composite nanostructures for high-energy-density and robust lithium-ion battery anode

I would like to use: Full article / chapter

I am the author of the Elsevier material: Yes
Involvement: I performed the simulation work and draft the manuscript.

In what format will you use the material: Electronic
Translation: No

Proposed use: Post on a website

Attendees / Users: 800000
Website URL: https://www.proquest.com/
Password-protected: Yes
Material can be extracted: No

Additional Comments / Information: